

May 2021

## Developing Optical Imaging Tools to Investigate Metabolic and Structural Biomarkers in Rodent Injury Models

Soudeh Mostaghimi  
*University of Wisconsin-Milwaukee*

Follow this and additional works at: <https://dc.uwm.edu/etd>



Part of the [Biomedical Engineering and Bioengineering Commons](#)

---

### Recommended Citation

Mostaghimi, Soudeh, "Developing Optical Imaging Tools to Investigate Metabolic and Structural Biomarkers in Rodent Injury Models" (2021). *Theses and Dissertations*. 2701.  
<https://dc.uwm.edu/etd/2701>

This Thesis is brought to you for free and open access by UWM Digital Commons. It has been accepted for inclusion in Theses and Dissertations by an authorized administrator of UWM Digital Commons. For more information, please contact [scholarlycommunicationteam-group@uwm.edu](mailto:scholarlycommunicationteam-group@uwm.edu).

DEVELOPING OPTICAL IMAGING MODALITIES TO  
INVESTIGATE METABOLIC AND STRUCTURAL BIOMARKERS  
IN RODENT INJURY MODELS

by

Soudeh Mostaghimi

A Dissertation Submitted in  
Partial Fulfillment of the  
Requirements for the Degree of

Master of Science

in Engineering

at

The University of Wisconsin-Milwaukee

May 2021

# ABSTRACT

## USING AND DEVELOPING OPTICAL IMAGING MODALITIES TO INVESTIGATE METABOLIC AND STRUCTURAL ALTERATIONS IN RODENT INJURY MODELS

by

Soudeh Mostaghimi

The University of Wisconsin-Milwaukee, 2021  
Under the Supervision of Professor Mahsa Ranji

Optical fluorescence imaging is one of the vastly growing fields of imaging used in a broad variety of preclinical investigation with great interest in translating its principles into clinical applications. Optical fluorescence imaging provides images of functional and structural changes with cellular and subcellular resolution in tissues at a low-cost. This technique takes advantage of the absorption of light photons at a specific wavelength by intrinsic or extrinsic fluorophores and emission of photons at characteristic wavelengths. The characteristics of the emitted wavelengths such as their energy and illuminance give substantial information of the imaged tissue. In the research presented here, we probe two Krebs cycle intrinsic fluorescence metabolic coenzymes, reduced nicotinamide adenine dinucleotide (NADH) and oxidized flavin adenine dinucleotide (FAD) to study metabolic status changes during a human disease.

The objective of my research can be categorized into two themes; I) Designing an optical imaging instrument called an *in vivo* fluorescence imager to quantitatively investigate the metabolic changes in tissue and customizing it to be suitable for human/clinical studies. II) Using optical imaging techniques to quantitatively investigate the 3D anatomical structure changes in vessel structure of organs.

*in vivo* fluorescence imager can image many intrinsic and extrinsic fluorophores. However, we used it to track mitochondria bioenergetics NADH and FAD in wounds of diabetic mice. We also define the redox ratio (NADH/FAD) as a biomarker to investigate the effect of 670 nm photobiomodulation in those wounds. In another study, we have used 3D optical imaging system on the biopsy of diabetic wounds to confirm the results from the *in vivo* fluorescence imager. It showed that our *in vivo* fluorescence imager could successfully track the changes in the metabolic state of non-treated and treated diabetic wounds with 670 nm photobiomodulation.

Additionally, I validated a 3D vessel segmentation method developed in our lab by employing Murray's law. Furthermore, I used the 3D optical cryo-imaging system and the segmentation method to quantitatively study the 3D vessel structure changes in irradiated animal model. The result of this study showed that radiation can adversely change the vasculature in irradiated kidneys and negatively affect kidney perfusion.

In summary, my major contribution has been in device implementation and applications of imaging and image processing in studies of animal model diseases of humans.

© Copyright by Soudeh Mostaghimi, 2021  
All Rights Reserved

*I dedicate this thesis to  
all the people that suffered from health issues, the ones who survived and the ones we  
lost in the past year, especially.*

*My grandparents*

*My friend Soha*

*All the people we lost because of COVID 19*

*And all the traumatic brain injury survivors*

# TABLE OF CONTENTS

<b>LIST OF FIGURES</b> .....	<b>viii</b>
<b>LIST OF TABLES</b> .....	<b>x</b>
<b>LIST OF ABBREVIATIONS</b> .....	<b>xi</b>
<b>ACKNOWLEDGMENTS</b> .....	<b>xiii</b>
<b>1. Introduction</b> .....	<b>2</b>
1.1. Major contributions .....	2
1.1.1. Bio-instrumentation.....	2
1.1.2. Mathematical Validation.....	3
1.1.3. Experimentation, image acquisition, and data interpretation.....	3
1.1. Biological background.....	5
1.1.1. Cell biology .....	5
1.1.2. Reactive oxygen species .....	7
1.2. Tissue and Light interaction .....	8
1.3. Optical Metabolic Imaging.....	10
1.3.1. Imaging oxygenation:.....	11
1.3.2. Autofluorescence imaging .....	11
1.3.3. Fluorescence imaging of Contrast Agents .....	12
1.4. Animal Injury Models .....	13
<b>2. Bio-instrumentation</b> .....	<b>17</b>
2.1. <i>In vivo</i> fluorescence Imager.....	17
2.1.1. Hardware upgrade .....	17
2.1.2. User interface development.....	24
2.1.3. Linearity test of <i>in vivo</i> fluorescence imager .....	29
2.2. Fluorometer .....	30
2.2.1. Hardware Upgrade .....	31
2.2.2. User interface upgrade .....	32
<b>3. <i>In vivo</i> and 3D fluorescence imaging</b> .....	<b>35</b>
3.1. <i>In vivo</i> fluorescence imaging of diabetic wounds.....	35
3.1.1. Experimental Protocol.....	36
3.1.2. Time-line and tissue preparation .....	37
3.1.3. Image processing.....	37
3.1.4. Results .....	38
3.2. 3D fluorescence Cryo-imager.....	40
3.2.1. Metabolic imaging of Diabetic wounds .....	41
3.2.1.1. Experimental Protocol: .....	41
3.2.1.2. Image processing: .....	41

3.2.1.3. Results: .....	42
3.2.1. Vascular imaging validation: .....	43
3.2.2. Kidney radiation-induced vascular injury .....	46
3.2.2.1. Experimental protocol .....	46
3.2.2.2. Vascular quantification and segmentation .....	47
3.2.2.3. Results.....	48
<b>4. Conclusion and future direction .....</b>	<b>60</b>
<b>References.....</b>	<b>62</b>

## LIST OF FIGURES

Figure 1: Electron transport chain.....	7
Figure 2: four ways of light and tissue interactions .....	9
Figure 3: Jablonski Diagram.....	10
Figure 4: Schematic of the preliminary design of the <i>in vivo</i> fluorescence imager.....	18
Figure 5: The actual implementation of the preliminary design of the <i>in vivo</i> fluorescence imager .....	19
Figure 6: The schematic of the upgraded <i>in vivo</i> fluorescence imager.....	21
Figure 7: The overview of the <i>in vivo</i> fluorescence imager.....	23
Figure 8: The actual implementation of the upgraded <i>in vivo</i> fluorescence imager. ....	23
Figure 9: The <i>in vivo</i> fluorescence imager user interface control panel. ....	25
Figure 10: Overall flow chart of <i>in vivo</i> fluorescence imager user-interface .....	27
Figure 11: The “Channel Picker” predefined process flow chart. ....	28
Figure 12 : The “Save” predefined process flow chart. ....	28
Figure 13) The results of the linearity test for the fluorescence imager using exogenous NADH and FAD solutions .....	30
Figure 14: The schematic of fluorometer.....	31
Figure 15: Background cod of XLED SubVi .....	33
Figure 16: The upgraded control panel for the fluorometer. ....	33
Figure 17: Representative <i>in vivo</i> fluorescence images of NADH, FAD, and the tissue redox ratio (NADH/FAD) for representative wounds over days. ....	39
Figure 18: The cryo-imaging results of sham-treated vs. FR-PBM treated wounds .....	43

Figure 19: VMI follows Murray's Law .....	46
Figure 20: The representative extracted 3D vasculatures .....	51
Figure 21: The representative extracted 3D vasculatures colored-coded based on diameter .....	52
Figure 22: The representative extracted 3D vasculatures colored-coded based on branch depth	53
Figure 23: The average of measurements on all the kidneys in bar plots $\pm$ standard deviation. ...	57

## LIST OF TABLES

Table 1 : Quantitative assessment of FR-PBM ( <i>in vivo</i> ) .....	40
Table 2: The fold changes for day-90 and day-60 post radiation. ....	54
Table 3: The average of measured vessel parameters and their standard deviation. ....	55
Table 4: The number of vessels that was detected for different ranges of 100 $\mu\text{m}$ span .....	58

## **LIST OF ABBREVIATIONS**

3D - Three-Dimensional

ADP - Adenosine Diphosphate

ATP - Adenosine Triphosphate

CCD - Charged Coupled Device

EC - Endothelial Cell

ETC - Electron Transport Chain

FAD - Flavin Adenine Dinucleotide

FR - Far red

FR-PBM – Far red Photobiomodulation

IACUC - Institutional Animal Care and Use Committee

Micro-CT - Micro-Computed Tomography

NADH - Nicotinamide Adenine Dinucleotide

NADPH - Nicotinamide Adenine Dinucleotide Phosphate

NAD(P)H - Combination of NADH and NADPH

NIR - Near-infrared

OS – Oxidative Stress

OMCA- optical metabolic contrast agents

PBI - Partial Body Irradiation

PBM - Photobiomodulation

ROS - Reactive Oxygen Species

RR - Redox Ratio

VMI - Vascular-Metabolic Imaging

WF- White Field

## ACKNOWLEDGMENTS

I would like to express my appreciation and gratitude to my advisor, Dr. Mahsa Ranji, for recognizing my potential to make a strong contribution to field of biomedical engineering. She convincingly guided and encouraged me to be professional and do the right thing even when the road got tough. Without her persistent help, the goal of this project would not have been realized.

I would like to extend my sincere thanks to our collaborators whose assistance was a milestone in the completion of these projects, especially Prof. Gopalakrishnan, Prof. Eells, Prof. Camara, and Prof. Medhora. I would like to recognize the invaluable support that you all provided during my study.

I like to thank my dissertation committee, Prof. Gopalakrishna and Prof. Hu not only for agreeing to serve as my committee, but for their time, intellectual contributions to my development as a scientist and for their insightful contributions.

I would like to recognize the assistance and help that I received from the former members of the Biophotonics Lab Shima Mehrvar and Farnaz Foomani.

Finally, I wish to acknowledge the love and support of my family and my friends, my mother, Soudabeh; my father, Hossein; my sister, Kimia; and my friends, Behnam and Pardis. Thanks for your constant support through the ups and downs of my academic career. It has been bumpy at times, but your confidence in me has enhanced my ability to get through it all and succeed in the end.

# **Chapter 1**

## **Introduction**

# 1. Introduction

Biophotonics is the study of the light and photonics process in biological systems. One of the most important aspects of this field is tracking the extrinsic and intrinsic fluorescence agents by imaging and sensing cells and tissues.

The research presented here involves the use and development of different imaging instruments and image processing techniques to investigate the effect of multiple diseases on the metabolic state of different tissues by tracking intrinsic fluorescence imaging. The obtained information can be of great interest in identifying and implementing interventions to treat or prevent diseases.

## 1.1. Major contributions

During my research activities at Biophotonics lab, I have contributed to the following three major areas:

### 1.1.1. Bio-instrumentation

I have contributed to the new design/upgrade of two devices as one major contribution to my thesis. These two devices are called optical *in vivo* fluorescence imager and fluorometer. Both instruments are used to track the intrinsic mitochondrial fluorophores, NADH and FAD. The former uses imaging techniques and the later uses signaling techniques. I utilized different optical components to design and develop the optical *in vivo* fluorescence imager. Then, by using LabVIEW, I have developed a user-interface that accelerated the different parts of experiments by automation of different parts synchrony and image acquisition. The clinical use of optical *in vivo* fluorescence

imager is in process. For fluorometer, I upgraded the systems by employing better light source and improving the user-interface code.

### **1.1.2. Mathematical Validation**

By using the 3D fluorescence cryo-imager and a segmentation method developed in Biophotonics lab, the anatomical 3D-vessel structure of different organs could be extracted. However, a co-registration was needed to validate this method. By employing the minimum work hypothesis of Murray's law, I was able to mathematically validate this method. I also used this method to computationally assess the effect of irradiation on the anatomical renal vessel structures and endothelium changes.

### **1.1.3. Experimentation, image acquisition, and data interpretation**

I was involved in two experiments during my studies, 1) the effect of far-red photobiomodulation on diabetic wounds of mice 2) the effect of 12.5 Grey irradiation on renal vessel structure of rats. For both experiments I participated on experimentation, image acquisition and data interpretation. Conducting all these experimental studies required the assembly of the required tools and designing experimental protocols to study the metabolism in the cryogenic, *in vivo*, and *ex vivo* regimens. For each regime used in this study, unique treatment, and preparation of the tissues, as well as proper imaging and acquisition methods are required. Moreover, different methods and techniques of image processing was used for each of these studies. The samples and surgery needs are provided by the Medical College of Wisconsin, the University of Wisconsin-Madison, and the College of Nursing at the University of Wisconsin-Milwaukee. My M.Sc, contributions and research are published in the following peer-reviewed journals and conference proceedings.

## Journal Publications

- J1. **S Mostaghimi**, S Mehrvar, F Foomani, N Narayanan, B Fish, AKS Camara, MM Medhora, and M. Ranji, “Quantification of Radiation Induced Renal Vascular Structure (Vasculature) Injuries: A time-response and dose-response study.,” (In submission process)
- J2. F. Foomani, JA. Jarzembowski, **S. Mostaghimi**, S. Mehrvar, SN. Kumar and M. Ranji, “Optical Metabolic Imaging of Mitochondrial Dysfunction on HADH Mutant Newborn Rat Hearts,” (submitted to JTHEM)
- J3. S Mehrvar, **S Mostaghimi**, F Foomani, N Narayanan, B Fish, AKS Camara, MM Medhora, and M. Ranji, “3D vascular-metabolic imaging using inverted intrinsic fluorescence,” (Under revision)
- J4. **S Mostaghimi**, S Mehrvar, FH Foomani, B Abroe, JT Eells, S Gopalakrishnan and M Ranji, “670nm Photobiomodulation improves the Mitochondrial Redox State of Diabetic Wounds,” (2021)
- J5. S Mehrvar, FH Foomani, S Shimada, C Yang, N Zheleznova, **S Mostaghimi**, A Cowley, and M Ranji, “The Early Effects of Uninephrectomy on Rat Kidney Metabolic State Using Optical Imaging,” (2020)

## Selected Conference Proceedings and Presentations

- C1. **S Mostaghimi**, S Mehrvar, FH Foomani, J Narayanan, JT Eells, AKS Camara, B Fish, M Medhora, and M Ranji, “Vascular injury in lung vessels post-irradiation: a dose and time response case study,” *CLEO*, San Diego (2021)

- C2. **S Mostaghimi**, S Mehrvar, FH Foomani, B Abroe, JT Eells, M Ranji, and S Gopalakrishnan, “The Effect of NIR Light Treatment in Metabolic State of Diabetic Wounds,” *BMES*, Philadelphia (2019)
- C3. S Mehrvar, F Foomani, **S Mostaghimi**, M Medhora, AKS Camara, and M Ranji, “Radiation-induced Injuries to Rat Kidney Vasculature,” *BMES*, Philadelphia (2019)
- C4. FH Foomani, S Mehrvar, **S Mostaghimi**, S Shimada, C Yang, N Zheleznova, AW Cowley Jr., and Mahsa Ranji, “The Early Effects of Uninephrectomy on Rat Kidney Metabolic State Using Optical Imaging,” *BMES*, Philadelphia (2019)

## **1.1. Biological background**

### **1.1.1. Cell biology**

Cells are the fundamental and smallest units of life[2]. All living organisms are made of cells. Cells can be classified into two groups based on their structure: eukaryotes and prokaryotes. The former refers to the cells with many or one nucleus and the latter refers to the cells without a nucleus. Eucaryotic are more complex than prokaryotic cells and have more elaborate intracellular compartments. Their metabolism depends on the oxidation of organic molecules by one of the most important organelles in the cell, mitochondrion. A mitochondrion contains a smooth outer membrane and a convoluted inner membrane [3]. The prominent role of mitochondria is to produce the units of energy, ATP, and to regulate the metabolism of a cell [4]. Cell produces ATP with breakdown of glucose and other substrates through glycolysis, Krebs cycle and oxidative phosphorylation. However, the synthesis of ATP mostly happens through a set of chemical reaction reactions via electron transport chain, located on the inner membrane of mitochondrion [3]. At first, during glycolysis two NADH molecules are produced to serve as electron donors to

the electron transport chain. Glycolysis is a cytoplasmic pathway that breaks glucose into two pyruvate molecules that enter the Krebs cycle. During pyruvate decarboxylation, FAD is reduced to FADH<sub>2</sub> which further will be used in the electron transport chain as well [5, 6]. The synthesis of ATP requires a proton gradient that happens through the pumping of electrons from the mitochondria matrix into mitochondrial intermembrane space. These electrons are obtained from electron donation of NADH to complex I and FADH<sub>2</sub> to complex II of the electron transport chain. In the end, complex V of electron transport chain is turned by the force of proton gradient, which facilitates the addition of a phosphate to adenosine diphosphate (ADP) to synthesis ATP [7, 8]. Figure 1 shows a schematic of the electron transport chain and the role of NADH and FADH<sub>2</sub> in it. Maintaining a proper pool of NADH and FAD is required for the proton gradient across the inner and outer membrane of mitochondria. On one hand, Cells with high levels of NAD(P)H have higher molecule for electron donation. As a result, they have a greater potential for producing ATP through oxidative phosphorylation. On the other hand, cells with elevated levels of FAD and low NAD(P)H have a higher demand for ATP production. Consequently, they need more oxidative phosphorylation to meet this energy demand [6].

In summary, NADH and FAD play an important role in cellular metabolic activities. Luckily, due to their fluorescent properties, they can be tracked to monitor cellular metabolism without exogenous markers. Chance et al, for the first time, introduce the concept of optical redox ratio and defined it as the ratio of NADH/FAD [9-13]. Redox ratio can be a global biomarker for the metabolic activity of cells and is a direct biomarker of a change in tissue oxidation state. For example, increases in oxidative metabolism rises the production of FAD and consumption of NADH and as a result, a decrease in redox ratio. [14, 15]. Therefore, by developing modalities to

track these biomarkers, we can detect irregularities in cellular metabolism and develop interventions to prevent or reverse damages to cells.

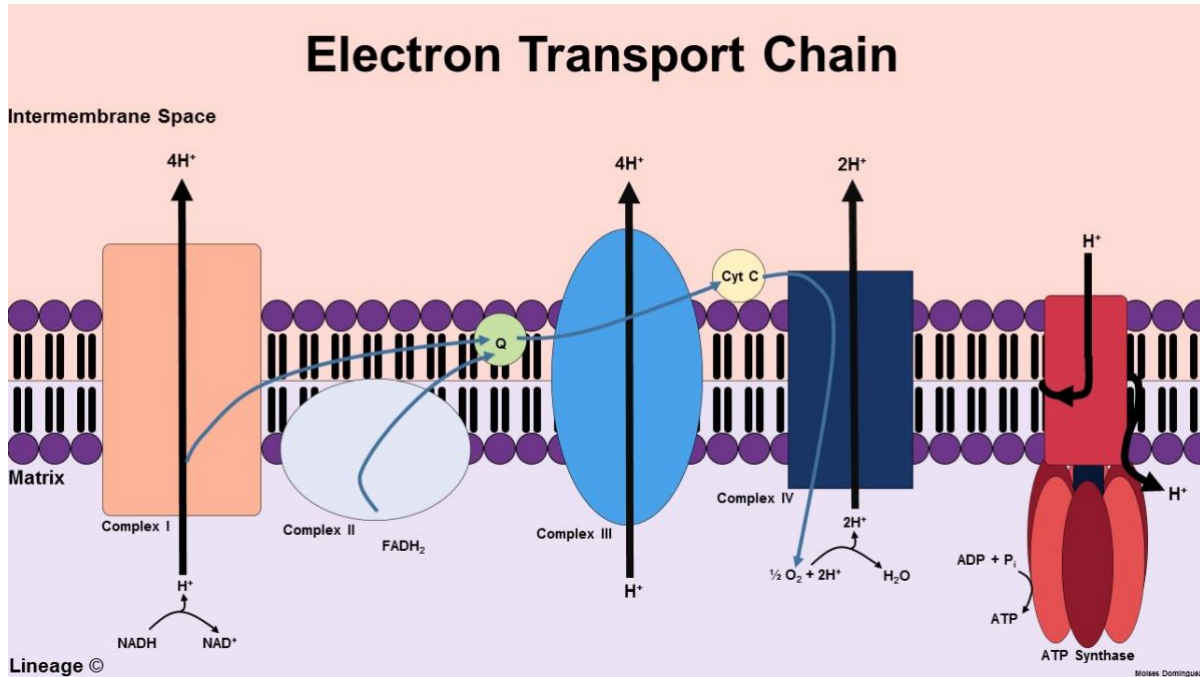


Figure 1: **Electron transport chain** with electron donation of NADH and FADH<sub>2</sub> to complex I and II. The proton gradient at complex V facilitates the ATP synthesis [16]. Reprinted from Electron Transport chain, by Medbullets Team, <https://step1.medbullets.com/biochemistry/102051/electron-transport-chain>, Copyright 2021 by Lineage Medical.

### 1.1.2. Reactive oxygen species

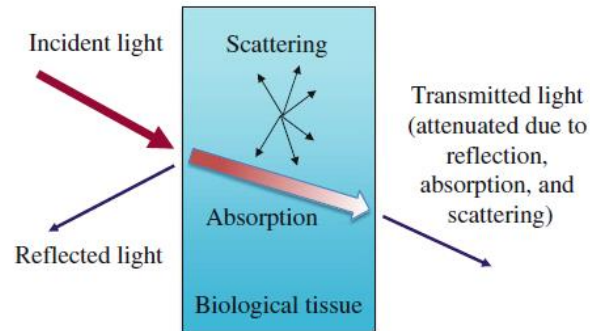
Species that contain one or more unpaired electrons are called free radicals. Reactive oxygen species (ROS) is a term used for both oxygen radicals and certain nonradical oxidizing agents that can convert to free radicals [17]. Also, ROS are by-products of normal cell metabolism, produced mainly by mitochondria, that play a vital role in cell signaling and redox regulating [18, 19]. A massive amount of mitochondrial ROS production happens at the electron transport chain [19]. An imbalance in antioxidant defense capacities and ROS production can lead to an oxidative stress

state [20]. Oxidative stress can damage proteins, nucleic acid and cell membrane, causing cumulative damages contributing to numerous diseases [21]. Even a slight increase in oxidative stress can lead to mitophagy, in which the mitochondria degrade but manage to recycle the released nutrient. But, if the increase in the oxidative stress continues, the cell can go through apoptosis or even necrosis, where the former is programmed cell death and the latter is abnormal cell death [22]. Therefore, it is highly assumed that changes in the levels of ROS are associated with mitochondria dysfunction that can lead to many diseases. The accumulation of NADH, an autofluorescence ROS and an important co-enzyme in the electron transport chain, in the dysfunctional mitochondria, is one of the examples [23]. As a result, the changes in the level of ROS are greatly involved in the pathology of many diseases such as radiation injuries [24], type II diabetes, cardiovascular diseases and muscular disorders [18]. In the studies presented here, beside NADH we also track FAD which is a cofactor of one the most important source of ROS, xanthine oxidoreductase (XOR) [17, 25]. As explained before, the ratio of NADH/FAD is a global biomarker of cellular metabolism and can give us an understanding of the oxidative stress state of the tissue.

## **1.2. Tissue and Light interaction**

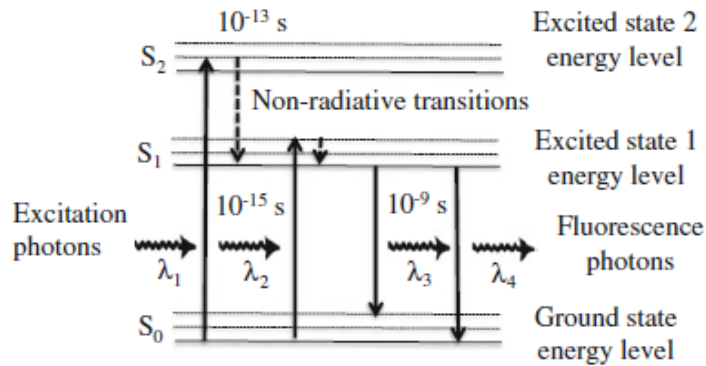
Tissue and light interaction effects can be observed in four ways. 1) reflection at a material surface 2) transmission when lights enter an environment (tissue) and passes through it. 3) absorption of photon energy by the material (tissue). 4) multiple scattering of photons in the material (tissue).

Figure 2 is showing these different interactions [1].



*Figure 2: four ways of light and tissue interactions: 1) reflection 2) transmission 3) absorption 4) scattering [1]. Adapted from Light-tissue interactions, by G Kesier, 2016, Springer, Copyright by Springer Science+Business Media Singapore 2016.*

The absorption of light by a part of an organic molecule called chromophores can result in fluorescence. Chromophores absorb light at a specific wavelength, and after a short time, emit it with a longer wavelength [1]. This process is called fluorescence and is also related to the transition of a molecule from the excited state to the ground state [26]. This process is illustrated in a Jablonski diagram presented in Figure 3.



**Figure 3: Jablonski Diagram.** Fluorescence happens when a molecule relaxes from an excited state to the ground state [1]. Reprinted from Light-tissue interactions, by G Kesier, 2016, Springer, Copyright by Springer Science+Business Media Singapore 2016.

In Figure 3, level  $S_0$  is the ground state energy,  $S_1$  and  $S_2$  are the first and second excited states. Each of these states has different vibrational energy levels (shown by dashed horizontal lines). The transition between states is only possible through absorption or emission of quantized energy units, photons. The absorption of photons is shown with upward solid vertical lines. In this process, a photon ( $\lambda_1$  or  $\lambda_2$ ) can excite the molecule from  $S_0$  state to one of the higher vibrational levels of  $S_1$  or  $S_2$ . Afterwards, the molecule will relax through a non-radiative internal process, shown with dashed vertical lines, to the lowest vibrational level of  $S_1$ . Subsequently, the molecule will relax to the ground state ( $S_0$ ) through emitting a fluorescent photon ( $\lambda_3$  or  $\lambda_4$ ) resulting in fluorescence. The solid downward vertical lines show the emission of fluorescent photons. Fluorescence substances, fluorophore, are broadly classified into two groups of intrinsic or extrinsic fluorophores. The biological molecules that can naturally go through the fluorescence process, called autofluorescence or natural fluorescence, are called intrinsic fluorophores [1].

### 1.3. Optical Metabolic Imaging

Optical imaging techniques, such as fluorescence and bioluminescence are emerging new modalities, with widespread applications from molecular biology to disease diagnosis and therapy [27, 28]. These techniques are becoming substantial because of reasons such as their ability to provide: a) functional and structural changes with high resolution, b) information in microscopic and macroscopic scale, c) quantitative information for follow-ups and objective diagnosis, and being: d) being non-invasive, e) non-ionizing f) of low cost [28]. Optical metabolic images are classified into three major groups:

### **1.3.1. Imaging oxygenation:**

The oxygen that is received by respiratory system is transferred to the blood flowing through pulmonary capillaries in the alveoli. The oxygenated blood then is moved to different organs by cardiovascular system. Afterwards, the oxygen is released from hemoglobin and is diffuse to the parenchymal cells in tissues. The transfused oxygen then is used in cytochrome oxide in the electron transport chain of mitochondria to produce ATP [29]. Therefore, the whole body respirometry is used to study the mitochondrial function. However, inferring the mitochondrial dysfunction from changes in oxygen consumption is very difficult because of the shortcomings to distinguishing whether a dysfunction in the mitochondria is because of a malfunction in the consumption of ATP or in the supplying of substrates [30]. But optical absorption provides the contrast for functional imaging since it provides information on the oxygen saturation of hemoglobin. This will give us functional information of the intact microcirculation *in vivo*.

### **1.3.2. Autofluorescence imaging**

NADH and FAD are two autofluorescence coenzymes involved in the synthetization of ATP. Therefore, both coenzymes exist in oxidized (NAD<sup>+</sup> and FAD) and reduced (NADH and FADH<sub>2</sub>) forms. However, only NADH and FAD yield significant fluorescence. NADH is excite at 350 nm

and emits maximum at 460 nm, while FAD is excited at 435 and has an emission maximum at 535. Since NADH has a higher quantum yield, it is associated with greater overall fluorescence intensity. Although NADH and NAD(P)H are both autofluorescence with overlapping excitation and emission spectra, studies have established that the autofluorescence is dominated by NADH. Because, not only NADH has a higher quantum yield, but also, other studies show that metabolic changes due to diseases such as cancer progression and drug treatments are ascribed to NADH [6].

Due to their role in cellular metabolism, NADH and FAD are used for molecular and cellular imaging in small-animal models[27]. As a quantitative biomarker, the ratio of NADH/FAD is used to describe the redox state of a tissue. Studies, conducted by many researchers, including our team, has shown the changes of redox ratio are associated with metabolism injuries due to ischemia-reperfusion [31-36], hyperoxia[37], diabetes[38], gene knockout[33, 39-42] and also with different treatments responses such as photo-modulation therapy[43, 44], cancer therapy[45-47] and mitigating radiation induced injuries[48].

### **1.3.3. Fluorescence imaging of Contrast Agents**

The advantage of optical metabolic contrast agents (OMCA) imaging is the combination of high spatial and temporal resolution with molecular-information. It can provide us with inter- and intracellular activity in real time with subcellular resolution. Four of the main branches of OMCA are nutrient uptake, enzyme activity, local chemical environment and cell signaling [6].

Most of the mitochondrial ROS productions are not fluorescence, therefore, by imaging the exogenous fluorophores that are correlated with OS, the mitochondrial ROS production rate can be monitored. May new modalities, methodologies and experimental protocols are advancing to quantify the alteration in oxidative stress caused by various stress conditions in an uncoupled or inhibited state of

cells. For example, the metabolic activity of cells under metabolic stressors such as hypoxia or high glucose condition is being studied.

#### **1.4. Animal Injury Models**

The animal injury models that have been studied are as follows:

**Diabetic wound and photo-biomodulation (PBM):** Chronic non-healing wounds are generally believed to develop when the acute inflammatory phase of wound healing progresses to chronic inflammation without resolution [49]. Chronic lower-extremity ulcers are a common complication of diabetes, and approximately 15% to 25% of individuals diagnosed with diabetes will develop lower extremity ulcers or foot ulcers at some point in their lifetime [50]. Moreover, diabetic ulcers often persist for months to years in debilitated patients [51-53]. These ulcers can become infected, causing pain, discomfort, hospitalizations, and poor quality of life, which impose a tremendous economic burden on the healthcare system with costs conservatively estimated for the management of diabetic foot ulcers to be \$9–13 billion in the United States [54]. This gives rise to a secondary demand; a need to be able to monitor and track the cellular changes during the wound healing trajectory, so that effective interventions can be identified and implemented during the early stages benefiting the patient population [55].

Current treatment strategies for wound management in diabetic patients involve debridement, topical antibiotics, the application of topical dressings, and oftentimes surgery [56]. Clinical Studies have shown that interventions like hyperbaric oxygen therapy (HBOT) and extracorporeal shock wave therapy can improve the process of diabetic wound healing [57-61]. Photobiomodulation (PBM) using far-red (FR) to near-infrared (NIR) light is a non-invasive, painless, and inexpensive therapeutic modality with documented efficacy in preclinical and

clinical studies in soft-tissue injuries and wound healing [62, 63]. In our studies, we investigated the effect of 670 far-red photo-biomodulation on wound healing process of excisional wounds on diabetic mice.

### **Partial body irradiation injury:**

Radiation induces intravascular coagulation in kidneys [64], leading to many vascular diseases such as renal artery atherosclerosis[65]. Atherosclerosis in large vessels can result in severe thromboembolic events, stenosis or renal failure [66]. Although some researchers claim that radiation therapy-induced renal arterial stenosis is very rare[67, 68], others have reported severe stenosis in intrarenal vascular branches[69]. One of the other radiation-induced injuries in the kidneys is radiation nephropathy[70]. Nephropathy is a kidney disease caused by damages to the small blood vessels or units in the kidney that are responsible blood filtration[71]. Radiation nephropathy can happen when a person is exposed to a radiation dose, higher than 5 Grey. Therefore, radiation nephropathy is possible after a nuclear accident, terrorism or radiotherapy [72, 73]Another sequel of cancer radiotherapy and accidental radiation is radiation-induced renal fibrosis that is excessive accumulation of collagen and other extracellular matrices (ECM) components [74-76]. Fibrosis is the hallmark of chronic kidneys diseases and can impair the function and morphology of vessels [77]. All aforesaid diseases are the result of narrowing of the blood vessels that is considered as one of the late vascular injuries [66]. Therefore, one of the most extensively studied side effects of radiation is vascular injuries [78]. However, the focus of most of these studies is mainly on the cellular and molecular pathology of these diseases and the computational and mathematical aspects of the effect of radiation on vascular remodeling has not been thoroughly studied. Nevertheless, it should not go unnoticed that the kidney plays an important part in blood perfusion, vascular tone, electrolyte control and blood filtration and it has

been shown that the correlation between the kidney's structural heterogeneity and functional physiology is very strong [79]. Therefore, a computational assessment of vasculature changes in the kidney due to radiation would help us to understand the pathology of radiation-induced injuries. In this study, we computationally investigate the earlier effect of radiation, 60 and 90 days after irradiation, on vessels  $\geq 70$   $\mu\text{m}$ . With our newly developed method [80] we observed the effect of irradiation on vessels by measuring the vessel diameter, volume, number of terminal points and branch depth.

# **Chapter 2**

## **Bio-instrumentation**

## 2. Bio-instrumentation

In this chapter, the hardware-design and upgrade of the *in vivo* fluorescence imager and fluorometer are covered. Then the development of the user interface for the *in vivo* fluorescence imager and soft-ware upgrade of fluorometer is discussed.

### 2.1. *In vivo* fluorescence Imager

We developed the *in vivo* fluorescence imager to quantitatively investigate the correlation of mitochondria metabolism in delayed diabetic wound healing in mice and the effect of Far-red photo-biomodulation on those wounds.

#### 2.1.1. Hardware upgrade

By using *the in vivo* fluorescence imager, we imaged the surface fluorescence of cutaneous wounds to monitor the changes in the concentration of NADH and FAD. To do so, we used an excitation source with an appropriate wavelength to excite NADH and FAD and optical filters, to filter the emitted photons from wounds and pass them to a CCD camera. Figure 4 shows a schematic of the preliminary design of the fluorescence imager. An XYZ translational micro-positioner (ThorLabs, NJ, USA) is used to manually control the field of view in XY direction. The Z-direction of the positioner movement controls the working distance and the focus of the images. A mercury arc lamp (Intensilight, Nikon, Tokyo, Japan) generates the excitation white light and passes it to the excitation filter wheel (FW103H, ThorLabs, NJ) through a liquid light guide. The excitation filter wheel has two channels for NADH and FAD. For each channel, the light spectrum is filtered by optical filters at selected wavelengths to excite the specific fluorophores of NADH and FAD from the surface of the wounds. We set the excitation filter for NADH at 350 nm (80-nm

bandwidth, UV Pass Blacklite, HD Dichroic, Los Angeles, CA) and FAD at 437 nm (20-nm bandwidth, 440QV21, Omega Optical, Brattleboro, VT. On the emission path, another filter wheel (FW103H, ThorLabs, NJ) is implemented with two channels to pass the emitted photons from NADH and FAD. The emission filters for NADH and FAD are set at 460 nm (50-nm bandwidth, D460/50M, Chroma, Bellows Falls, VT) and 537 nm (50-nm bandwidth, QMAX EM 510-560, Omega Optical), respectively. At the end of the emission path, a charge-coupled camera (QImaging, Rolera EM-C2, 14 bit) with 1,004×1,002-pixel arrays is used to save the online and real-time surface fluorescence. Two neutral density filters (ThorLabs, NJ) are also used as excitation and emission filters for white field channel imaging. We also used a two-channel stepper motor (BSC202, ThorLabs, NJ) to manually synchronize the rotation of the excitation and emission filter wheels.

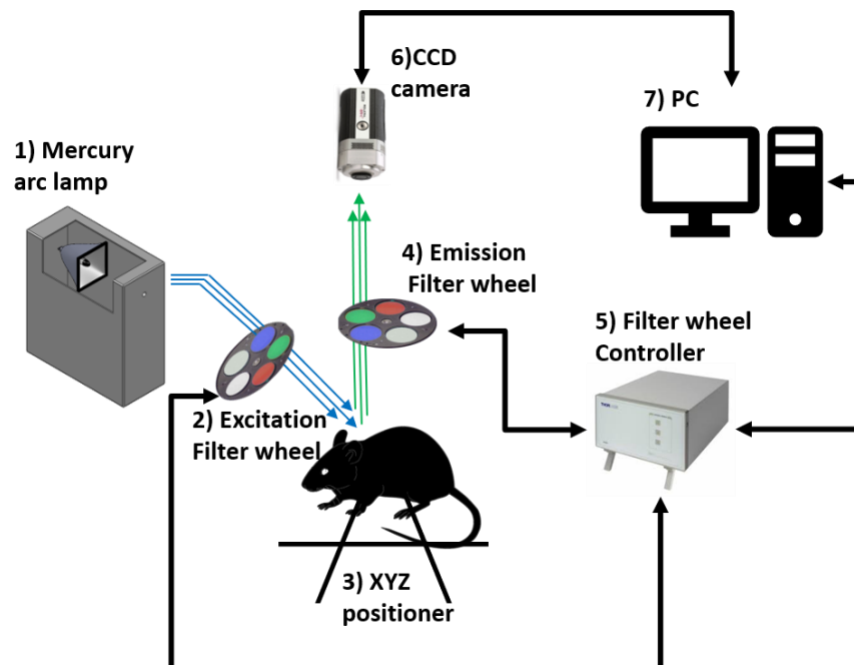


Figure 4: Schematic of the preliminary design of the *in vivo* fluorescence imager.

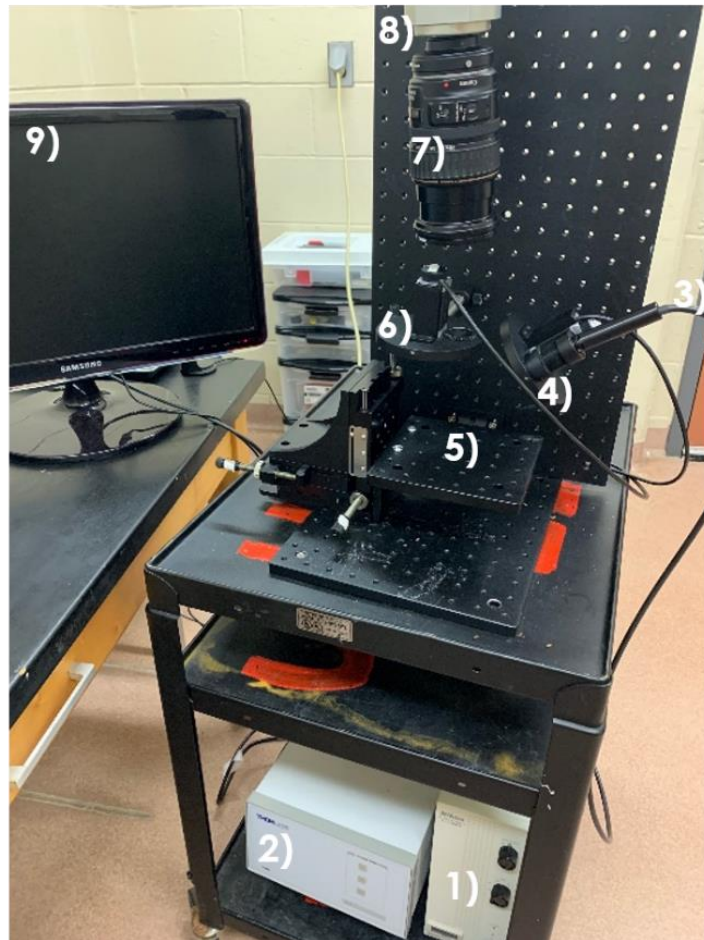
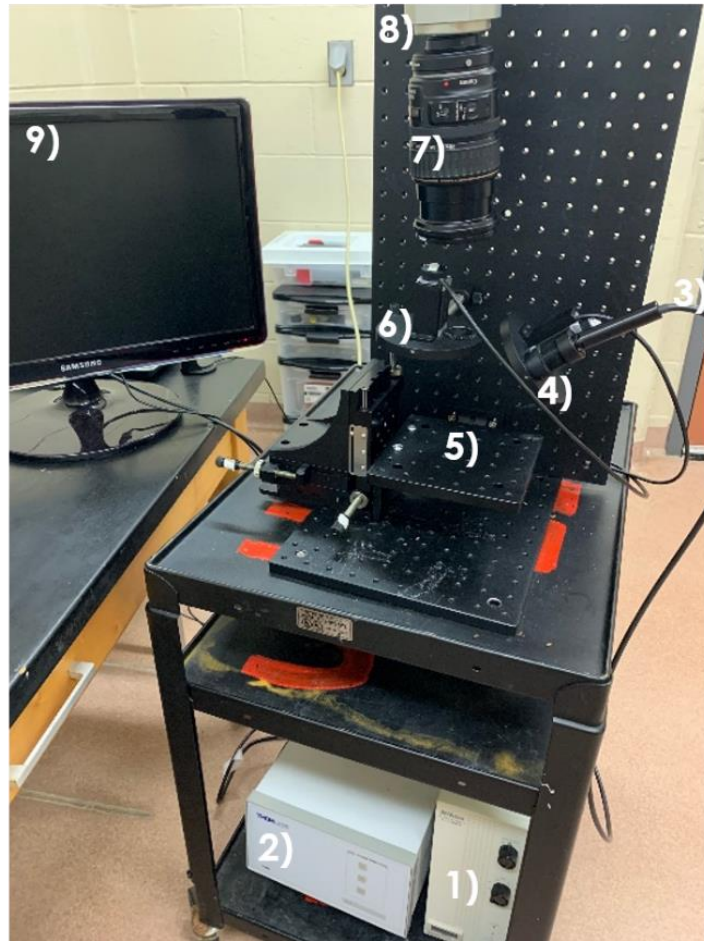


Figure 5 shows the actual implementation of the preliminary *in vivo* fluorescence imager. Different parts of it are as follows:

1. The excitation source: Nikon intensilight
2. Filter wheel controller: 2-channle stepper motor
3. Liquid light guide
4. XYZ positioner

5. Excitation filter wheel



*Figure 5: The actual implementation of the preliminary design of the *in vivo* fluorescence imager.*

- 6. Emission filter wheel
- 7. Lens: Nikon
- 8. CCD Camera: Rolera EM-C2
- 9. PC

To facilitate the use of the *in vivo* fluorescence imager for other experiments and clinical trials, the preliminary design of the *in vivo* fluorescence imager has undergone several improvements. Three major parts that were changed are the excitation light source, the camera, and the lens. The Nikon

lens in the preliminary design was changed with a close focus zoom lens from Edmund Optics (Edmund Optics, Blackwood, NJ, USA). This zoom lens has a higher working distance (from 127 mm to infinity), wide field of view, close focus, and variable apertures, to adjust the depth of field, making the user needless of XYZ micropositioner. On this account, just by changing the settings on the zoom lens, the user can zoom and focus on the desired area without any need for position change of the experimental model or the patient. Moreover, Edmund lens (\$ 613) is much cheaper in terms of cost compared to the previous Nikon lens (\$ 5000). By replacing the Nikon lens with Edmond lens, while reducing the cost of prototype assembly, the resolution of the images is saved.

Another fundamental change is related to the replacement of the excitation source. Instead of using a lamp as the excitation light source with white light and an excitation filter wheel, we used fluorescence LED illumination, Xcite LED1 (Excelitas Technologies Corp., Waltham, MA, USA) with four switchable wavelengths, due to many reasons, including:

**Speed:** The interchangeable excitation filters integrated for each LED modules is designed to allow accelerated wavelength switching beyond the scope of motorized filter wheels. Saving time, by reducing the imaging process of all three channels from 10 minutes to less than 5 minutes.

**Phototoxicity:** Preliminary studies show that the cells manifest less phototoxicity after imaging with LED versus mercury lamps. Therefore, the possible errors in the redox ratio caused by mercury arc lamp are reduced.

**Lower cost:** Using LEC decreases electrical consumption by 69%, reducing the operating costs.

**Environment green:** It would greatly help the environment for two reasons. One, the light source does not contain mercury and two, energy consumption is reduced by 84%.

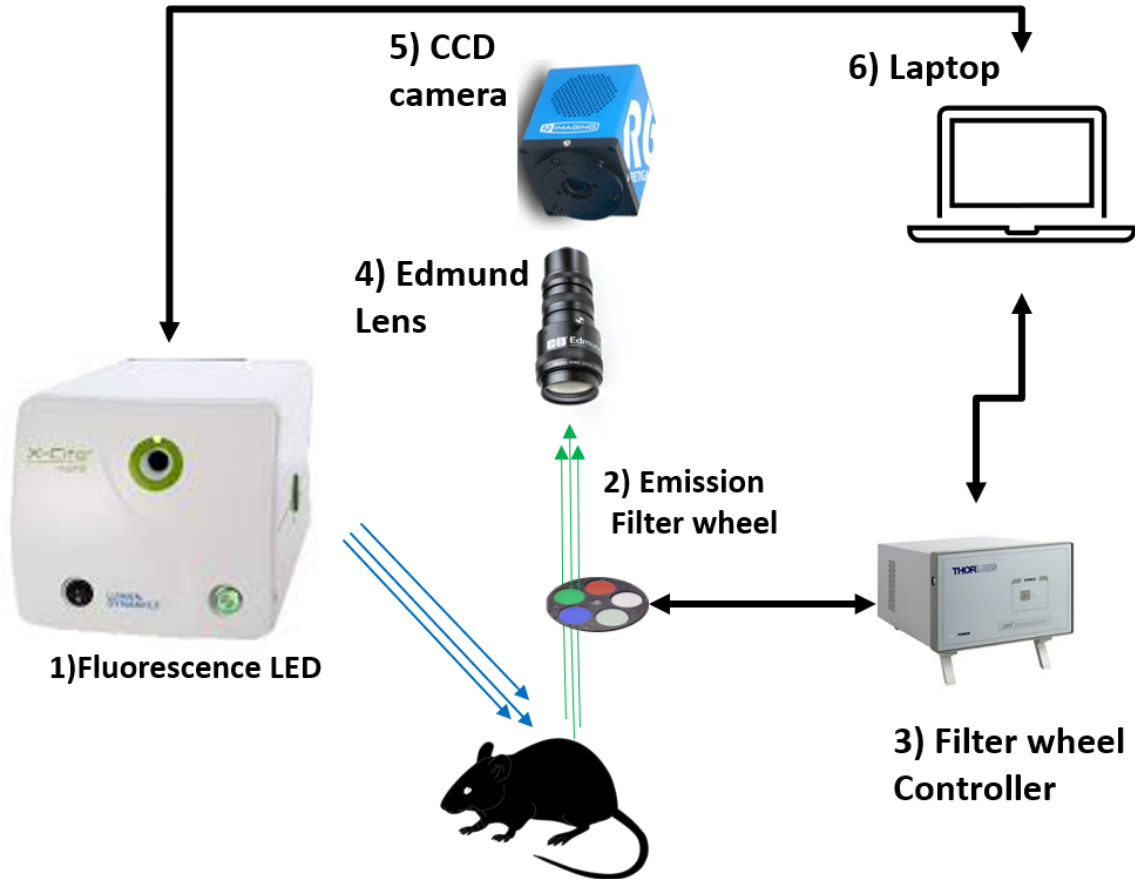
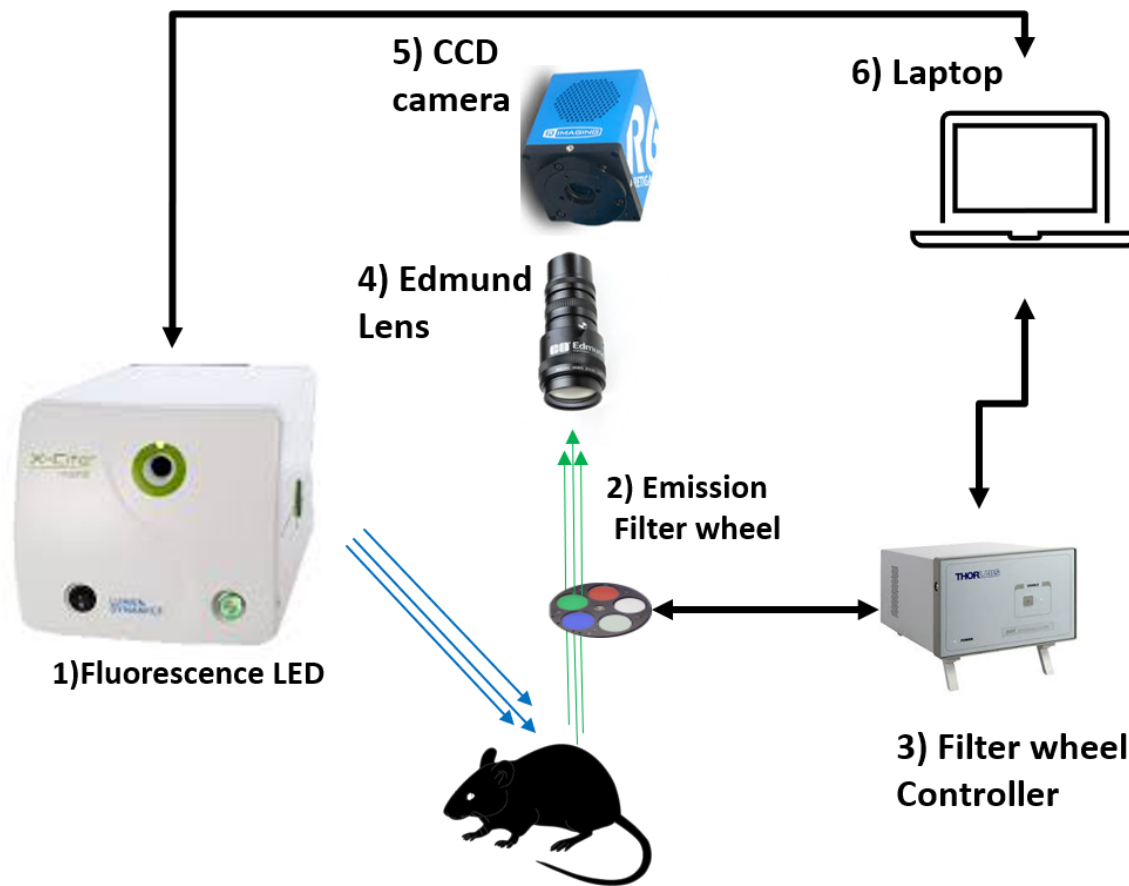


*Figure 6: The schematic of the upgraded *in vivo* fluorescence imager.*

One of the other main changes is the replacement of the Rolera camera with Retiga R6. Retiga R6 with a pixel array of 2688×2200, 16-bit and higher field of view, increased the resolution and dimensions of acquired images.



Figure

6 shows the schematic of the upgraded *in vivo* fluorescence imager.

In this design, since Xcite LED1 provides us with the excitation wavelengths for exciting NADH and FAD, the excitation filter wheel is removed, and by that means, just the emission filter wheel needs a controller. As a result, we replaced the two-channel stepper motor with a lighter and smaller one-channel stepper motor (BSC201, ThorLabs, NJ).

The *in vivo* fluorescence imager is designed to image the surface fluorescence of a tissue. The tissue can be on any part of a patient body. In the case of diabetic wounds, the diabetic ulcers are on the low-extremity of patients. To facilitate the imaging process and to minimize the movement

of the patient, we needed to be able to rotate the fluorescence imager so the patient would not have to experience any discomfort from changing their position. Therefore, the optical parts of the fluorescence imager were separated from the hardware parts and put in two different boxes. Box “a” containing the liquid light guide, emission filter wheel, lens and camera, and box “b” contains the excitation source and filter wheel controller.

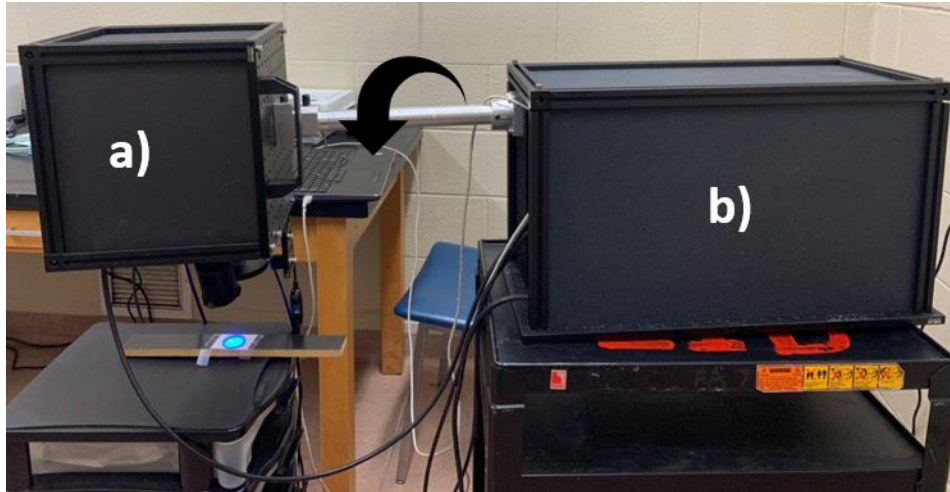


Figure 7 is showing these two boxes, attached with a bar, allowing the optical parts to rotate separately from the rest of the instrument and image tissues on different parts of a body.

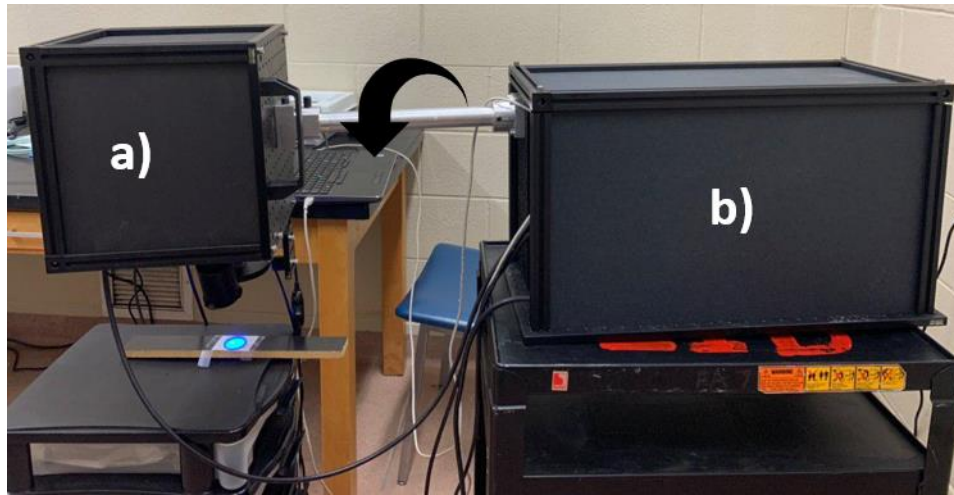


Figure 7: The overview of the *in vivo* fluorescence imager.

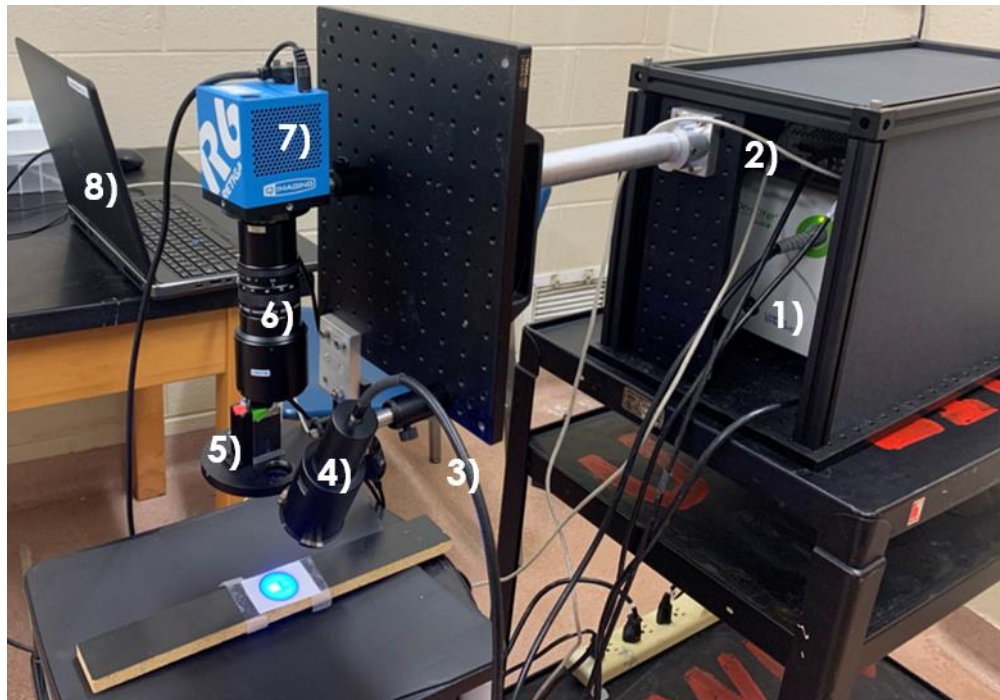


Figure 8 shows the internal design of box “a” and “b”, containing:

1. Excitation source: Xcite LED1

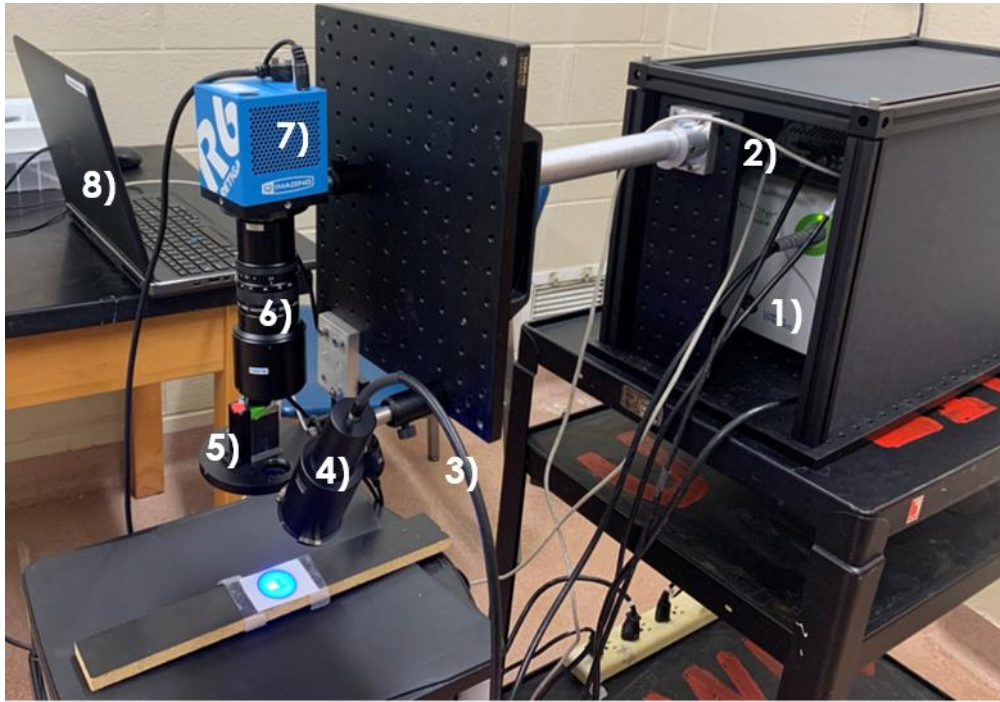


Figure 8: The actual implementation of the upgraded *in vivo* fluorescence imager.

2. Filter wheel controller: 1-channel stepper motor
3. Liquid light guide
4. Fiber adapter
5. Emission filter wheel
6. Edmond zoom lens
7. CCD camera: Retiga R6
8. Laptop

With these changes applied to *in vivo* fluorescence imager, not only it has become more user friendly but also the size and weight have been significantly reduced making it easier to move. Moreover, the ability to rotate the optical part of the instrument accommodates the patients with the ease of positioning.

### **2.1.2. User interface development**

One of the significant improvements for the *in vivo* fluorescence imager was developing a user interface using LabVIEW (2019 National Instruments). Two user interfaces were developed for the design with two filters and the design with one filter wheel and the Xcite LED as the excitation source. However, to make it brief, only the user interface that is developed for Xcite LED will be discussed.

*This user-interface atomizes the synchrony of excitation light with the proper emission filter. Also, it enables the user to choose an arbitrary exposure and a path for saving images. The user interface*

reduced the time of experiments from 5 minutes to less than 1 minute.

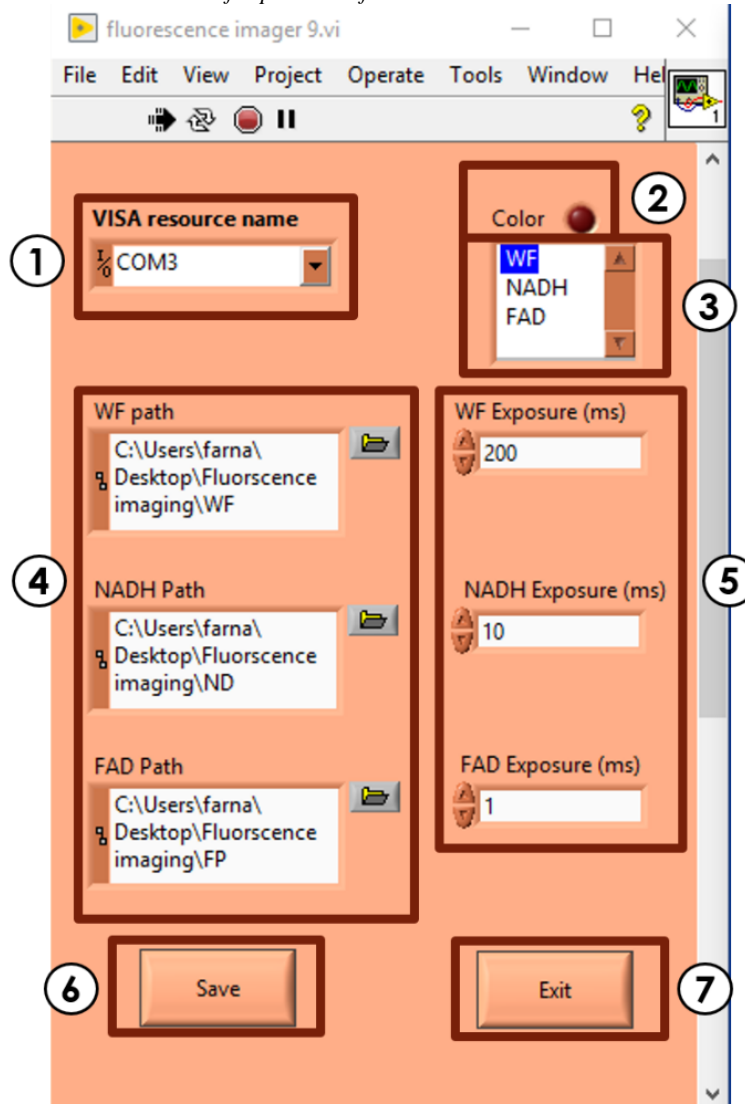


Figure 9 shows the control panel of the *in vivo* fluorescence imager. Seven parts of the control panel are boxed and numbered. Box 2 of the control panel shows a red LED representing the current camera temperature. This LED indicates the camera has reached the regulated temperature lock when it turns green. Before running the program, the proper COM should be inserted in box 1. Users receive or give the information from each box of the control panel as follows:

1. Insert the COM to start communicating with the device and run the program.
2. Wait for the LED to turn green.
3. Click on the channel you want to image.

4. Enter the path you want the image to be saved for each channel.

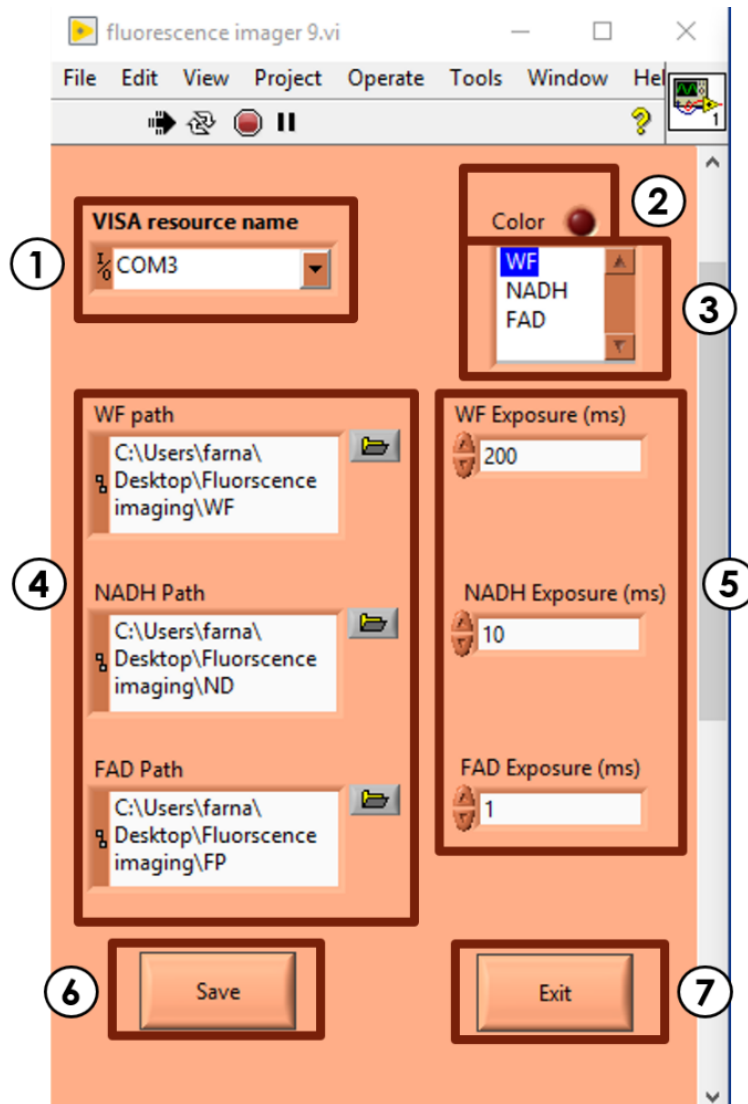


Figure 9: The *in vivo* fluorescence imager user interface control panel.

5. Set the exposure for each channel.
6. Click on the “Save” button to save the image.
7. Click on the “Exit” button when the experiment is over to turn off the device.

After running the program, a window will pop up showing live video (on-line and real-time) of the tissue. The exposure for each channel is predefined and as explained before, the user can set the desired exposure from box 5. By clicking on each of the channels in part 3, the selected channel

will be highlighted by blue in the control panel and excitation wavelengths will change accordingly. The emission filter wheel will also rotate to synchronize the excitation wavelength and optical emission filter. The path that images are saved is predefined too. User can save the images from each channel in an arbitrary path by entering the desired path for each channel in part 4 and then click on the “Save” button. It is important to mention that by clicking on the “Save” button, an image from what the camera is displaying at the moment will be saved. To save the images from other channels, the user should click on the desired channel from part 3 and then click on the “Save “button again. The overall flow chart for the user interface is shown in .

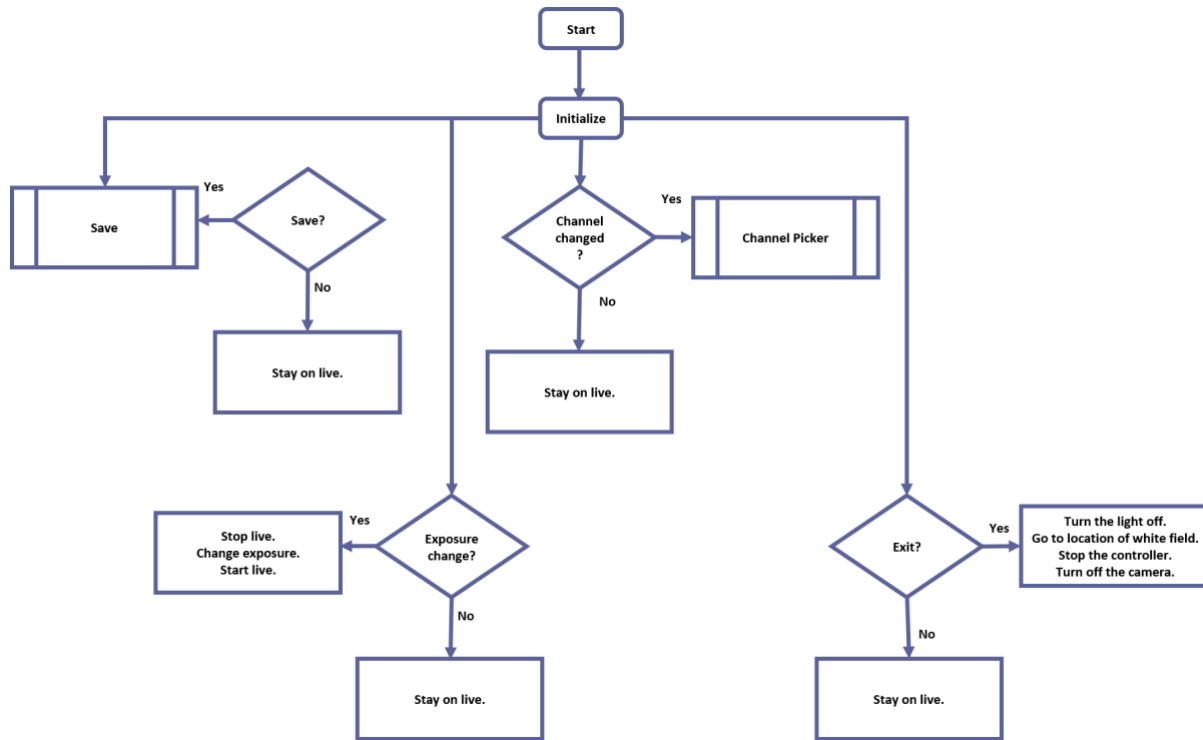
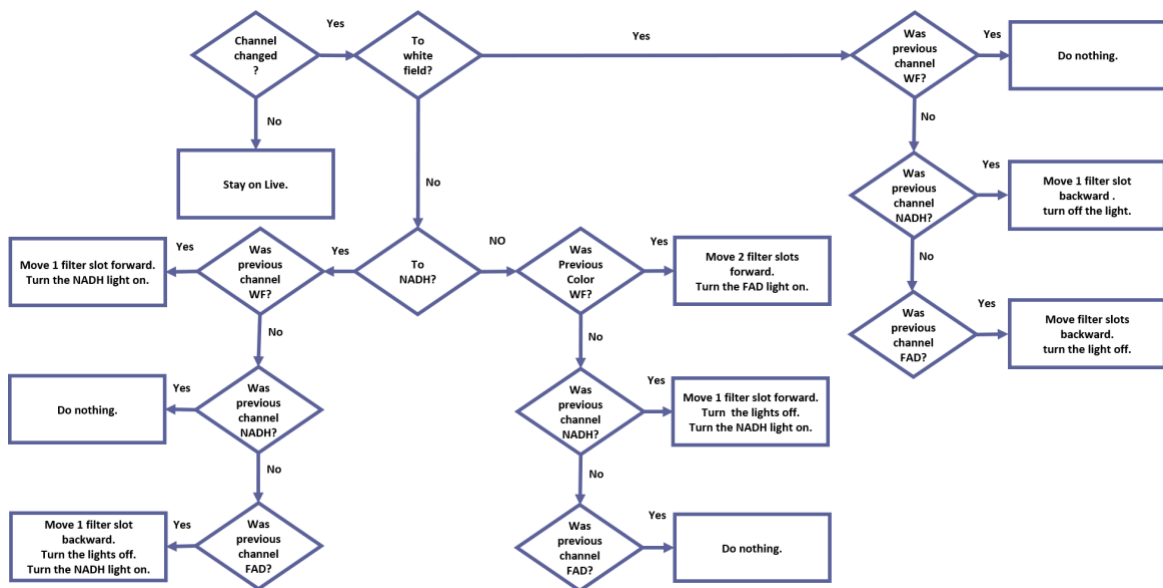


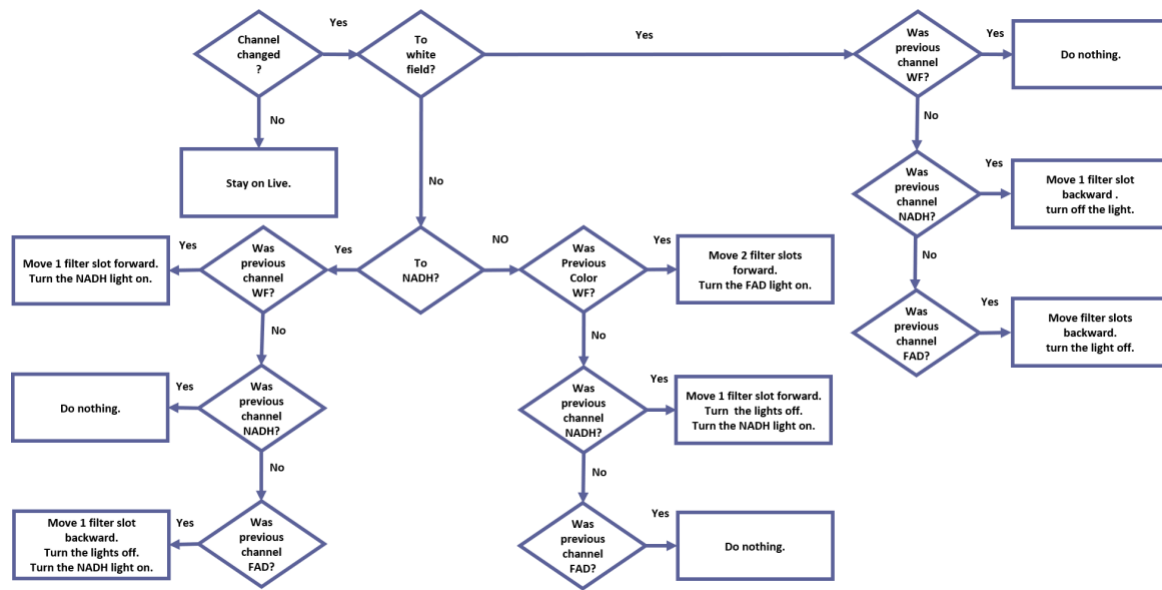
Figure 10: Overall flow chart of *in vivo* fluorescence imager user-interface

The "Channel Picker" predefined process is executed every time the user selects a channel from



box 3.

Figure 11 shows the flow chart of the "channel picker". As



Figure

11shows, the *in vivo* fluorescence imager is calibrated on the white field and if the user runs the program, the camera shows white field footage of the tissue. By selecting other channels, the

excitation source and the filter wheel will change accordingly and the NADH and FAD footages of tissue will be displayed.

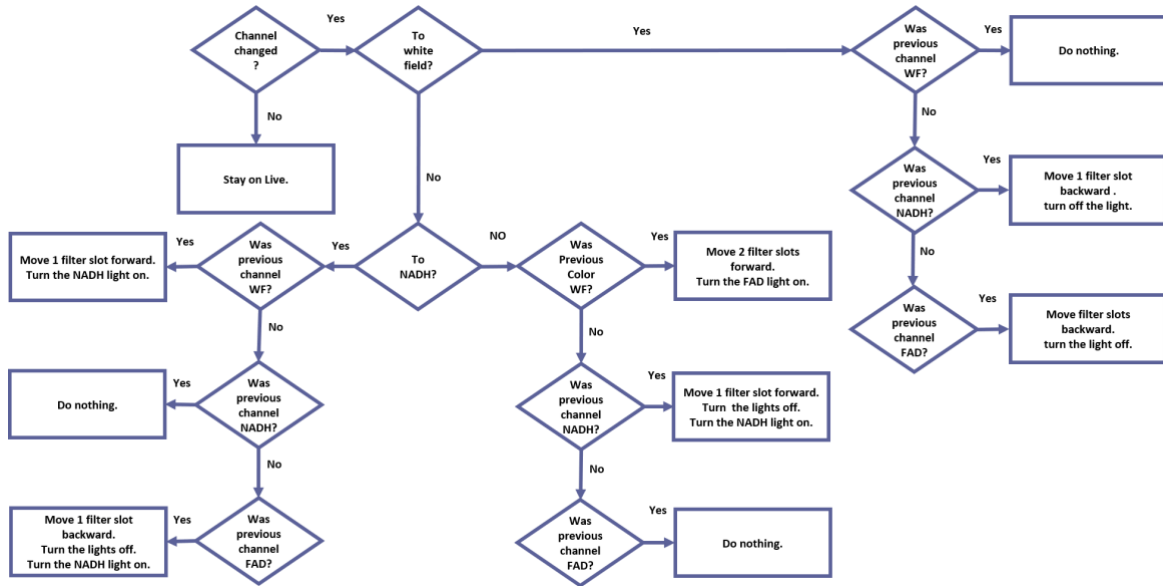


Figure 11: The “Channel Picker” predefined process flow chart.

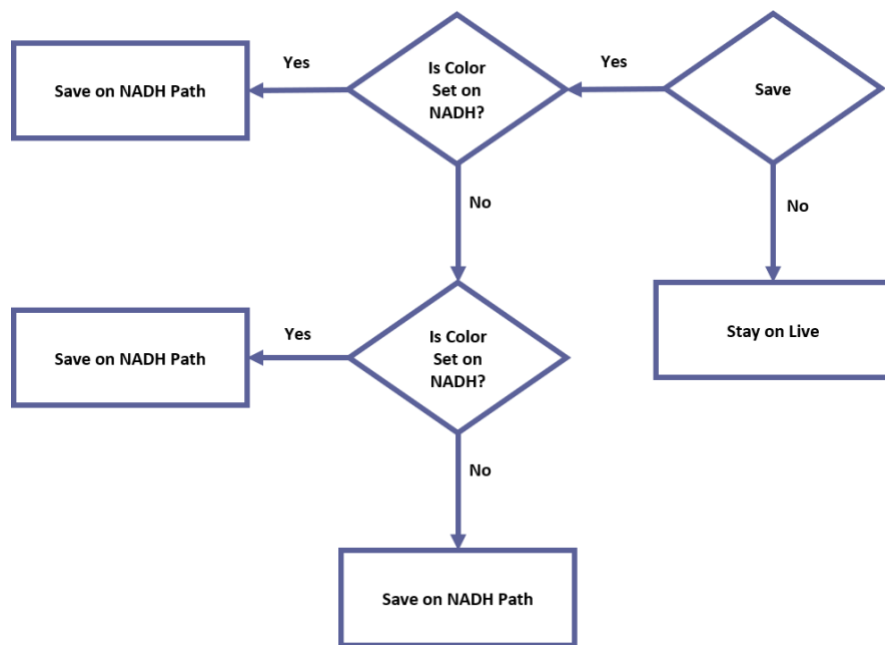


Figure 12 shows the flow chart of the “Save” predefined process. The saving path will change

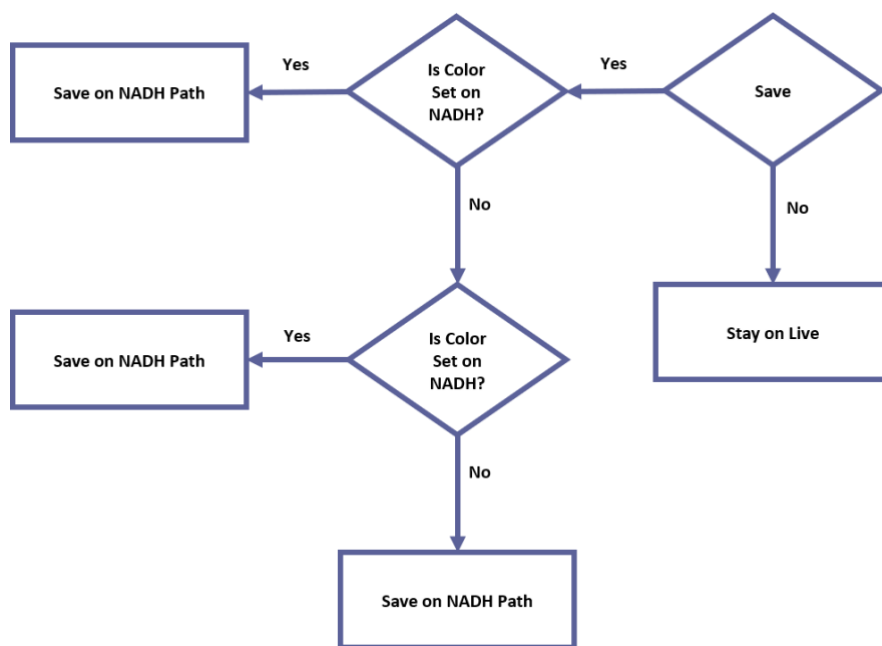


Figure 12 : The “Save” predefined process flow chart.

accordingly by selected channels from box 3.

### 2.1.3. Linearity test of *in vivo* fluorescence imager

This test is performed to assess the linearity response of the system. Cuvettes containing dilution of NADH and FAD fluorescent dyes (Sigma-Aldrich Inc., St. Louis) were imaged. The concentrations were chosen based on tissues' physiological relevant range [81]. The mean  $\pm$  standard deviation (SD) of the images is calculated, and linear regression is performed (

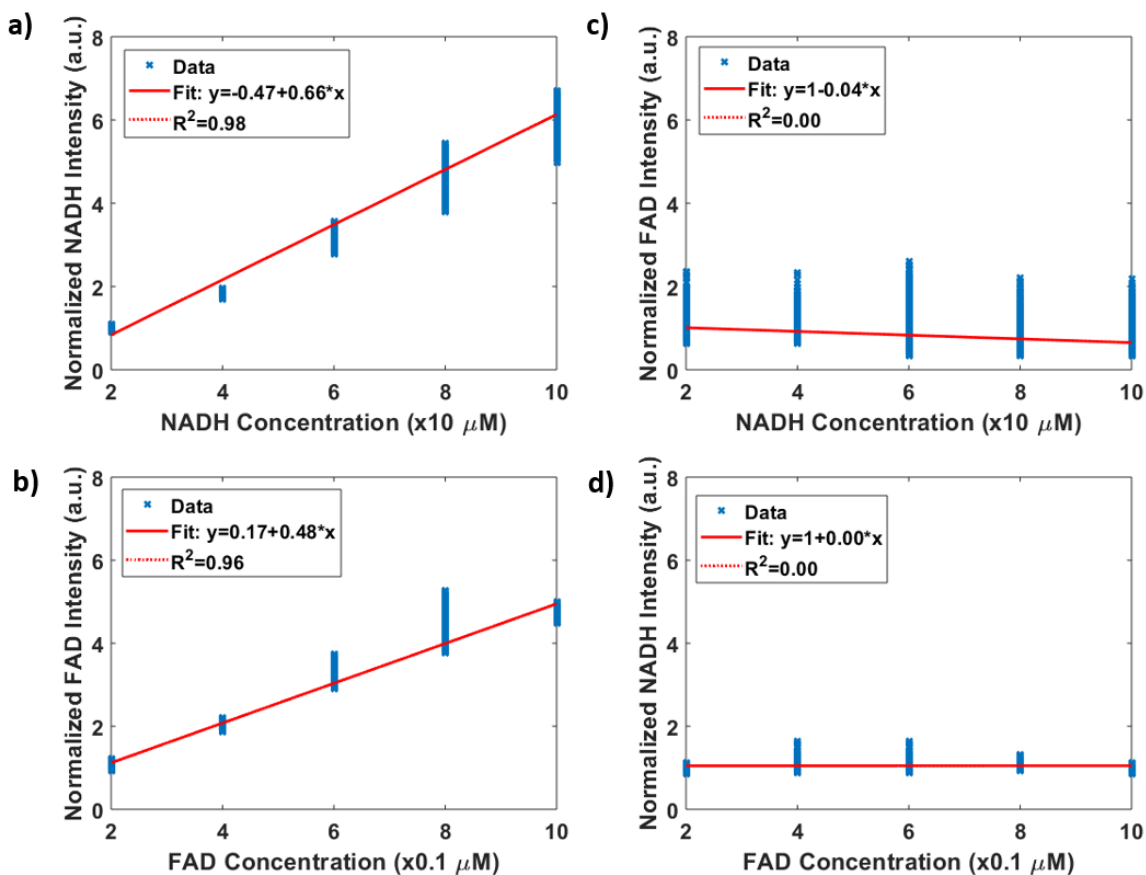


Figure 13). For correlations between measurements, a Pearson correlation coefficient was determined.

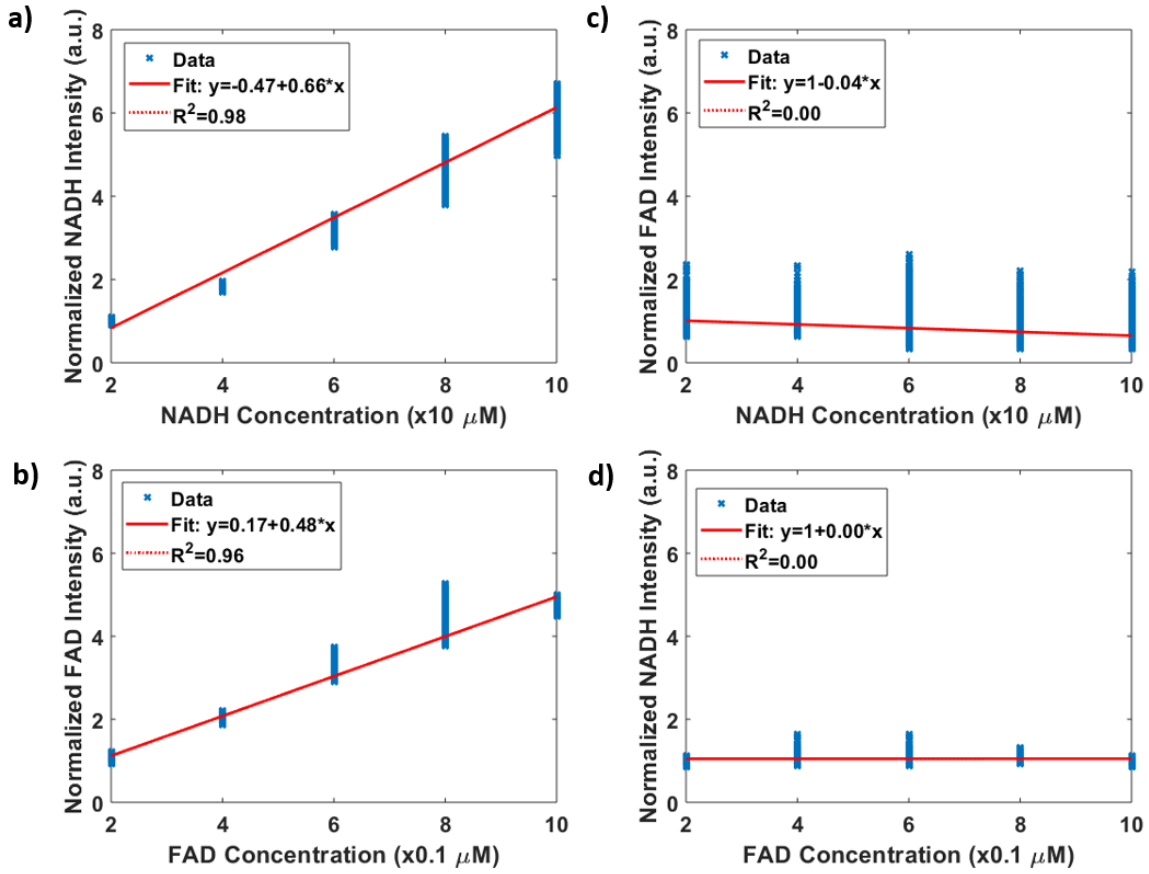


Figure 13a shows that the NADH channel of fluorescence imager is linear with the changes in the concentration of NADH ( $R^2=0.98$ ,  $P<0.001$ ), while in

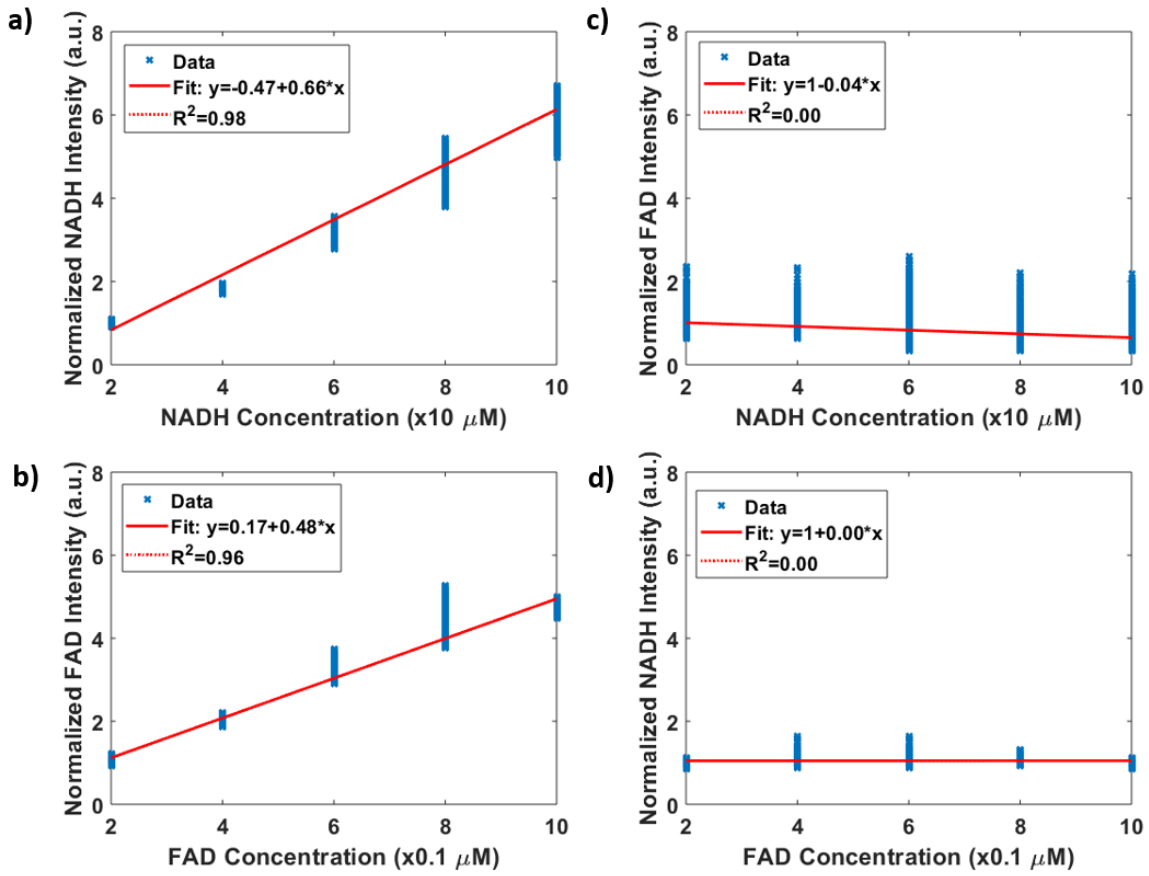


Figure 13b, the intensity of the captured NADH images remained constant with FAD concentration variations. These results suggest that the NADH channel is sensitive to NADH solely, and it is unresponsive to FAD concentration variations. Similarly, by increasing the concentration of FAD in the solutions, the intensity of captured FAD images increases linearly (

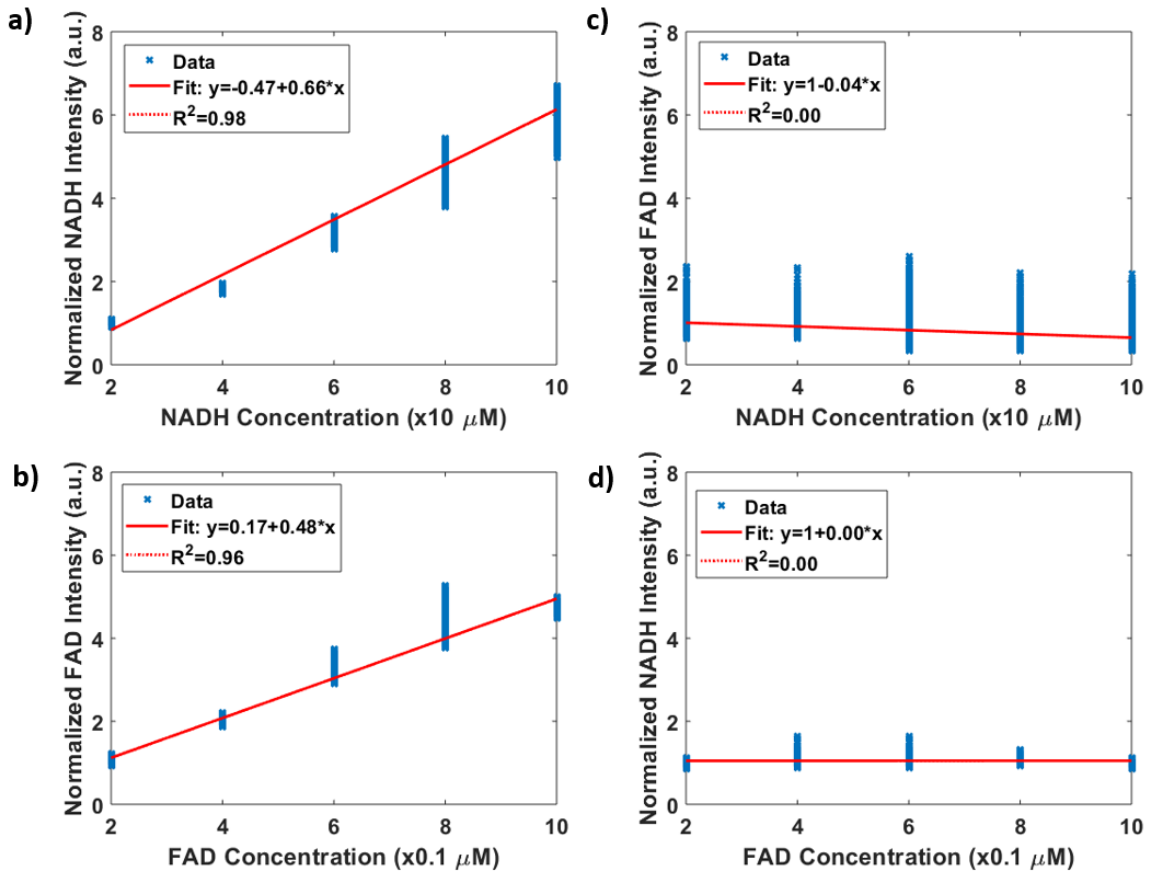


Figure 13c,  $R^2=0.98$ ,  $P<0.001$ ), and the intensity of NADH images remained constant (

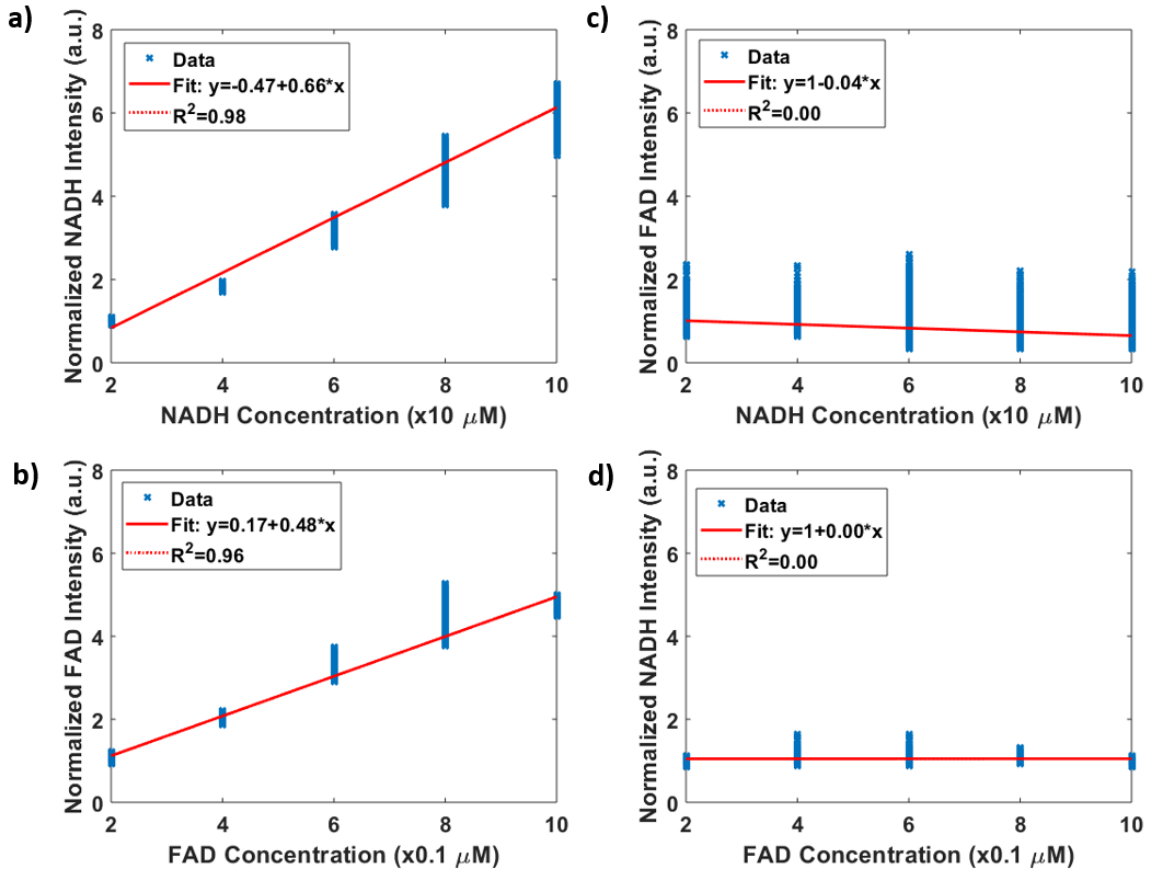


Figure 13d). Therefore, the fluorescence imager used in our study is linear in the biologically relevant concentrations of NADH and FAD, and there is no cross-relation between the two channels. Furthermore, it can be inferred that the intensities of the cryo-images correlated linearly with the amount of the autofluorescence signal from the samples.

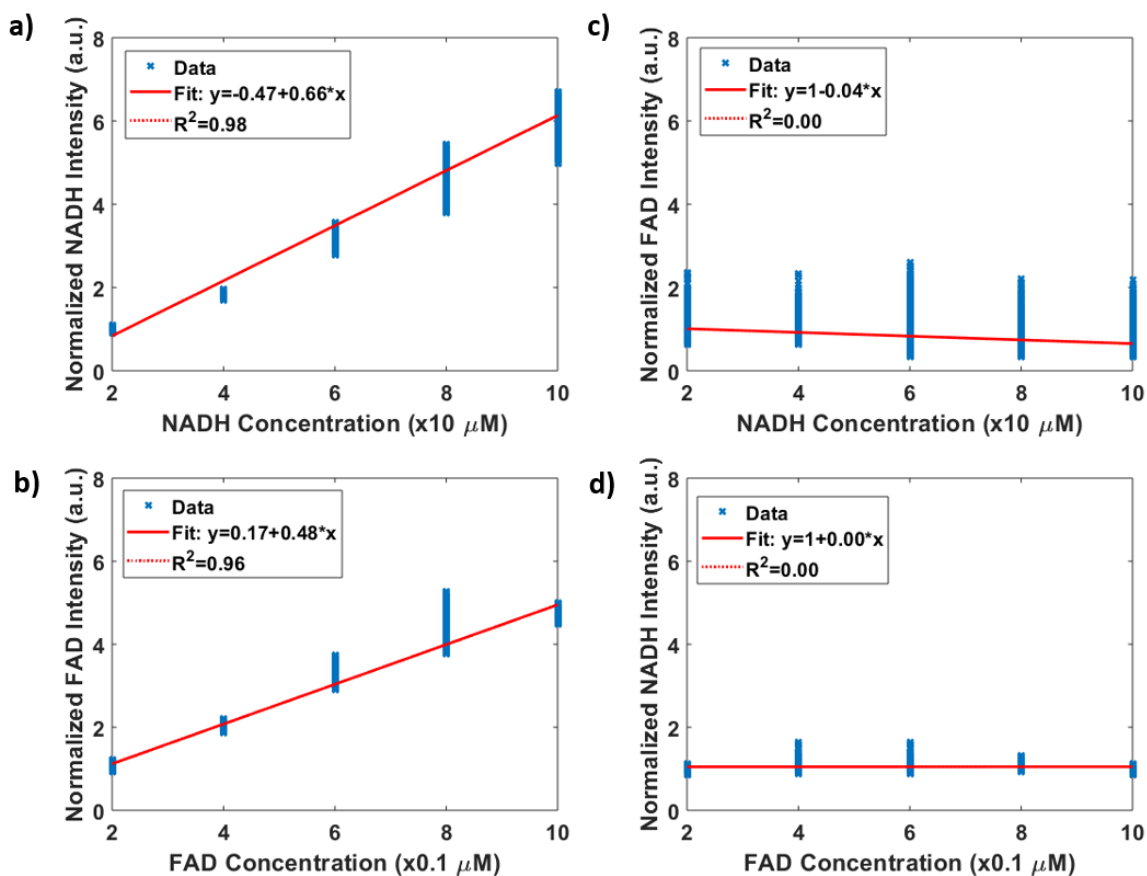


Figure 13) The results of the linearity test for the fluorescence imager using exogenous NADH and FAD solutions: the NADH (a) and FAD (b) response of the system to the increase in NADH concentrations. The NADH (c) and FAD (d) response of the system to the increase in FAD concentrations. The fitted linear regression is shown as a line, and the R2 values are included in the legends. The *in vivo* fluorescence imager used in our study is linear in the biologically relevant concentrations of NADH and FAD, and there is no cross-relation between the two channels. NADH, nicotinamide adenine dinucleotide; FAD, flavin adenine dinucleotide

## 2.2. Fluorometer

A complete description of the implementation and the design of the fluorescence imaging system can be found in our previous study [82, 83]. The fluorometer is a fiber-optic-based optoelectronic fluorometer, designed and developed in the Biophotonics lab. It is used to monitor the concentration of autofluorescence electron carrier, NADH and FAD. The fluorometer is equipped with two synchronized filter wheels, a bifurcated fiber optic bundle, and one photomultiplier tubes

(PMT) for signal detection in NADH and FAD channels. The filter wheels communicate with the computer through a control box (Lambda- 3, Sutter instrument, CA). The bifurcated fiber bundle consists of high-grade fused silica fibers for UV transmission (Newport instrument, NJ) with a distal end of 3 mm inner diameter. For fluorescence spectroscopy, the peak energy of the NADH and FAD excitation spectrum occurs at 365 nm and 436 nm, respectively. The emission filters for NADH and FAD fluorescence are set at 455nm and 525nm, respectively. The fluorometer was

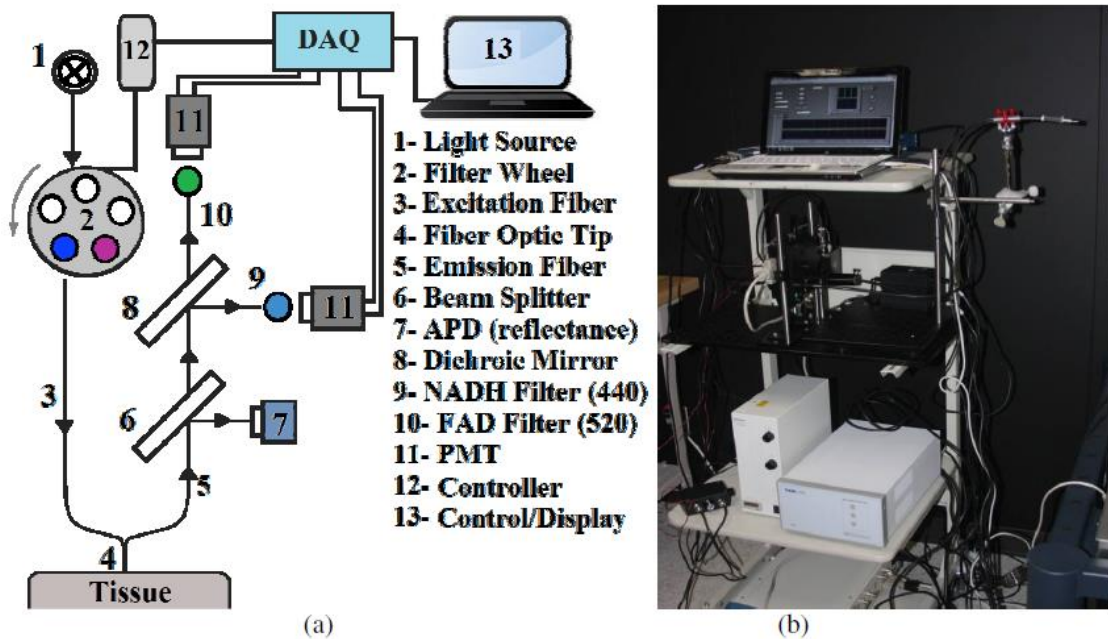


Figure 14: The schematic of fluorometer (a) and previous actual implementation (b) of the fluorometer.

used to acquire surface fluorescence signals from NADH and FAD by placing the fiber optic probe against the desired tissue.

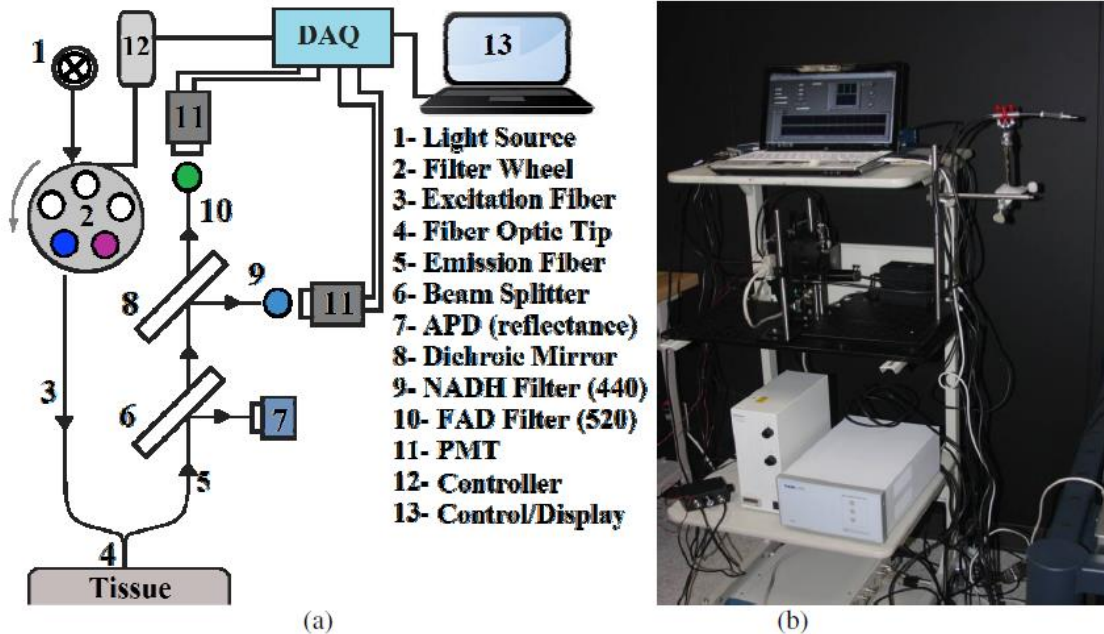


Figure 14 shows the schematic and the previous actual implementation of this device.

### 2.2.1. Hardware Upgrade

The light source in the previous design of the fluorometer was a mercury arc lamp (Intensilight, Nikon, Tokyo, Japan). Due to reasons such as speed, phototoxicity, environmental green and lower cost that is discussed in detailed before (2.1.1), we replaced the light source by Xcite LED1 (Excelitas Technologies Corp., Waltham, MA, USA) with 4 switchable wavelengths.

### 2.2.2. User interface upgrade

A LabVIEW user interface was developed for fluorometer, to control PMT gain, filter wheel synchronization, and data acquisition. However, this user interface was not able to communicate with Xcite LED1. Therefore, we developed a LabVIEW subVi called XLED and implemented it

in the original LabVIEW program and changed the main code so it would be able to communicate with Xcite LED. However, to concise, only the XLED subVi will be discussed.

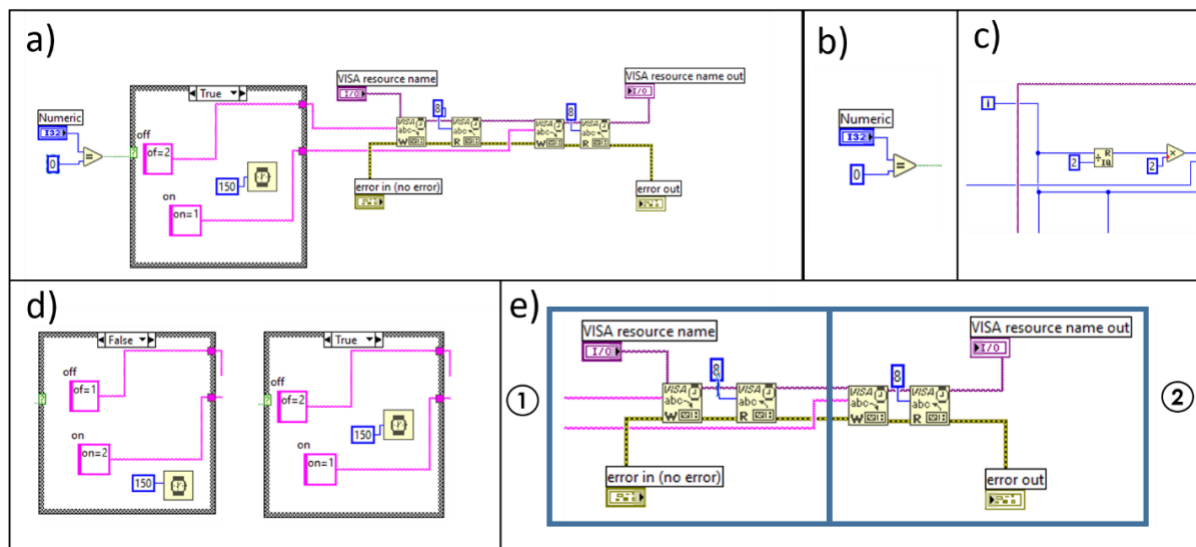


Figure 15a shows the overall background code of XLED subVi. The “Numeric” icon in

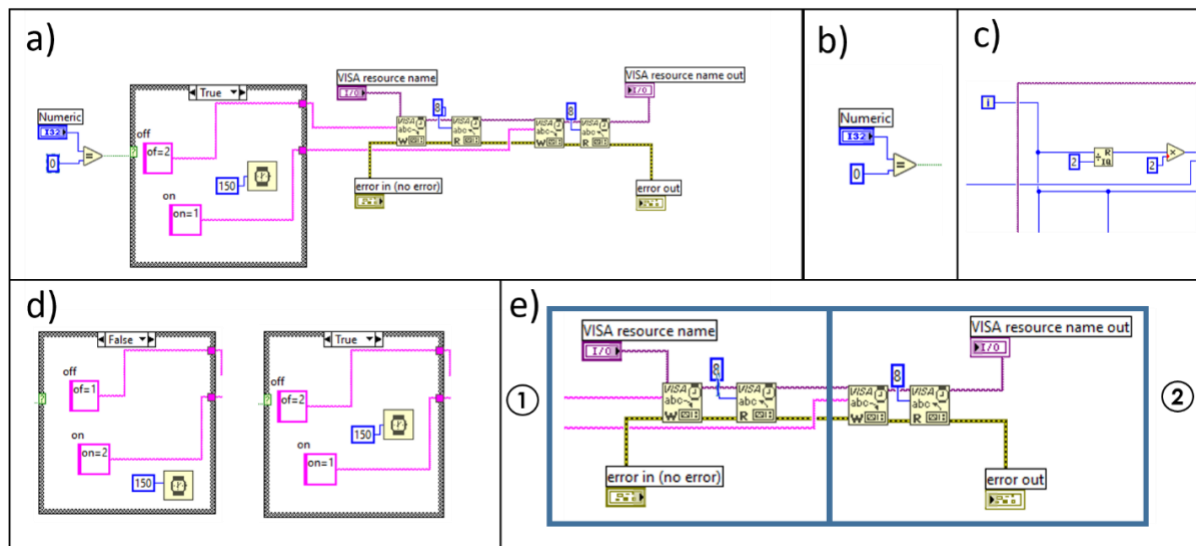


Figure 15b defines whether a signal is received from NADH or FAD. It gets this information from the icon “i” show in

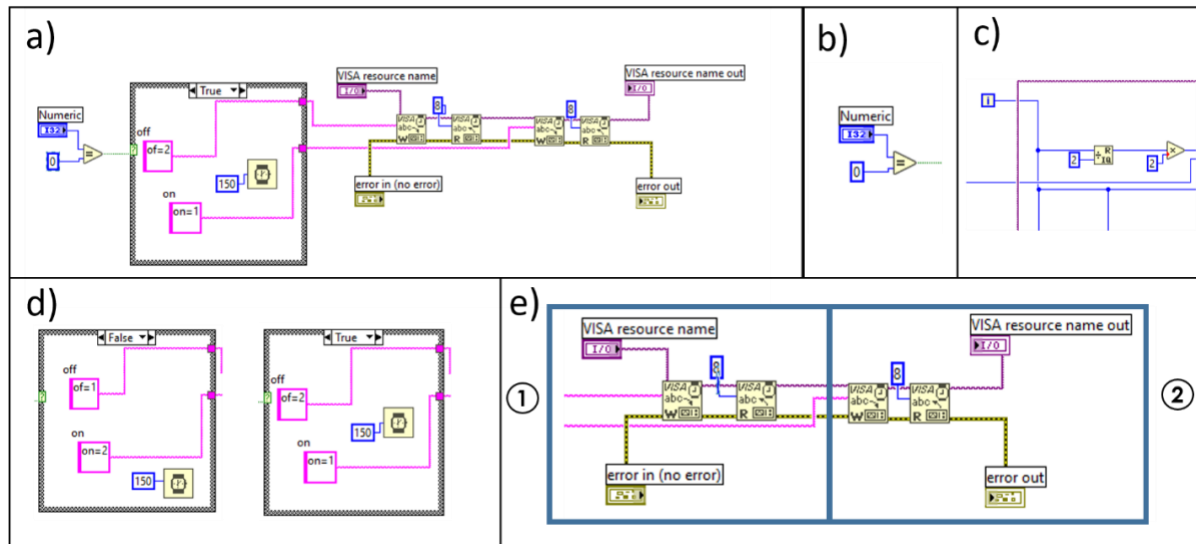


Figure 15c from the main code. “i” is the number of iteration (the number of times that the while loop in the main program has been executed). In each loop, the filter wheels rotate to go to the location of either FAD or NADH and this information is passed on to XLED Vi through the “Numeric” icon.

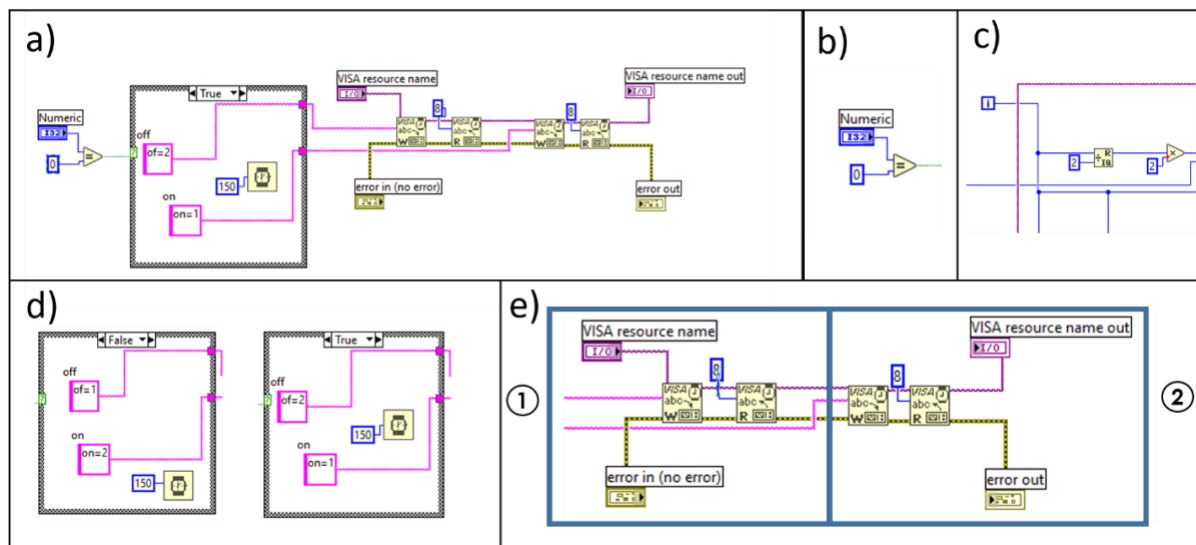


Figure 15d shows a True or False Case Structure in LabView. This structure will send the orders from the “False” Case Structure if the excitation source is set to excite NADH and it will send the orders from “True” if the excitation source is set to excite FAD. "Visa Write" and "Visa Read" in

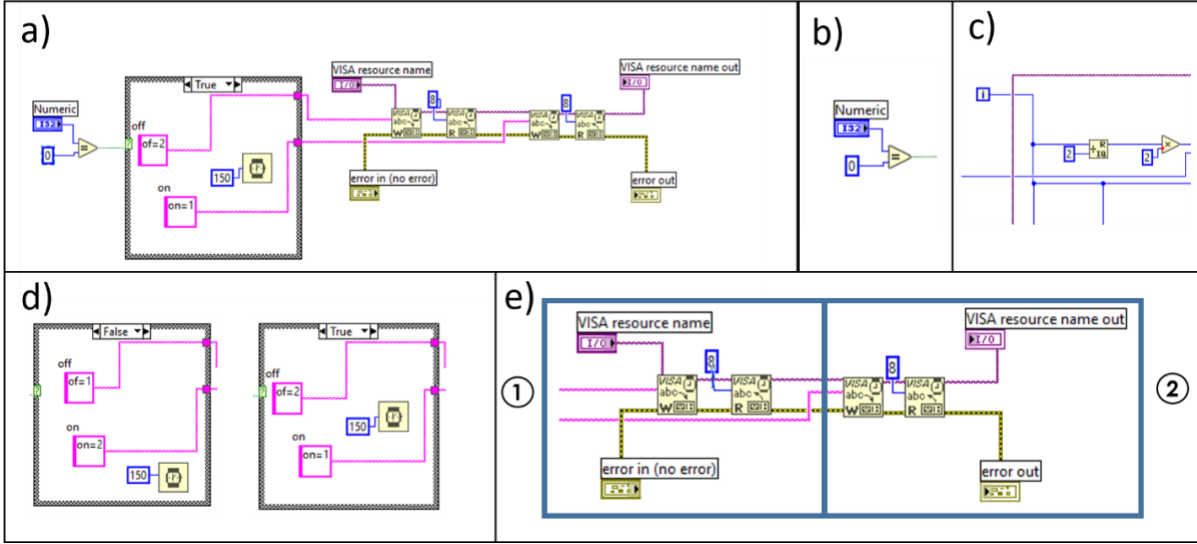


Figure 15e will execute the commands that have been produced in the case structure to turn the

desired XLED light sources off and on. Part 1 in figure 15.e will turn the undesired excitation light off and part 2 will turn the desired excitation light on.

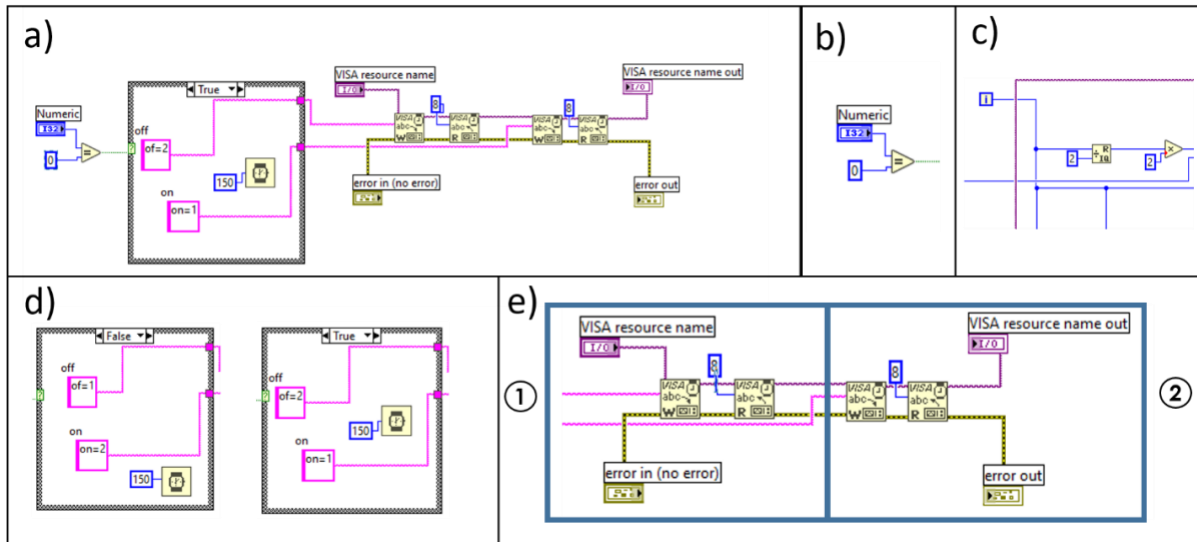


Figure 15: Background cod of XLED SubVi.

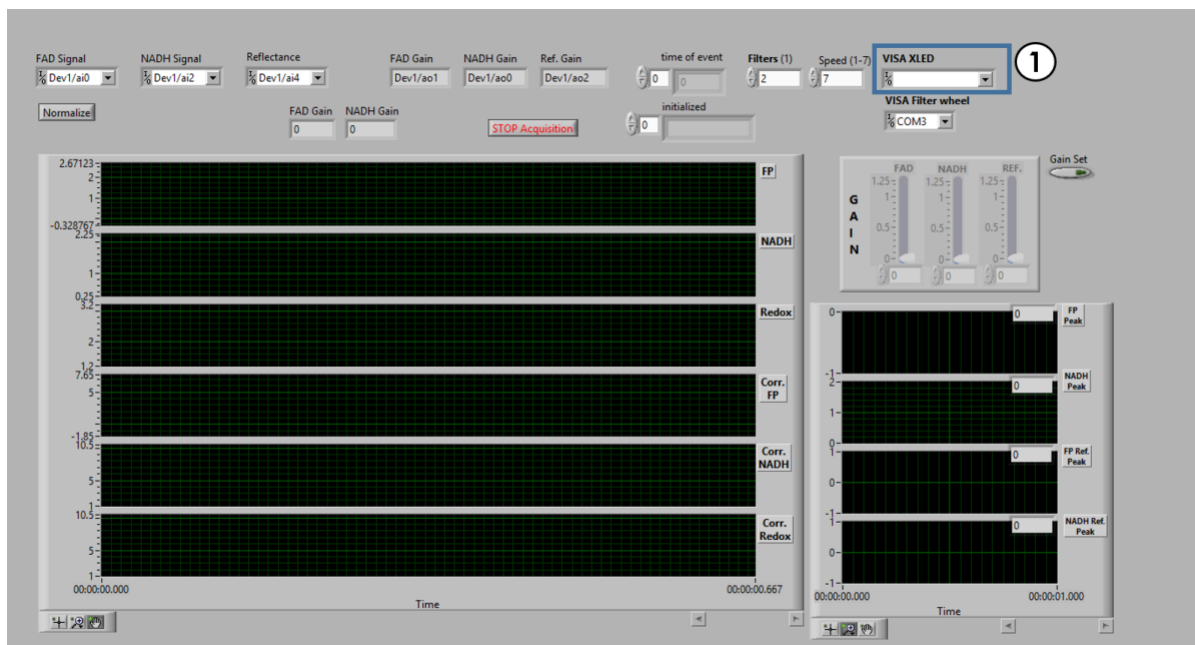


Figure 16 is showing the upgraded front panel for the fluorometer. Part 1 in figure15 is added to the front panel so Xcite LED1 will communicate with the PC.

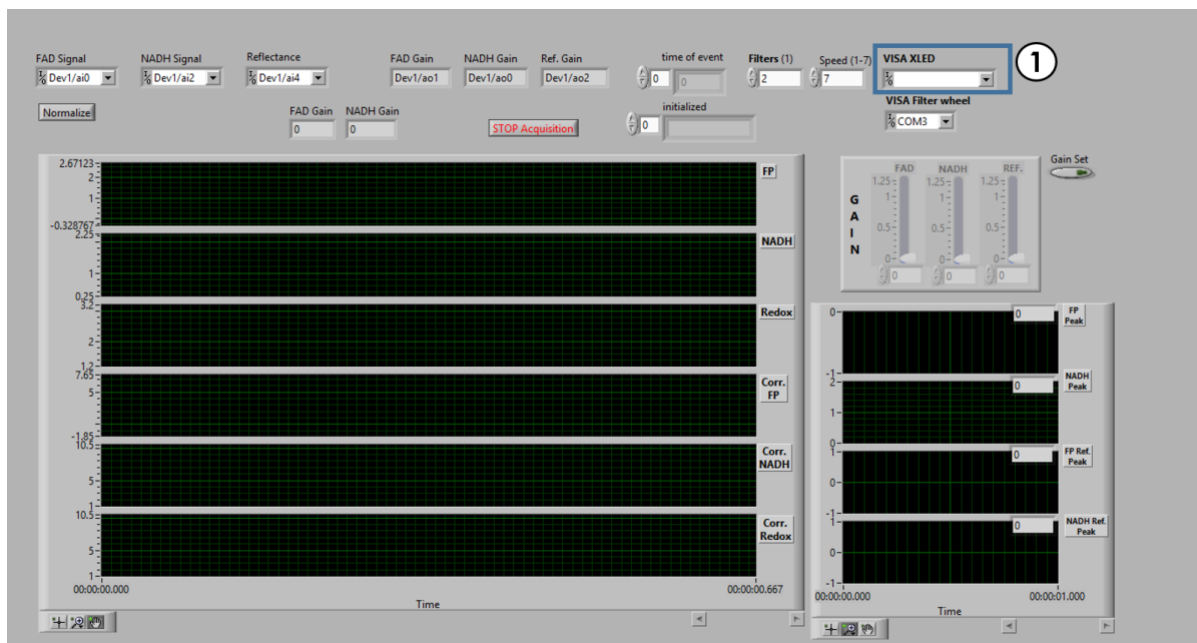


Figure 16: The upgraded control panel for the fluorometer.

# **Chapter 3**

***In vivo* and 3D fluorescence imaging**

### **3. *In vivo* and 3D fluorescence imaging**

In what follows, the result of our study on the effect of 670 nm photo-biomodulation on diabetic mice wounds, using the *in vivo* fluorescence imager is discussed. As explained before, the excitation light source in the second version of the *in vivo* fluorescence imager is Xcite LED1 (Excelitas Technologies Corp., Waltham, MA, USA). Xcite LED1 excites the autofluorescence coenzymes of the surface of the wounds, NADH and FAD, through a fiber-guiding light. Xcite LED1 produces the appropriate excitation wavelength for NADH and FAD with a peak at 385 nm and 460nm, respectively. The emitted light from the wounds passes through a set of optical filters inserted in a filter wheel. NADH and FAD emission filters were set at 460 nm (50-nm bandwidth) and 537 nm (50-nm bandwidth), respectively. A neutral density filter (ThorLabs, NJ) was also used as the emission filter for white field imaging. A single channel stepper motor was used as the filter wheel controller to synchronize the produced excitation light with the appropriate emission filter. Finally, a charged charge-coupled device (CCD) camera (QImaging, Retiga R6) captures the filtered emitted light and save the result as a .tiff file.

#### **3.1. *In vivo* fluorescence imaging of diabetic wounds**

The objective of this study is to investigate the effect of far-red photo-biomodulation (PBM) on the wound healing process by tracking the changes in the ratio of the mitochondrial bioenergetics (NADH /FAD) or redox ratio (RR).

Wound healing is a complex and dynamic biological process that involves overlapping phases of hemostasis, inflammation, proliferation, and remodeling [84]. Excessive and uncontrolled oxidative stress has been shown to contribute to a perpetual inflammatory state, deregulate the

healing process; thus, playing a central role in the pathogenesis of chronic non-healing wounds [55, 85]. Photobiomodulation (PBM) by far-red (FR) to near-infrared (NIR) light has been demonstrated to accelerate diabetic wound healing in preclinical and clinical studies. FR/NIR photons interact with the mitochondrial photo-acceptor molecule, cytochrome c oxidase (CcO), the terminal electron acceptor of the electron transport chain (ETC) [86, 87]. This interaction modifies NADH linked dehydrogenase reactions [88] and alters the rate of ADP/ATP exchange [89], resulting in improved mitochondrial bioenergetics and activating intracellular signaling pathways that decrease chronic inflammation and promote healing [90]. Imaging NADH and FAD, two autofluorescence mitochondrial metabolic co-enzymes, is one of the methods vastly used to study mitochondria bioenergetics. Our *in vivo* fluorescence imager enables us to capture the real-time metabolic images (by capturing the surface fluorescence of NADH and FAD) of the wounds *in vivo*. The redox ratio (NADH/FAD) serves as a quantitative indicator of the mitochondrial redox state [31, 44, 91]. In the current study, the fluorescence imager is utilized to test the hypothesis that PBM would accelerate the healing process in the db/db mice model of diabetes by affecting the mitochondrial redox state.

### **3.1.1. Experimental Protocol**

The conducted experiments were approved by the Institutional Animal Care and Use Committee (IACUC) at the University of Wisconsin Milwaukee. Genetically diabetic mice (*db/db*<sup>-/-</sup> mice; BKS.Cg-Dock7m <sup>+/+</sup> Lepr<sup>db/J</sup>), 8 weeks of age were obtained from Jackson Laboratories (Bar Harbor, ME) and used in this study. After confirming a hyperglycemic state, the mice went through wound induction surgery. A 10 mm full-thickness excisional wounds were generated on either side of the mouse's midline at the level of the shoulders using a disposable sterile 4 mm biopsy punch

and iris scissors. General anesthesia was induced using 4% isoflurane in 100% oxygen (flow rate 1 L/min), and the anesthesia was maintained using 1–3% isoflurane during the surgery.

Light treatment of the induced wounds was performed using 670 nm LED arrays engineered to eliminate heat (670±10 nm GaAlAs LED arrays (75 cm<sup>2</sup>), Quantum Devices, Barneveld, WI). Diabetic db/db mice were randomly assigned to 670 nm PBM (FR-PB, n=6) or sham treatment (Sham group, n=5) groups. Treatment consisted of positioning the 670 nm LED array 1–2 cm directly above the wound surface and irradiating the wound for 90 seconds at an irradiance of 60 mW/cm<sup>2</sup> once per day for five days per week to deliver a dose (radiant exposure) of 4.5 J/cm<sup>2</sup> at the wound surface for each treatment. Sham-treated mice had the LED array positioned above the wound for 90 seconds, but the LED array was turned off.

### **3.1.2. Time-line and tissue preparation**

A total of 16 diabetic mice were involved in this investigation, all of which went through the wound induction surgery. Except for 5 of them that were sacrificed after collecting biopsies for cryo-imager (3.2.1.1), the rest (a total of 11) received far-red Photobiomodulation treatment and were imaged by *the in vivo* fluorescence imager. *In vivo* fluorescence imaging was performed on days 0, 3, 6, and 9 post-wounding on the remaining group of mice (n=6 FR-PBM, n=5 sham-treated). The imaging of wounds was performed right after receiving the 670 nm photobiomodulation. Therefore, there was no interference of PBM in the imaging procedure, and the NADH and FAD excitation/emission did not interfere with the effect of 670 PBM on the wound healing process.

### **3.1.3. Image processing**

The image processing was performed using MATLAB. Using the *in vivo* fluorescence imager, images of the wounds on diabetic mice were acquired from white field, NADH and FAD channels. First, to minimize the day-to-day variation of light intensity, the NADH and FAD images were calibrated by images of two cuvettes containing 50 $\mu$ M NADH and 0.5 $\mu$ M FAD solutions, respectively. Second, the white filed images were used to determine the outline of the wounds, and then it was masked on the images from NADH and FAD channels. Then, the redox ratio of the wounds (RR = NADH/FAD) was calculated pixel by pixel. The mean of RR histograms was considered as the quantitative marker, called Surface RR and it is calculated by using Equation 1.

$$RR = \frac{1}{N} \sum(\text{wound pixels}) \quad \text{Equation 1}$$

The wound area can be approximated by the number of wound pixels multiplied by pixel size and by using Equation 2 we can calculate the normalized wound area.

$$\text{Normalized Wound Area} = \frac{PS(t) \times N(t)}{PS(0) \times N(0)} = \frac{N(t)}{N(0)} \quad \text{Equation 2}$$

Where N(t) is the number of wound pixels at day t. N(0) is the number of wound pixels at day 0, i.e., the initial wound area. PS(t) is the pixel size at day t, and PS (0) is pixel size at day 0. Since the pixel size remained unchanged, we can remove it from the denominator and nominator. This simplifies the equation, so the normalized wound area is equal to the number of pixels at day t to the number of pixels at day zero.

### 3.1.4. Results

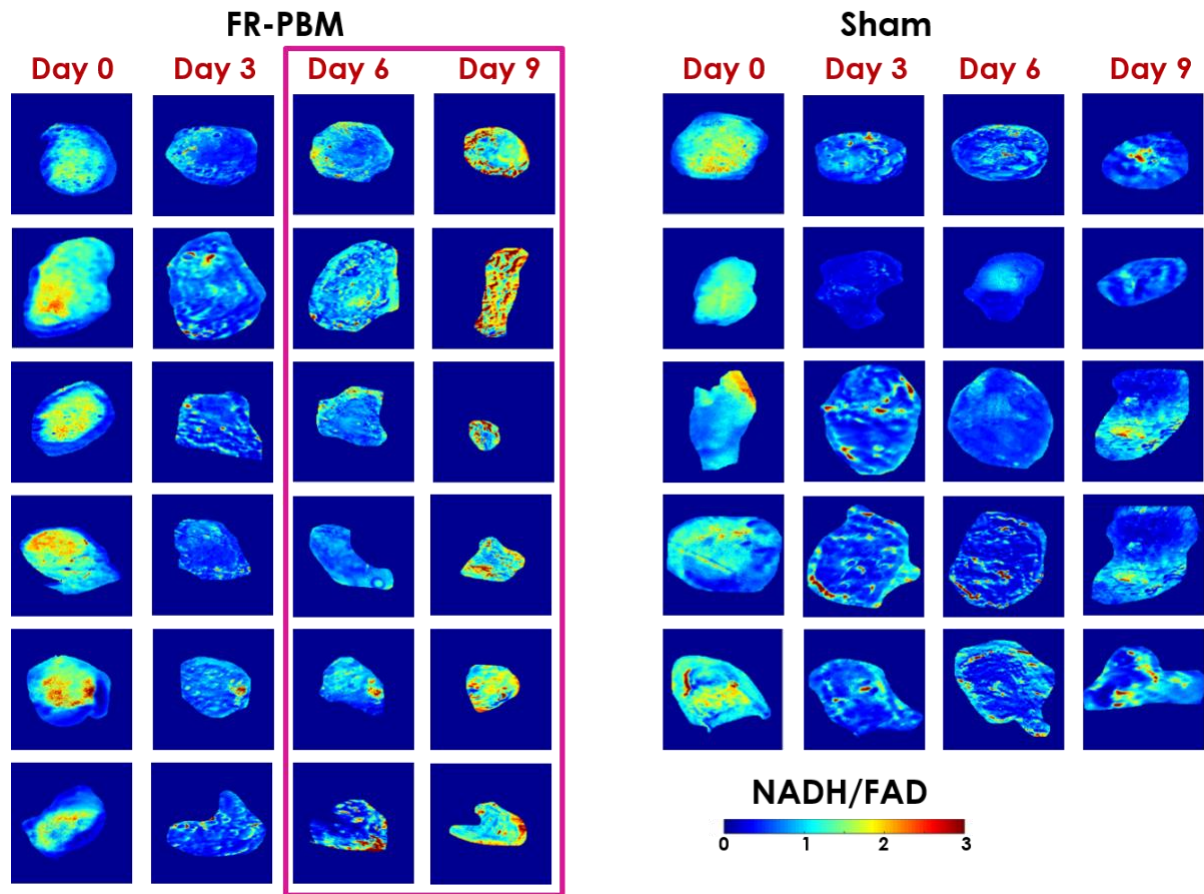


Figure 17 shows the on-line temporal fluorescent redox images of FR-PBBM and Sham treatment groups on days 0, 3, 6 and 9 of the experiment. The data in

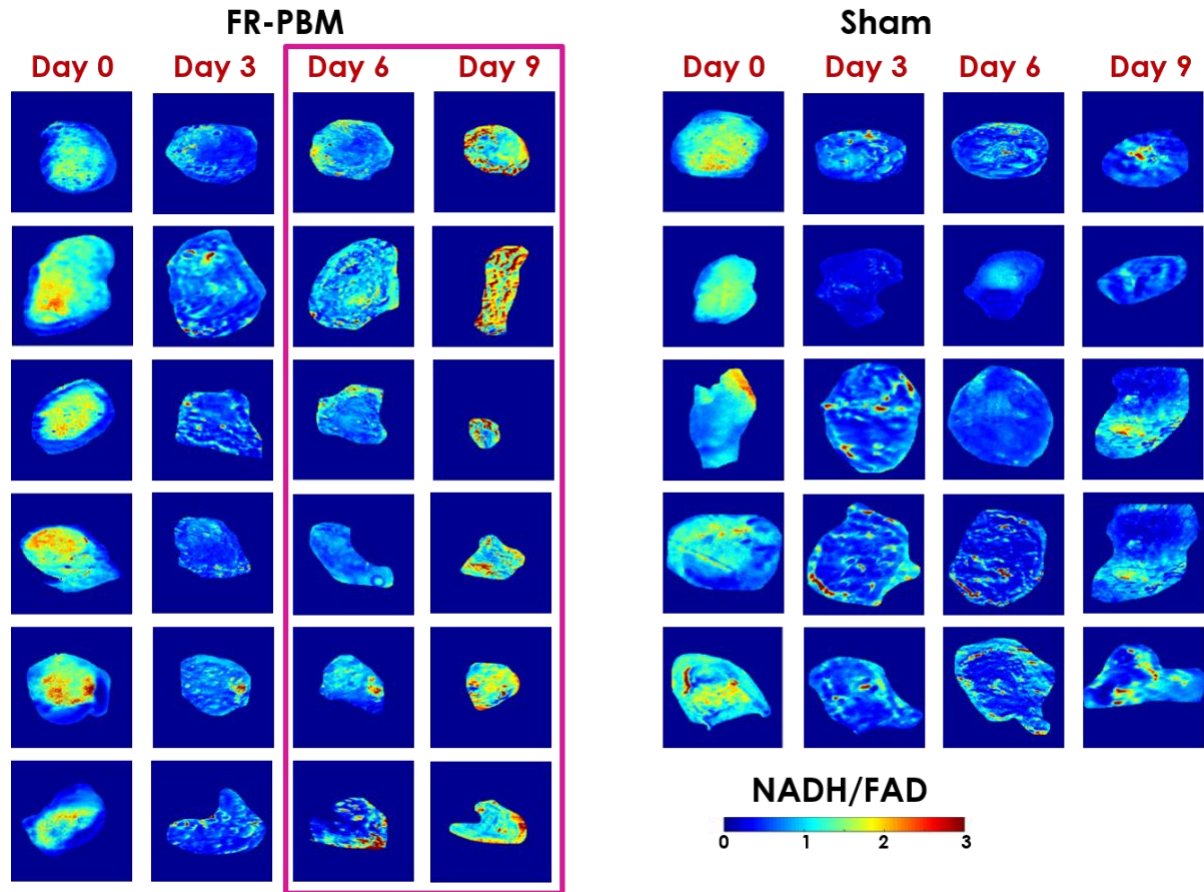
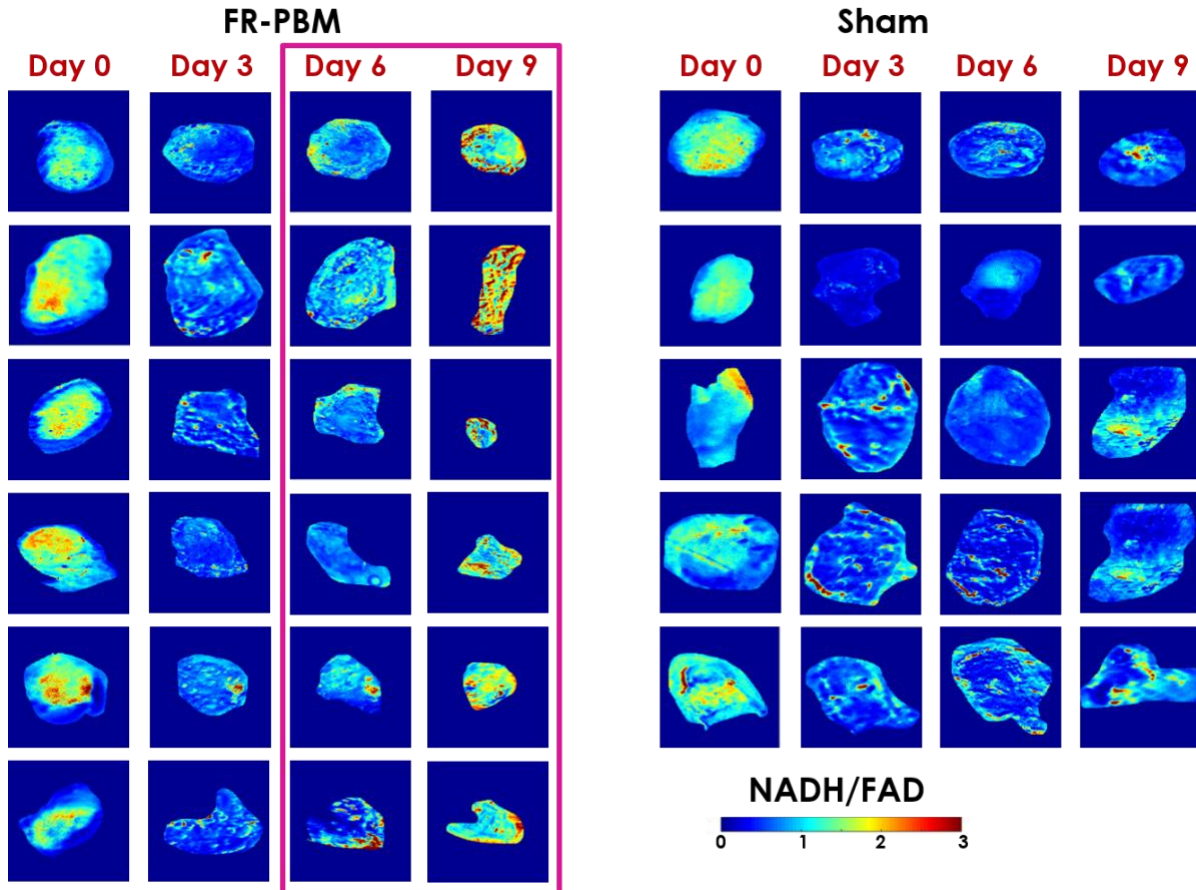


Figure 17 at days 6 and 9 show that the RR in the FR-treated wounds is greater than the RR measured in sham-treated mice. This reflects an increase in NADH and a decrease in the FAD

concentrations of the FR-treated wounds over time, resulting in a visibly greater RR at days 6 and 9.



**Figure 17: Representative *in vivo* fluorescence images of NADH, FAD, and the tissue redox ratio (NADH/FAD) for representative wounds over days:** unlike the wound on the sham-treated mice, the FR-PBM treatment increased the NADH intensity of the wounds and decreased the FAD intensity. Therefore, at days 6 and 9 of post wounding, the wound on FR-PBM mice showed a higher redox ratio in comparison with sham-treated mice. NADH, nicotinamide adenine dinucleotide; FAD, flavin adenine dinucleotide; FR, far-red; PBM, photobiomodulation.

Table 1 presents the data and the statistical analysis for FR-PBM and sham-treated groups of mice over the time course of the experiment. Surface RR and wound area were obtained using *in vivo* fluorescence imager, and their corresponding changes over time are the RR change rate and closure rate, respectively. In more detail, The RR change rate is the difference between the mean RR of samples in two consecutive data collection days. This biomarker is used to evaluate the temporal

differences in the *in vivo* RR changes at different days. A negative value of the RR change rate corresponds to a descending trend in the RR, i.e., a drop in the RR by a decrease in mitochondrial redox state and an increase in oxidative stress. The wound closure rate was defined as the difference in wound area between two consecutive data collection days and was used to determine the rate of wound healing. The closure rate provides a quantitative index of wound healing over time. A positive value in the closure rate corresponds to a decrease in the wound area, and a negative value of the closure rate corresponds to an increase in the wound area.

FR-treatment resulted in a notable increase in Surface RR at days 6 and 9, but the change rate of surface RR became significant by day 9. Thus, over the time course of the experiment, the mitochondrial redox state of the wounds in the FR-PBM group increased at a faster rate than the sham-treated group.

*Table 1* : Quantitative assessment of FR-PBM (*in vivo*): the surface RR, RR change rate, normalized wound area, and closure rate are calculated by *in vivo* fluorescence imager.

		<b>Day0</b>	<b>Day3</b>	<b>Day6</b>	<b>Day9</b>
<b>Surface RR</b>	FR-PBM	1.01 ± 0.07	0.46 ± 0.03	<b>0.55 ± 0.05*</b>	<b>1.26 ± 0.07*</b>
	Sham	1.08 ± 0.07	0.47 ± 0.05	0.36 ± 0.06	0.67 ± 0.04
<b>RR change rate</b>	FR-PBM	-	-0.54 ± 0.07	0.09 ± 0.05	<b>0.71 ± 0.08*</b>
	Sham	-	-0.61 ± 0.11	-0.05 ± 0.06	0.25 ± 0.04
<b>Normalized wound area</b>	FR-PBM	1	<b>0.87 ± 0.08*</b>	<b>0.82 ± 0.02*</b>	<b>0.61 ± 0.09*</b>
	Sham	1	1.32 ± 0.14	1.26 ± 0.09	1.08 ± 0.11
<b>Closure rate</b>	FR-PBM	-	<b>0.13 ± 0.08*</b>	0.05 ± 0.06	0.21 ± 0.11
	Sham	-	-0.32 ± 0.14	0.06 ± 0.10	0.18 ± 0.11

### 3.2. 3D fluorescence Cryo-imager

3D fluorescent cryo-imager was custom-designed at Biophotonics Lab, University of Wisconsin Milwaukee. This instrument has been described in detail in our previous studies [31, 32, 48]. This

device captures the metabolic state of the tissue at the cryogenic temperature. The system has a mercury arc lamp as the excitation light source (200 W lamp, Oriel, Irvine, CA, in the light source from Ushio Inc., Japan). The light passes through a filter wheel, which has NADH (350 nm with 80 nm bandwidth) and FAD (437 nm with 20 nm bandwidth) optical filters. The light is air-guided toward the sample, and emitted light passes through the emission filter wheel, which contains the specific emission filters for NADH (460 nm with 50 nm bandwidth) and FAD (537 nm with 50 nm bandwidth). Then, the images will be acquired using a CCD camera (QImaging, Aqua) from the filtered emitted photons. A microtome blade cuts through the sample with a specified thickness (varies based on each study), and the images are captured sequentially.

### **3.2.1. Metabolic imaging of Diabetic wounds**

#### **3.2.1.1. Experimental Protocol:**

A total of 16 diabetic mice were involved in this study, all of which went through wound induction surgery. Five of them were sacrificed immediately after biopsies of wounds for cryo-imaging at day 0 were collected. The harvested wound samples were flash frozen. Moreover, at the end of the experimental protocol, on day 9 of post-wounding, the entire wounds were excised and snapped frozen immediately. All 16 frozen biopsies were then imaged by cryo-imaging for the volumetric redox study.

#### **3.2.1.2. Image processing:**

The cryo-images were processed using MATLAB. NADH and FAD images were calibrated with images captured from a flat field for NADH and FAD channels, respectively. The background (low-intensity) voxels were set to zero, and 3D redox images were obtained by calculating the RR

for each voxel. The mean of RR histograms was considered as the quantitative marker, called Volumetric RR.

### 3.2.1.3. Results:

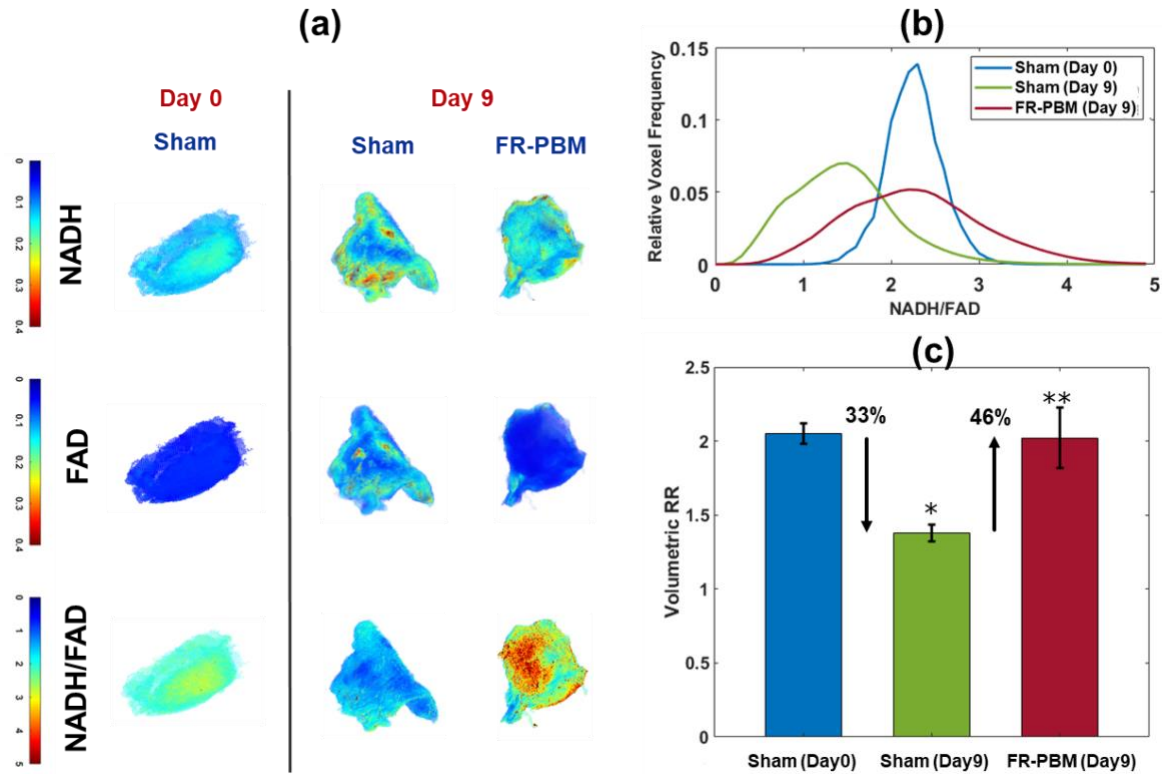


Figure 18a shows representative 3D rendered cryo-images captured from the biopsies collected at the beginning and the end of the experimental protocol. The color-coded images of wound biopsies show higher NADH and lower FAD in the FR-PBM group in comparison with the sham-treated group, resulting in a higher volumetric RR.

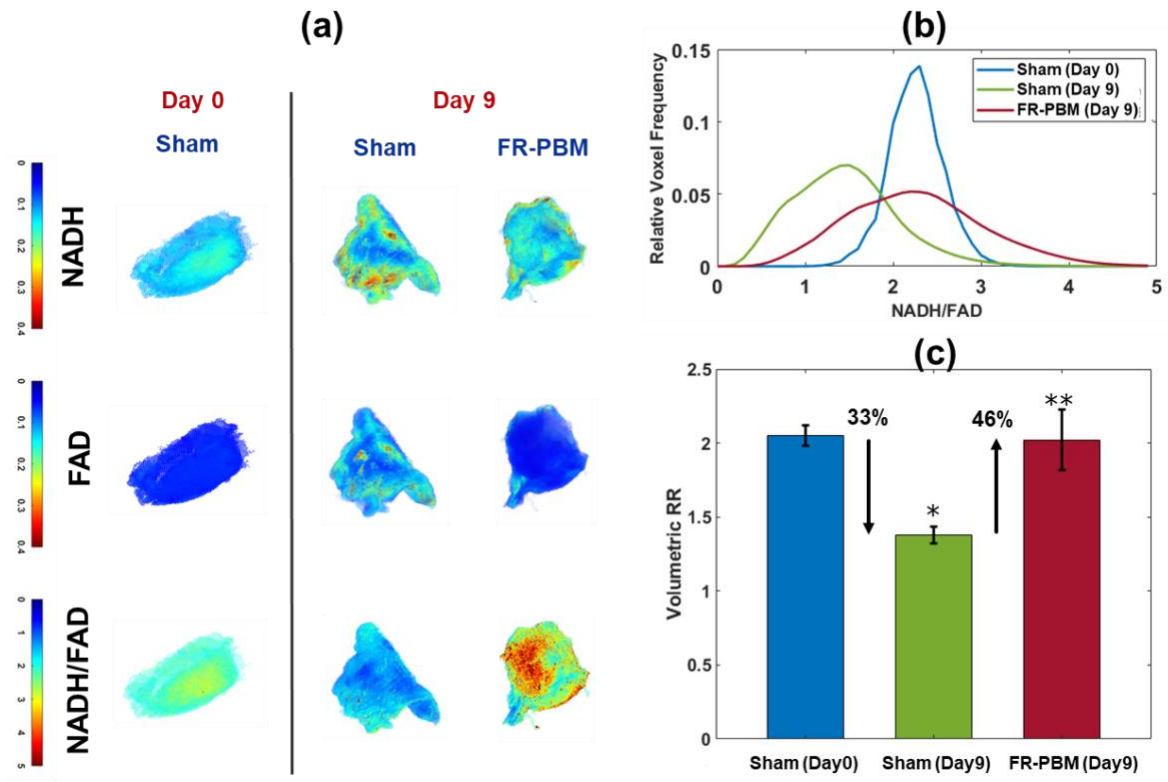
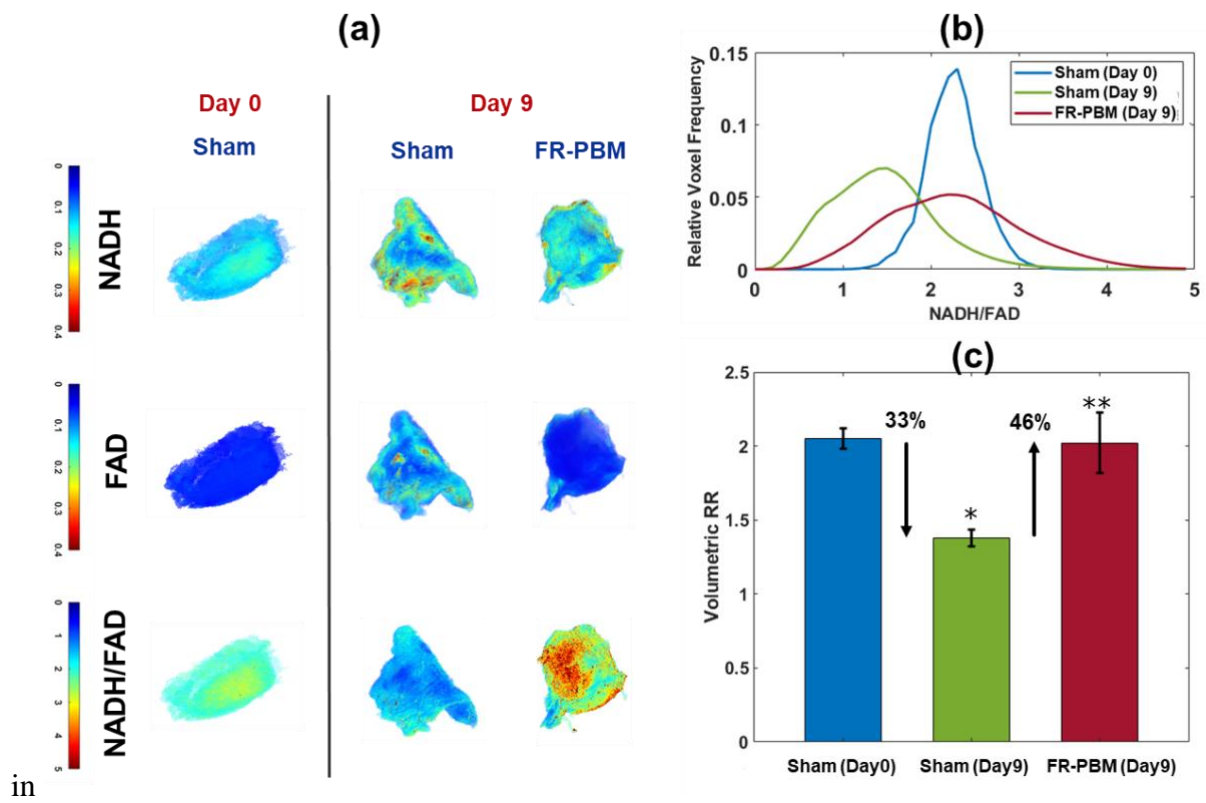


Figure 18b illustrates the histograms of the corresponding RR images, as shown



in

Figure 18a. The histogram of sham-treated wounds at day 9 has shifted to the left when compared to the day 0 wound histogram. Also, it shows that the histogram of sham-treated wounds at day 0 and FR-PBM wounds at day 9 are centered almost at the same place, but the histogram of FR-PBM is more widely distributed. It means in the wounds of the day-0 sham-treated group; the redox ratio was more uniform over the wound biopsies. However, the redox ratio in the wounds of the day-9 FR-PBM group is unevenly distributed over the wounds. It can suggest that although by day 9 the FR-PBM wounds are manifesting successful wounds healing, to observe better results, receiving more dosage of FR-PBM might be needed. The mean volumetric RR  $\pm$  standard deviation in three groups of wounds is shown

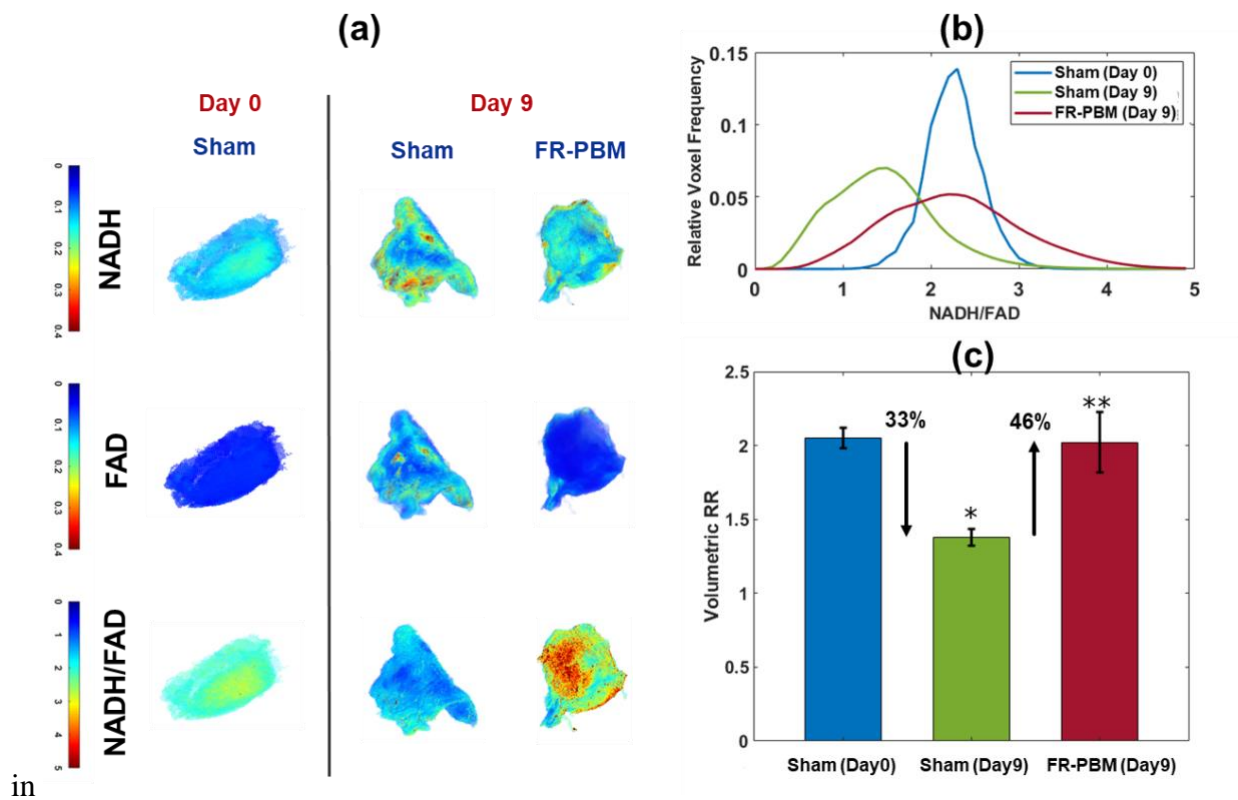
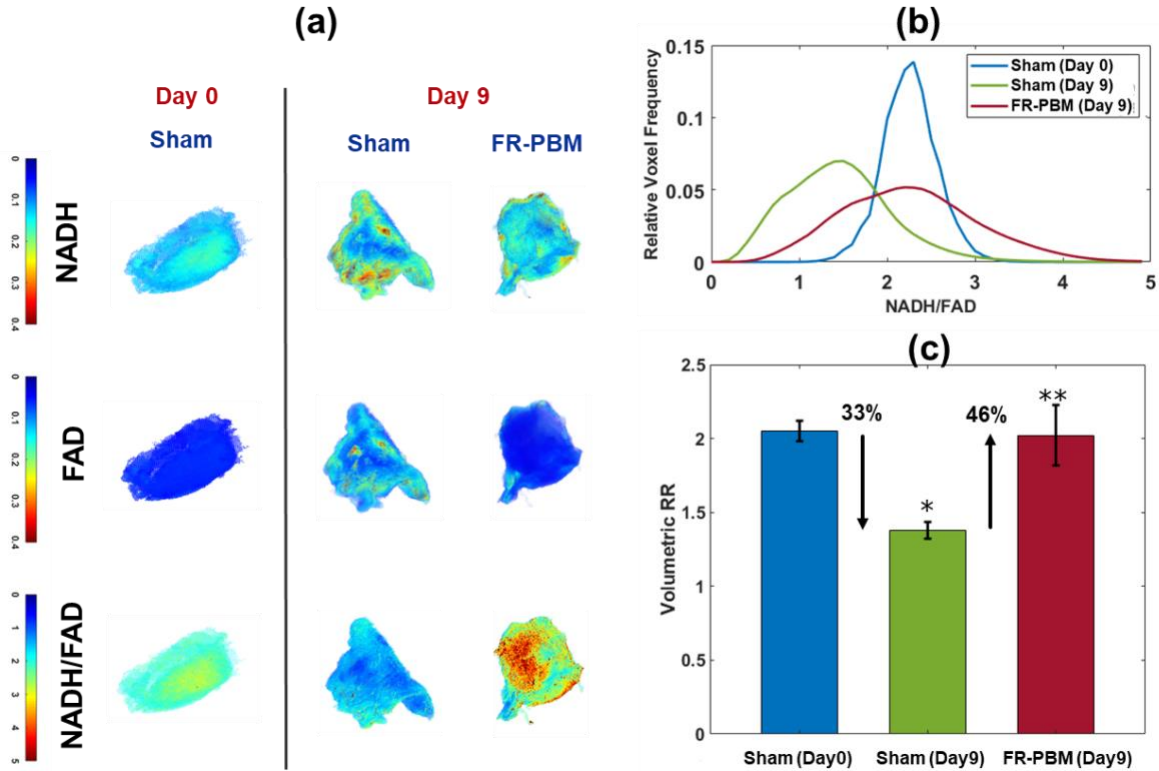


Figure 18c. The Volumetric RR of sham-treated wounds on day 9 significantly dropped by 33% when compared to the sham-treated mice on day 0. Also, FR-PBM caused a significant 46%

increase in the volumetric RR of wounds on day 9 when compared to the sham-treated wounds on day 9. This observation confirms the data that was obtained from the *in vivo* fluorescence imager.



**Figure 18: The cryo-imaging results of sham-treated vs. FR-PBM treated wounds.** (A) Representative fluorescence cryo-images of NADH, FAD, and the tissue redox ratio (NADH/FAD) for representative wounds are shown at days 0 and 9. (B) The redox ratio histogram of the wounds on the FR-PBM and sham-treated mice. (C) The volumetric redox ratio  $\pm$  standard deviation of representative wounds in bar plots. The wound on FR-treated mice showed a 46% higher redox ratio in comparison with sham-treated controls at day 9 [n=5 sham-treated (day 0), n=5 sham-treated (day 9), and n=6 FR-PBM (day 9)]. \*, significant difference between day 0 and day 9 in redox ratio of sham-treated wounds. \*\*, significant difference between redox ratio of FR-PBM treated vs. sham treated wounds at day 9 of post wounding. NADH, nicotinamide adenine dinucleotide; FAD, flavin adenine dinucleotide; FR, far-red; PBM, photo-biomodulation.

### 3.2.1. Vascular imaging validation:

A 3D vascular detection and segmentation method using autofluorescence imaging was developed in our lab, termed VMI, short for “Vascular-metabolic Imaging”. In this method, the NADH and FAD images that are acquired by cryo-imager to study the metabolic state of an organ are also used to extract its 3D vessel network. The intrinsic NADH and FAD fluorophores illuminate the

foreground of each image, which makes the background vessel networks more distinctive. We hypothesized that the dark voxels are associated with the vasculature because the red blood cells quench the auto-fluorescence signals from NADH and FAD [92]. To validate this method, we coregistered the VMI vessel images with the vessel images extracted from red fluorescence images of a genetically modified rat kidney (TdTomato) with tagged endothelial cells. We also showed that the extracted vessel networks using VMI follows Murray's law. Murray's laws state that when a parent blood vessel branches into daughter blood vessels, the cube of the radius of the parent vessel is equal to the sum of the cubes of the radii of daughter blood vessels. This relation is presented in Equation 3, where  $r_p$  is the diameter of parent vessel lumen and  $r_{d_i}$  is the diameter of the daughter vessel lumen and  $i$  is the number of daughter vessels of a parent vessel.

$$r_p^3 = \sum_{i=1}^N r_{d_i}^3 \quad \text{Equation 3}$$

This law is based on the assumption of constant blood flow and a hypothesis that throughout the vascular system, the sheer force of moving blood on the inner wall is constant. Murray derived this law from a minimum work hypothesis by defining a cost function for the sum of the energy cost of blood in a vessel and the energy cost of pumping blood through the vessel. If vessel radii follow the Murray law, the cost is minimized [93].

Using cryo-imager, the TdTomato transgenics rat kidney was imaged in two channels of fluorescence, NADH (excitation 545, emission 645), and red (excitation 545,147 emission 645). The 3D kidney vessel network of TdTomato rat was extracted from both red fluorescence vessel elements of red channel images and dark vessel element of the NADH channel. To apply Murray's law on the extracted vessels, we used the branch depth as an indicator to differentiate a parent vessel from a daughter vessel. Branch depth is the number of bifurcations in the shortest path, from

the beginning point to a given point in the vessel network. Branch depth increases every time a bifurcation happens in a branch. Equation 4 shows Murray's law based on the branch depth.

$$r_k^3 = \sum_{i=1}^N r_{k+1_i}^3 \quad \text{Equation 4}$$

Where  $r_k$  is the diameter of a vessel at depth of  $k$  (parent vessel) and  $r_{k+1}$  is the diameter of daughter vessel at depth of  $k + 1$  and  $i$  is the number of daughter vessels at depth of  $k + 1$  and  $i$  is the number of daughter vessels at depth  $k + 1$ .

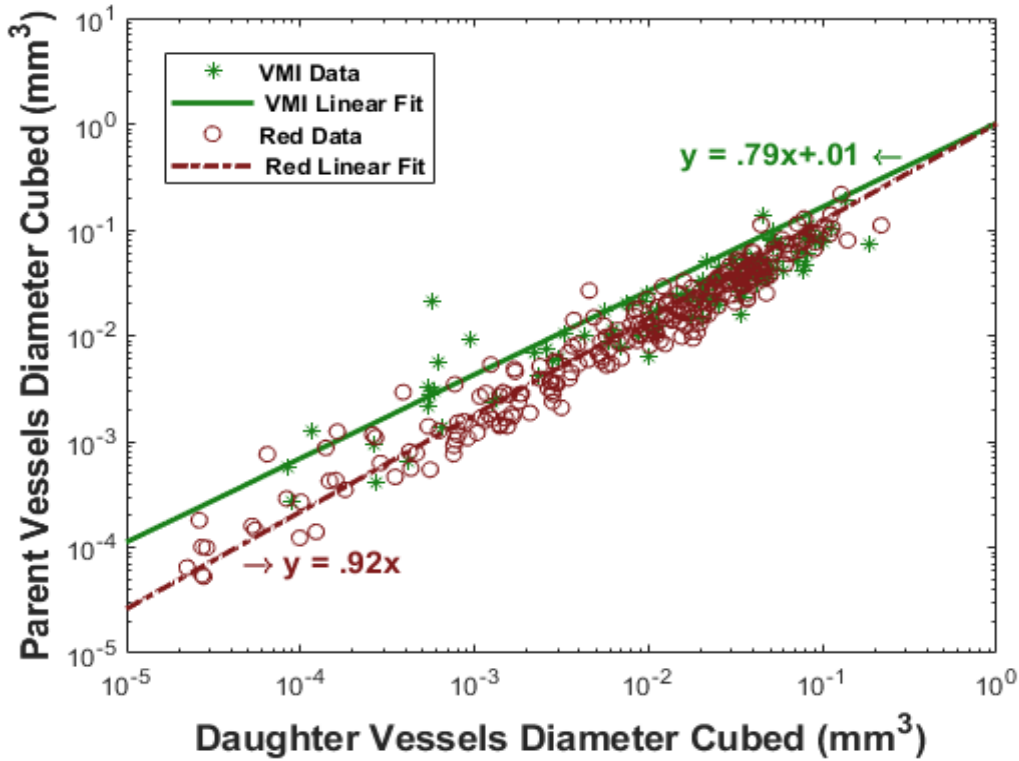
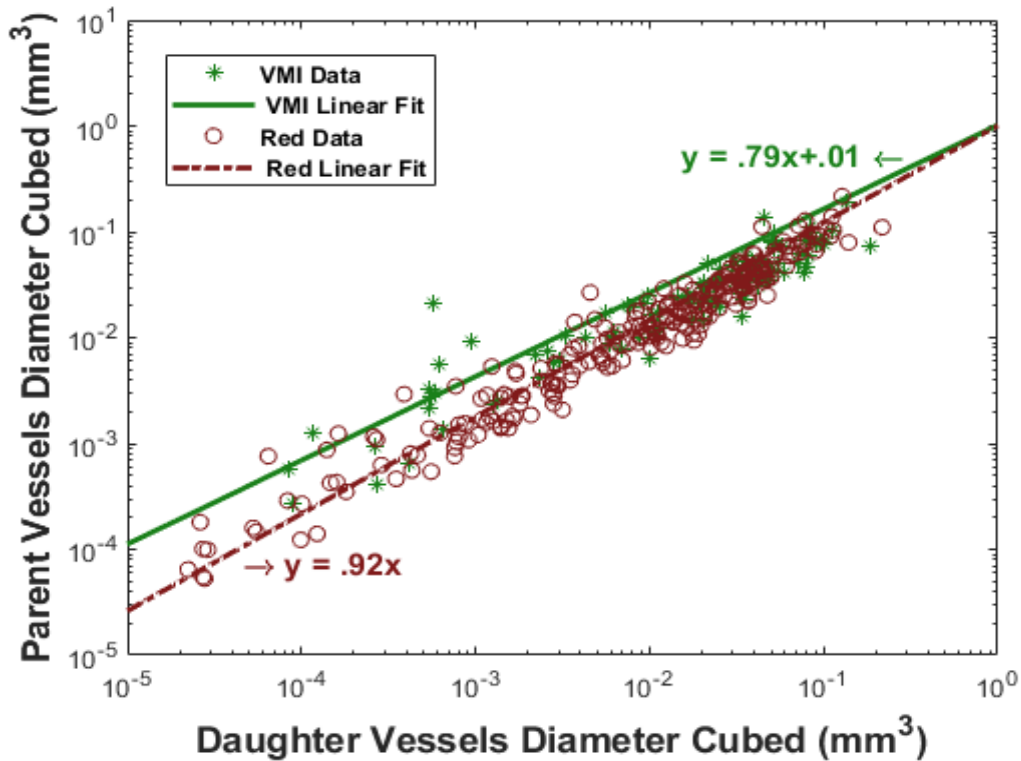


Figure 19 shows the result of applying Murray's law on branching of extracted vessel structures from both NADH and red 3D channels. The VMI Data colored with green is showing the vessel extracted from NADH channel images and the Red Data colored with red is showing the vessels extracted from the red channel images. According to Murray's law, the relationship between the cubed diameter of the parent vessel and summation of the cubed diameter of the daughter should

be fitted to  $y = x$ , i.e., a line with a slope of 1 and y-intercept of 0. Using linear regression, two lines are fitted to each set of data points. The intercept for both lines is approximately zero and the slopes for VMI and red channel are close to 1, indicating that the VMI branching, similar to red vascular branching follows Murray's law successfully.



As

Figure 19 shows, although the slope of fitted lines to data sets of NADH and red channels are close to 1, there is still an error that needs to be discussed. Besides the human artifact and the device artifacts, this error might be induced due to a simplification that we used in defining the parent vessel and daughter vessel. Murray's law works more accurately in the branches where the angle of bifurcation is at least 75 degrees. However, to simplify our calculations, we disregarded the angle of bifurcation and simply assumed that wherever a bifurcation happens the daughter vessels

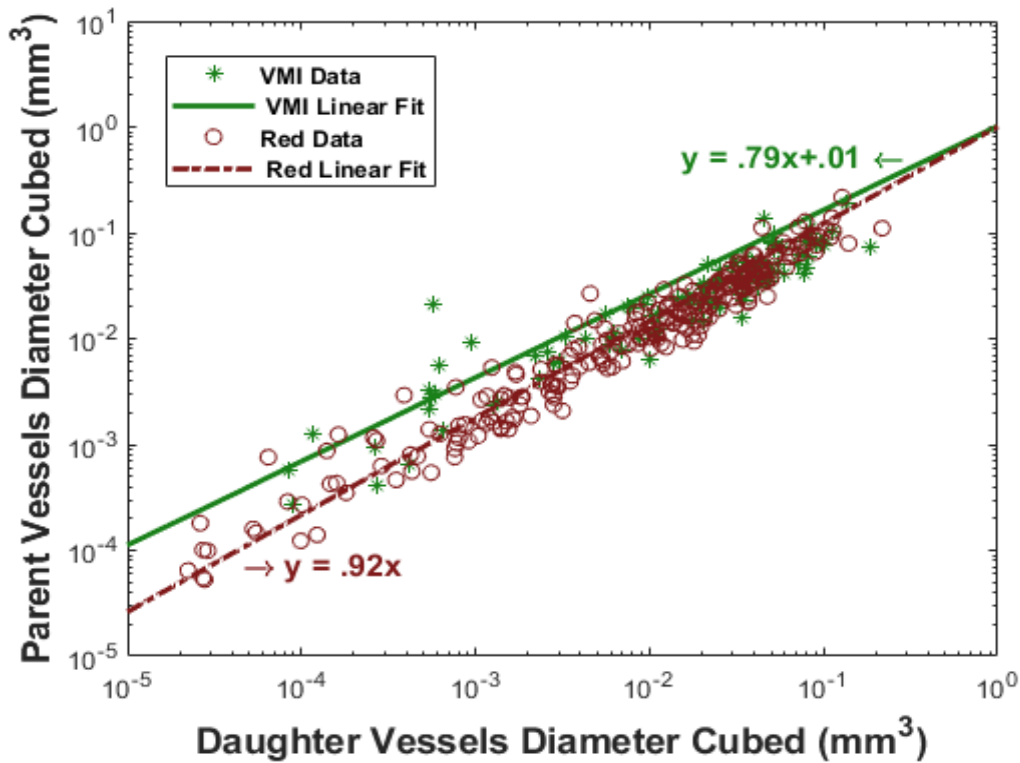


Figure 19: VMI follows Murray's Law. The parent vessel diameter cubed is plotted against the sum of the diameter cubed of their corresponding daughter vessels. The data from red fluorescence of TdTomato rat are shown as red circles, and the data from vasculature extracted using the VMI technique are represented as green stars. Two vascular branching data from VMI and red fluorescence have merged, and their linear regression fit has shown very good compliance with Murray's law (identity line,  $y=x$ ).

are separated from the parent vessels. However, this simplification does not invalidate our method, it just imposes an error on our calculations.

### 3.2.2. Kidney radiation-induced vascular injury

#### 3.2.2.1. Experimental protocol

The animal protocols were approved by the Institutional Animal Care and Use Committees (IACUC) at the Medical College of Wisconsin, Milwaukee. WAG/RijCmcr female rats were irradiated at 12-13 weeks of age (~155 grams). Two groups of rats were randomized. I) non-irradiated (n=12); II) 12.5 Grey leg-out partial body irradiated (leg-out PBI) (n=14). The 12.5

Grey leg-out partial body irradiation (PBI) protocol in rats was the same as that reported in previous studies [94]. Briefly, rats were restrained and irradiated without the use of anesthetics. One hind limb of each rat was carefully externalized and shielded with a 0.25-inch lead block. An XRAD 320KV orthovoltage x-ray system (Precision X-Ray, North Branford, Connecticut) was operated at 320 kVp and 13 mAs with a half-value layer of 1.4 mm Cu with a dose-rate of 1.75 Grey min<sup>-1</sup> for a total dose of 12.5 Gy. Radiation was delivered posterior to anterior to the rat. The dosimetry is as described by Medhora et al [95]. Groups of rats were euthanized either at 60 or 90 days after radiation and kidneys were harvested then flash frozen in prechilled isopentane. In total four groups of rats were studied, rats receiving 0 Grey radiation harvested at day 60 (n=6) and day 90 after radiation (n=6), rats receiving 12.5 Grey radiation harvested at day 60 (n=7) and day 90 after radiation (n=7).

#### **3.2.2.2. Vascular quantification and segmentation**

For this study, we used the optical Cryo-imager to obtain the anatomical vessel structure of kidneys. The Vascular segmentation method is described in detail in our previous study [80]. Briefly, the stack of images acquired from the NADH channel of Cryo-imager goes through a set of image processing steps. First, the brightness and contrast of each slice are adjusted to enhance the quality of the image and to bold the vasculature elements. Second, the images are inverted because the blood in the vessels quench the NADH fluorescence and leaves the tissue itself bright but makes the inside the lumen of vessels darker (more like a negative image). Third, the background is subtracted so the other components of kidney tissue are removed from the kidney vessel tissue. Then by stacking the slices of each sample in Z-direction the re-constructed 3D-vasculature is obtained.

For quantification purposes, the 3D-vasculature is fed to Imaris (9.5.1 software, Bitplane Inc) and using a manual tracing algorithm based on local intensity contrast, the vessel network is extracted. The diameter of each vessel using both automatic and manual method is set. In the end, based on the extracted vessel network, Imaris calculates different parameters such as vessel mean diameter, vessel volume, the vessel branch depth, the number of terminal points etc. To measure the vessel density, the volume of each sample was measured by detecting the surface of the whole kidney in Imaris. Then the total vessel volume was divided by the whole sample volume to obtain vessel density.

### **3.2.2.3. Results**

The representative 3D extracted vasculature, the vessel terminal points (green spheres) and beginning points (blue spheres) from four groups of rats are shown in Figure 1. The size of spheres marking the beginning of the vessel and its terminal points varies based on the vessel diameter at that point. Figure 20a, b, c, and d represent the day-60 non-irradiated, day-60 irradiated, day-90 non-irradiated, and day 90-irradiated kidneys, respectively. Figure 20 shows that the green spheres in Figure 20b and d are both smaller and lower in number in comparison with Figure 20a and c, respectively. This indicates that either, small vessels are lost due to radiation or the vessels have become smaller and the number of vessels that could be detected 60 and 90 days after receiving 12.5 Grey radiation has decreased. With a closer look at the samples in Figure 20, it can be perceived that radiation has also lessened the diameter of the vessels. Also, the effect of radiation

is more evident in figure 1d in comparison with figure 1b meaning that the changes in vasculature due to radiation is more distinct 90 days post-radiation in comparison with 60 days post-radiation.

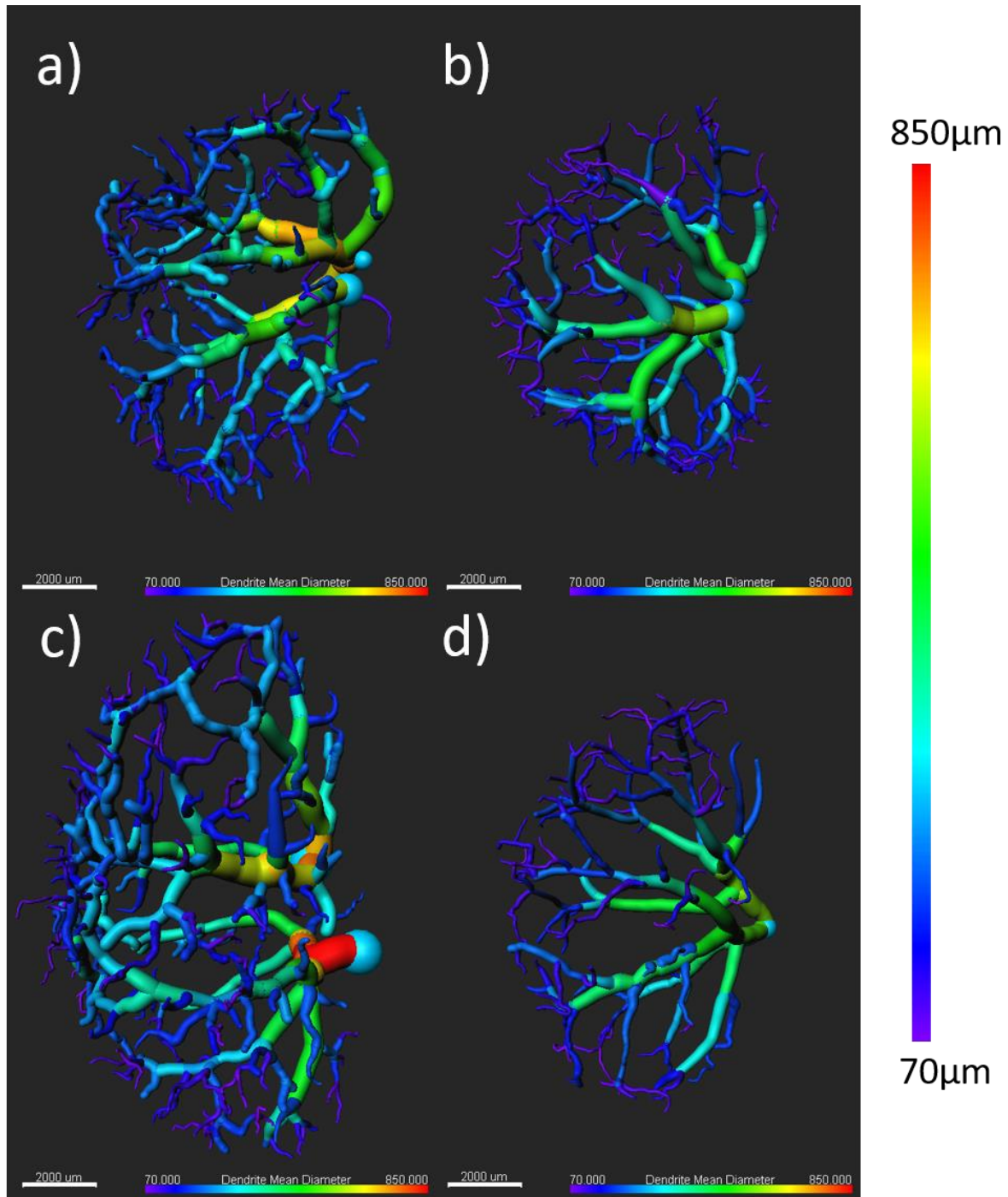
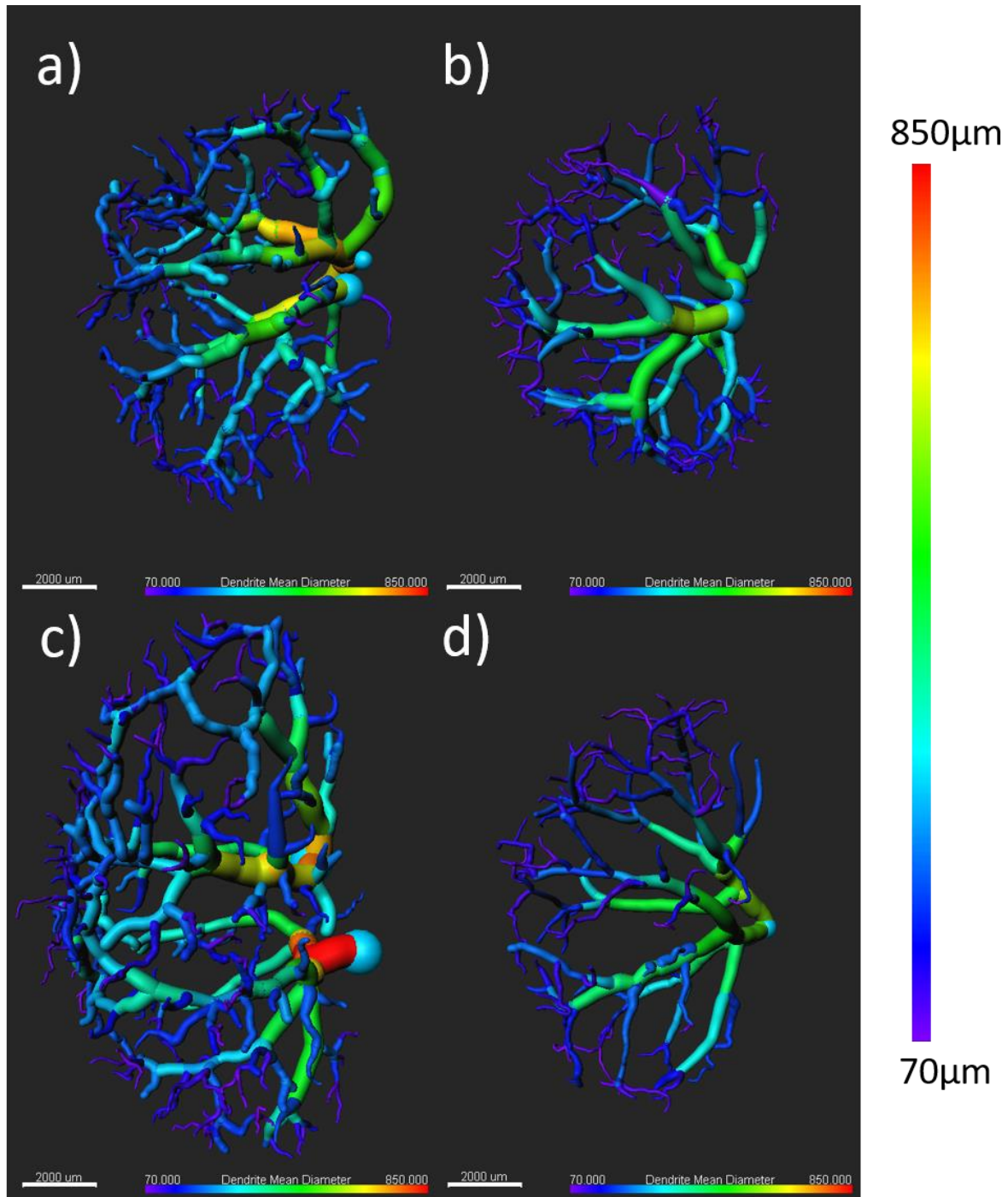


Figure 21 makes the observations in Figure 20 more tangible since it is color-coded based on the mean diameter of dendrites (vessels) ranging from 70  $\mu\text{m}$  to 850  $\mu\text{m}$ . The diameter of each vessel is measured from the center to the surface of the vessels. Violet is assigned to the vessels with a diameter close to 70  $\mu\text{m}$  and red is assigned to the vessel diameter close to 850  $\mu\text{m}$ . Representative

non-irradiated and irradiated kidneys harvested 60 days post-radiation are shown in



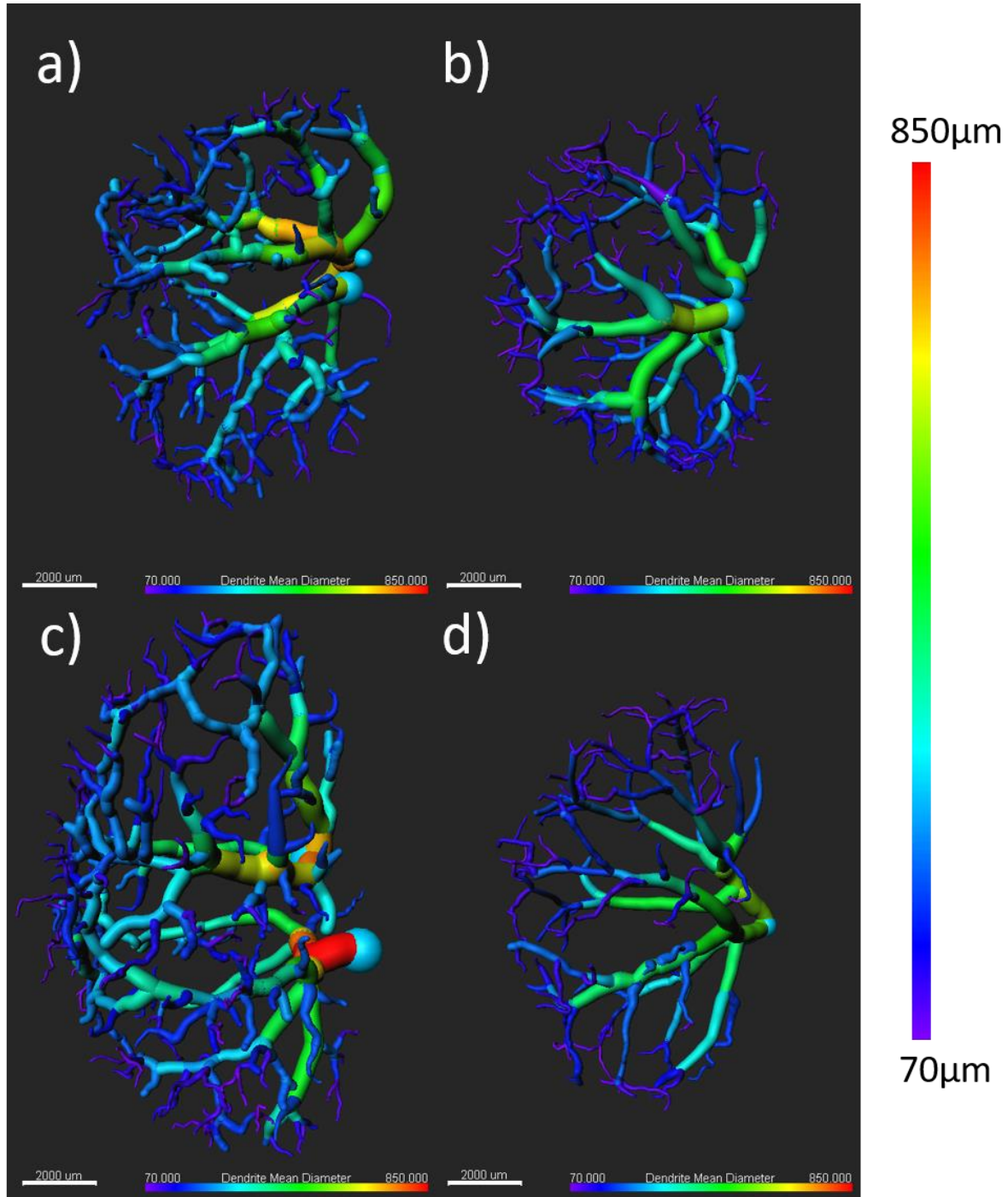


Figure 21c and d are representative kidneys for non-irradiated kidneys and irradiated kidneys harvest at day-90 post-radiation.

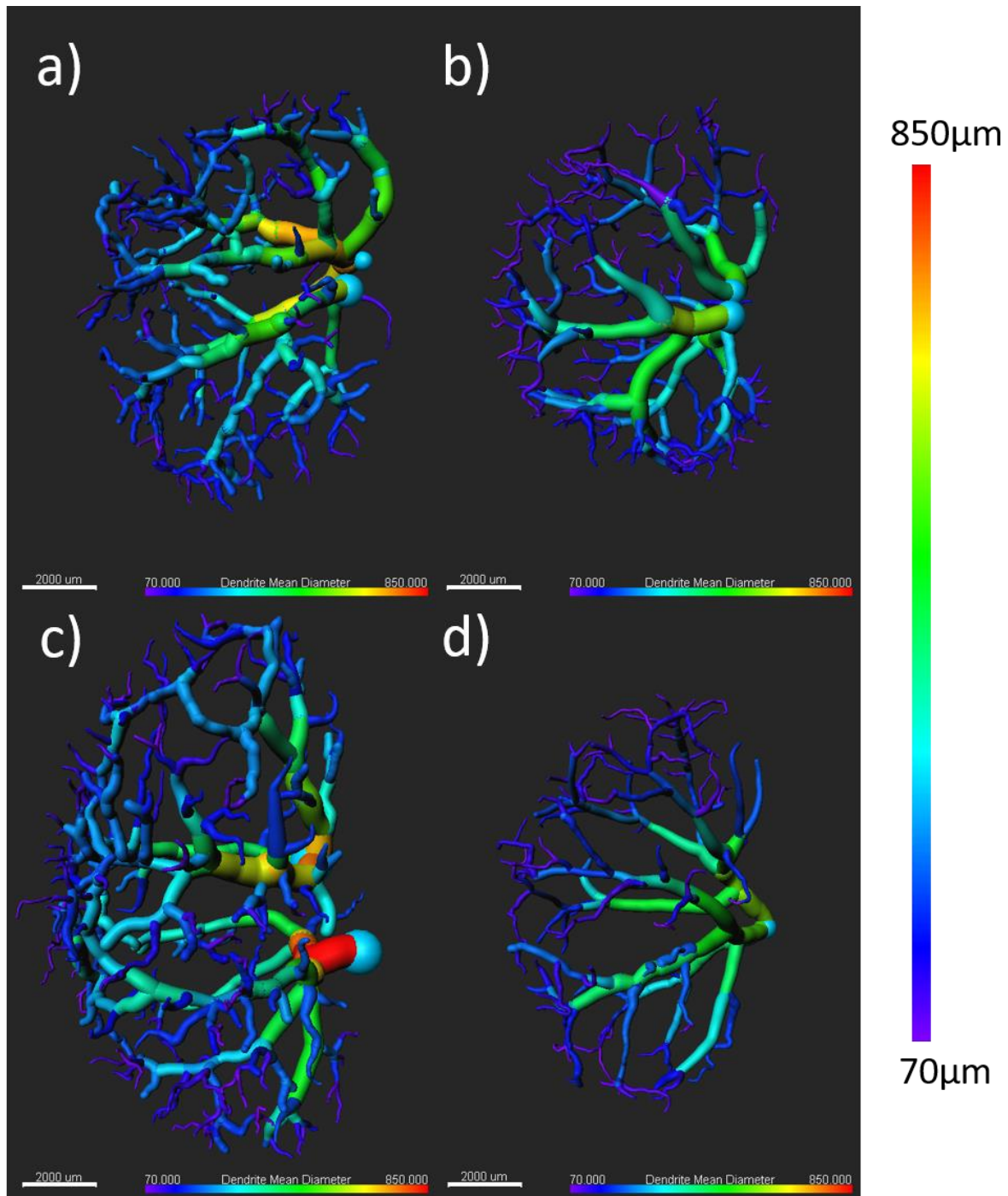


Figure 21a and c show that in non-irradiated kidneys, bigger vessel branches (the vessels that are closer to the beginning point) are mostly colored red or yellow. However,

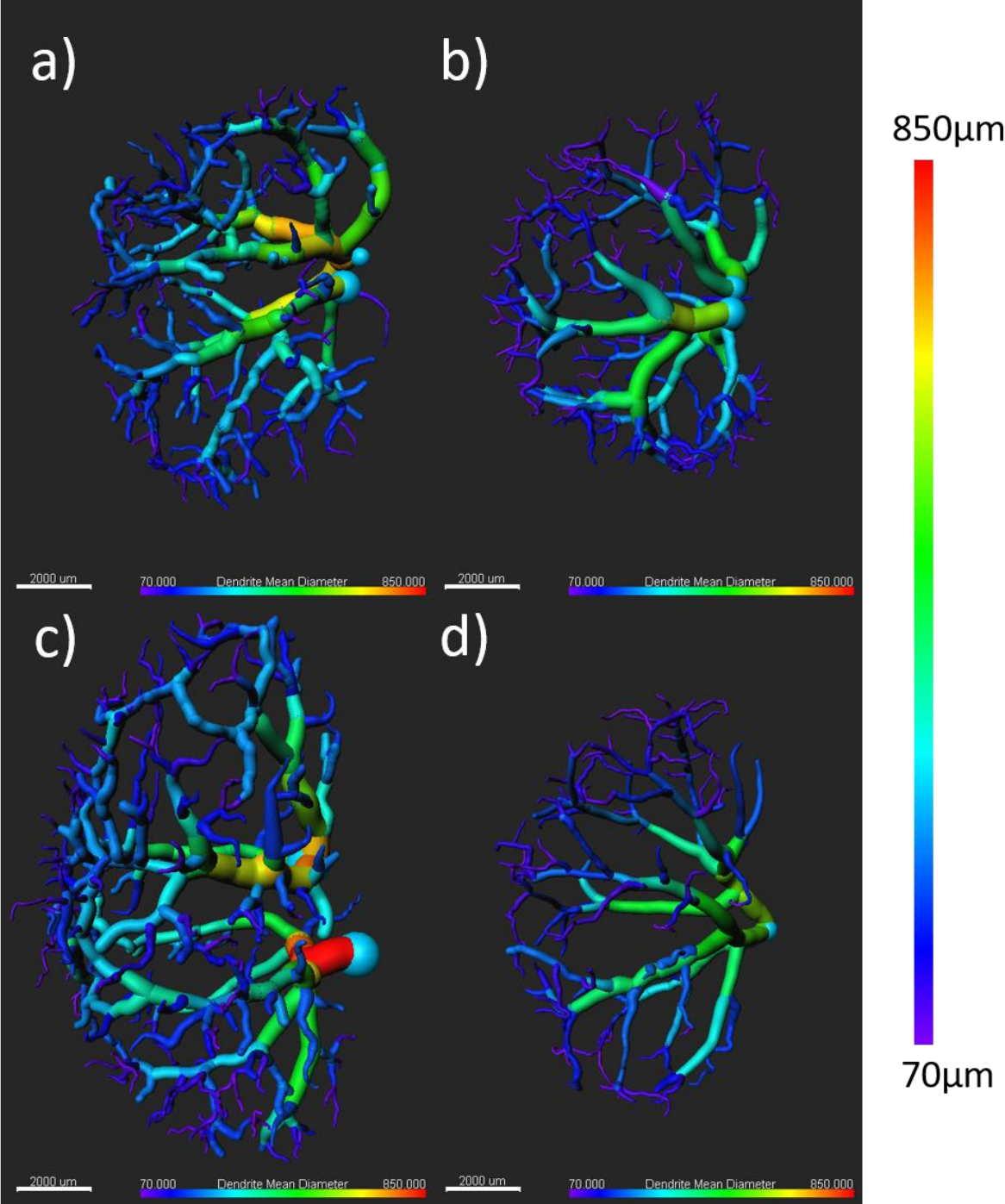


Figure 21b and d show that the bigger vessel branches are mostly colored green or blue. It denotes that radiation can damage the vessels, making the lumen of the blood vessels smaller. the

comparison of vessel colors in

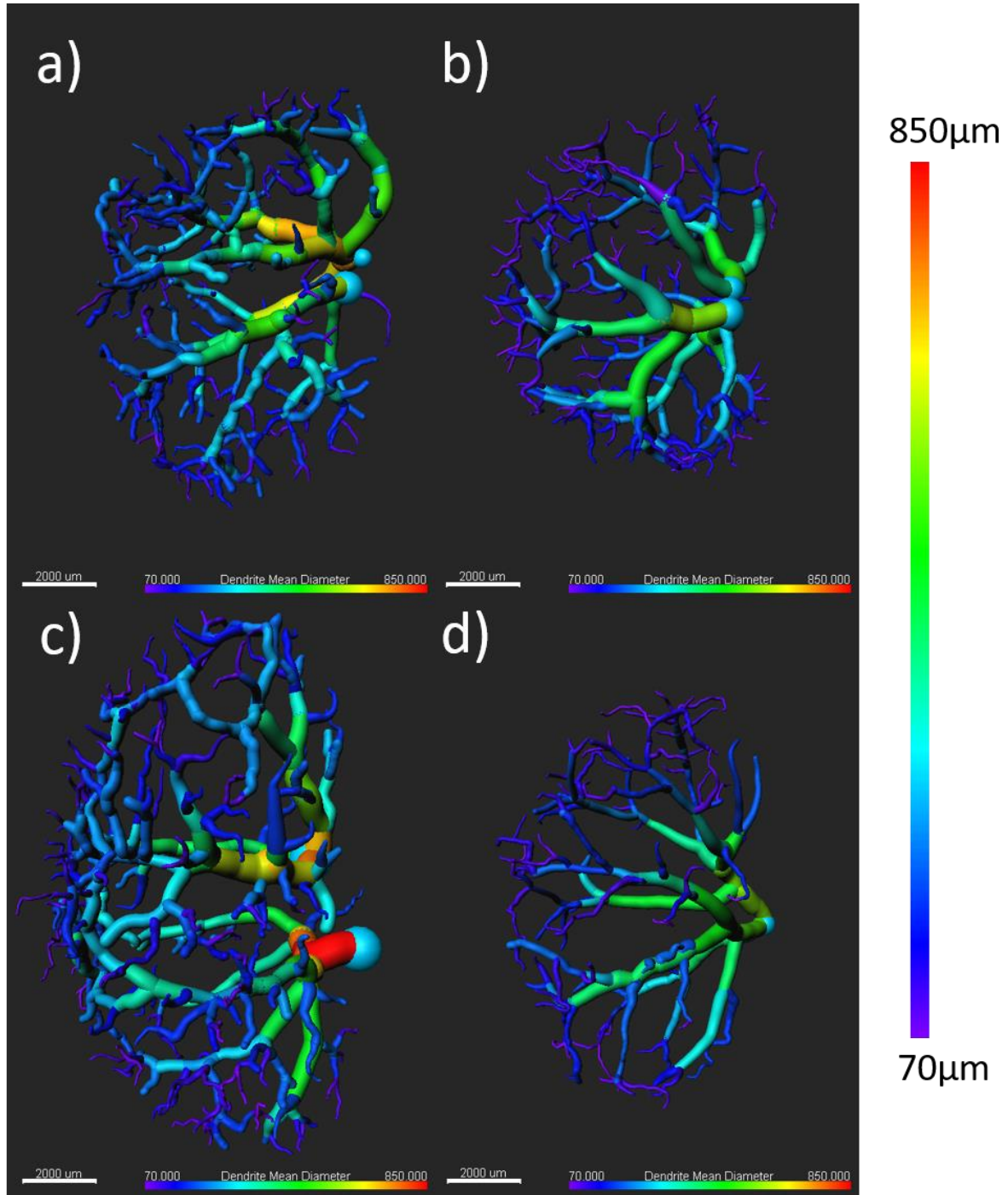


Figure 21a and b can infer that vessel mean diameter in non-irradiated and irradiated kidneys harvested 60 has not changed noticeably. However, the comparison of

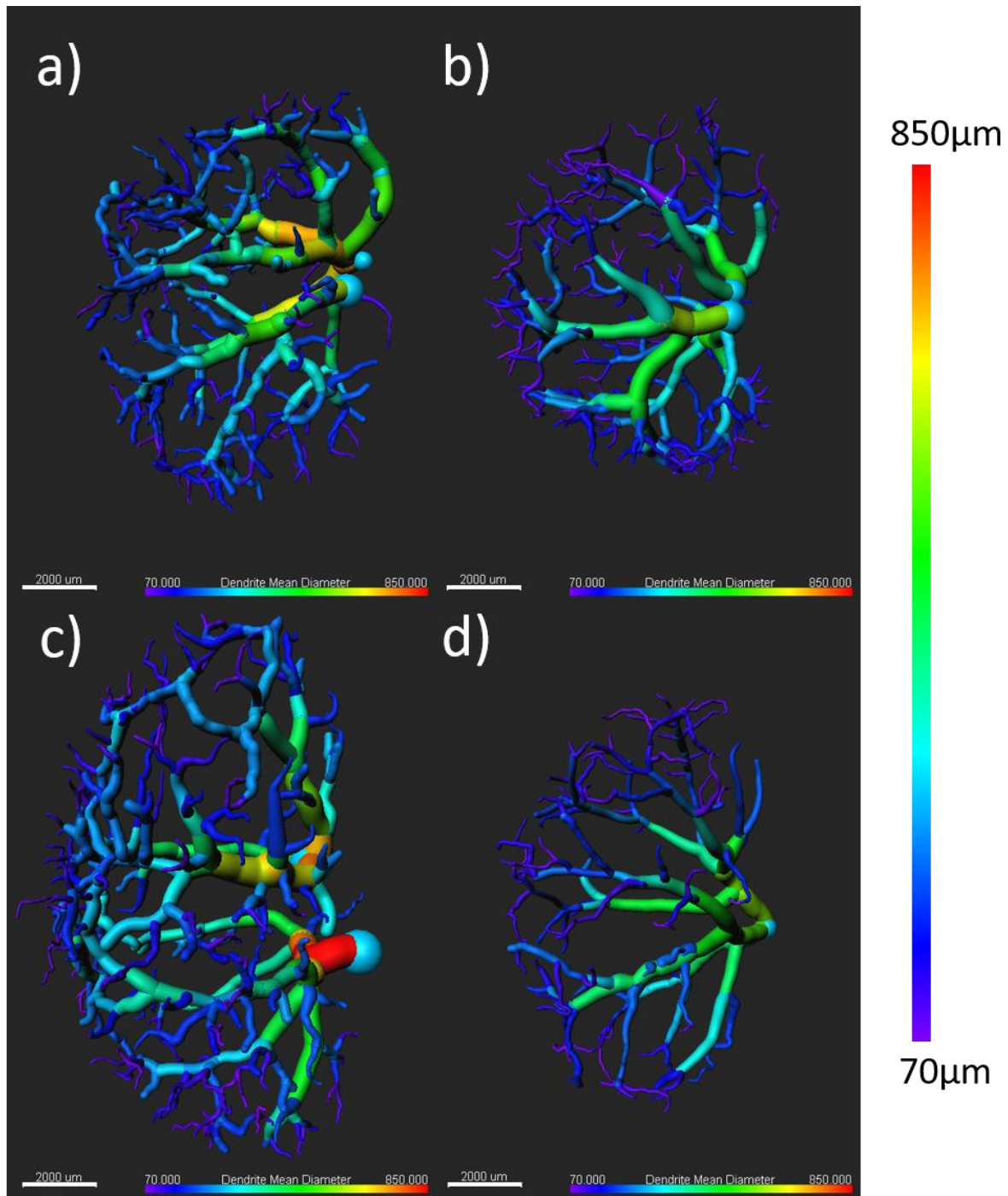


Figure 21c and d show that by 90 days post-radiation, vessel diameter in irradiated kidneys is remarkably different from that of non-irradiated kidneys.

Figure 22 shows the same kidneys in Figure 20 and

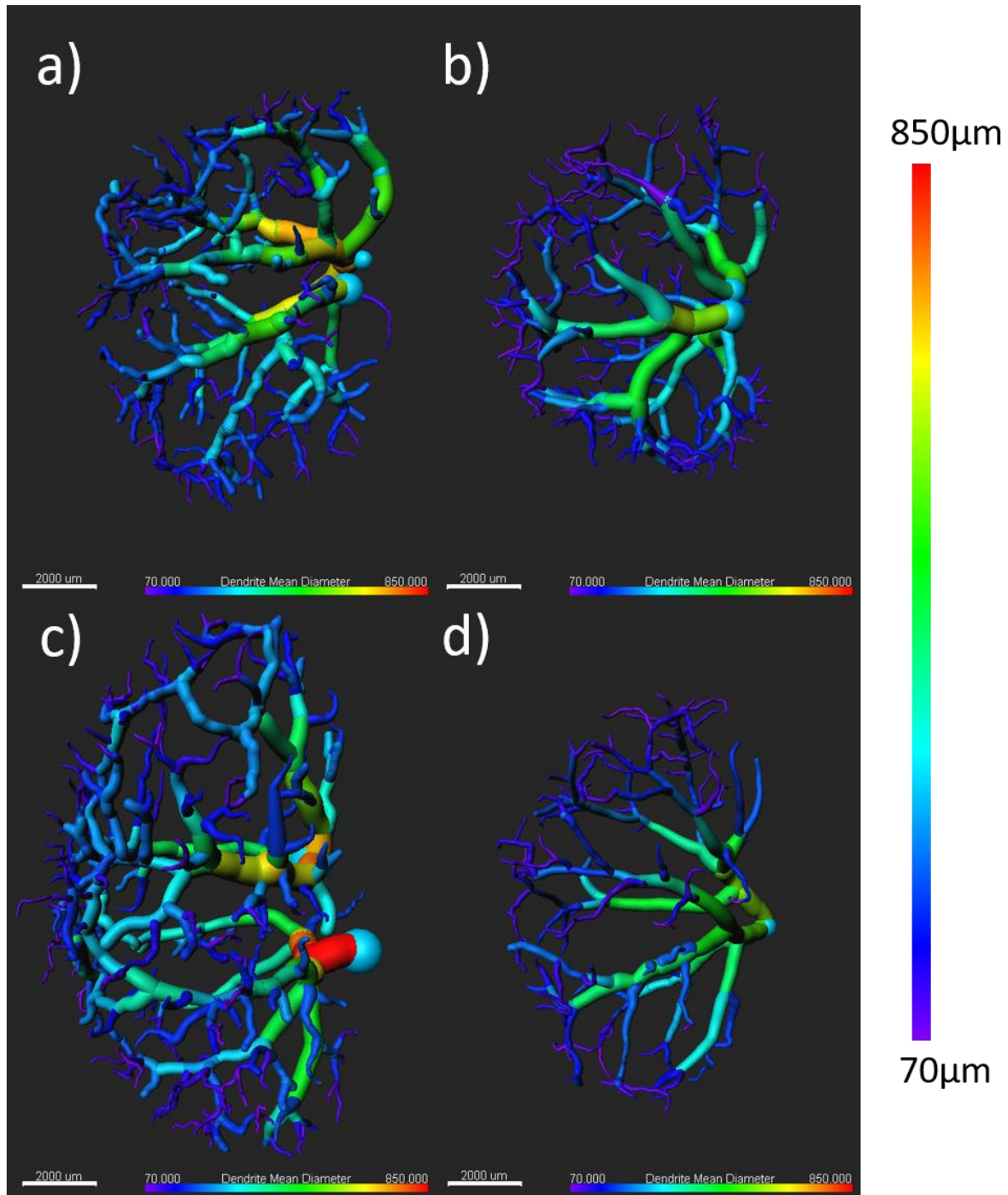
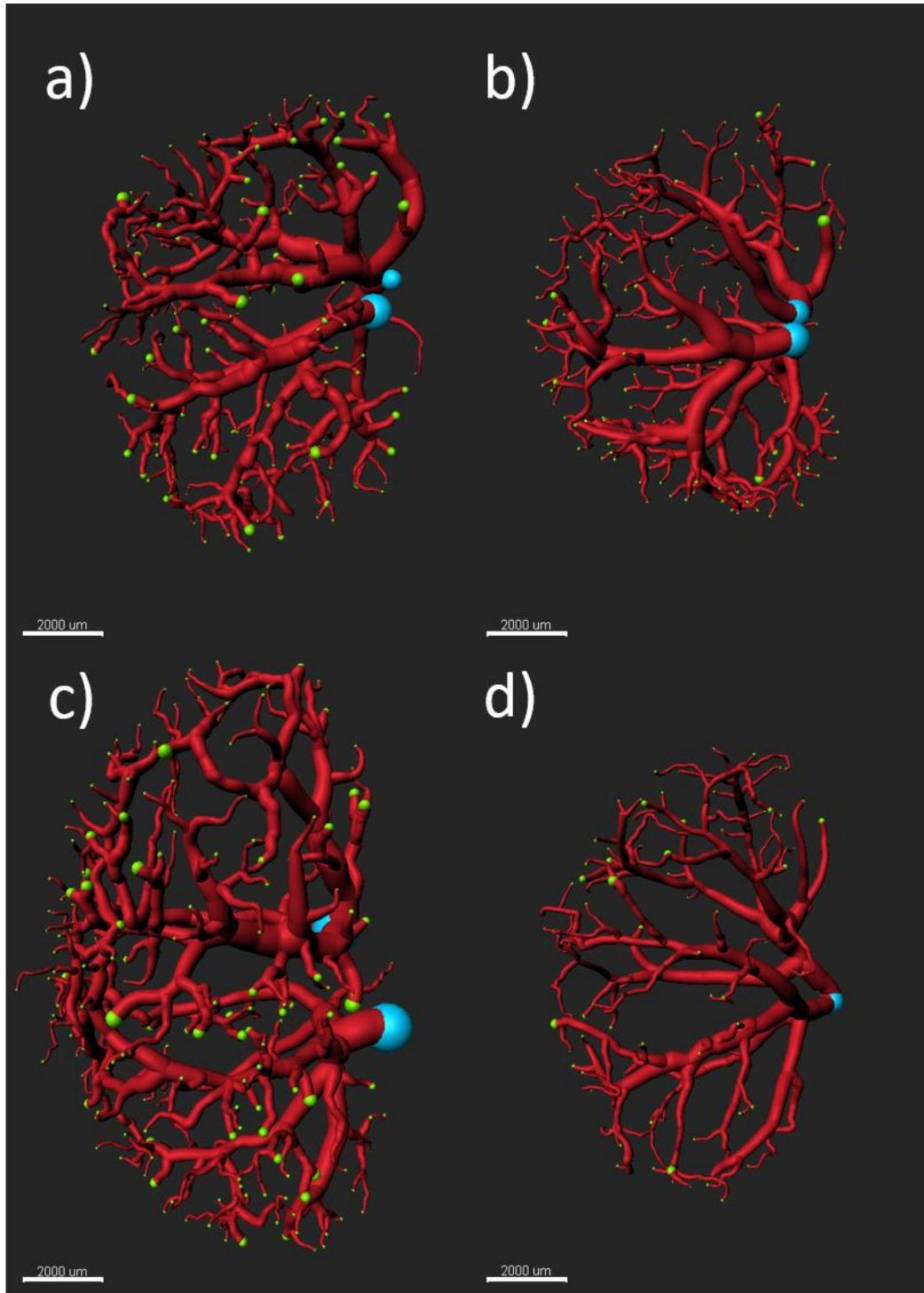
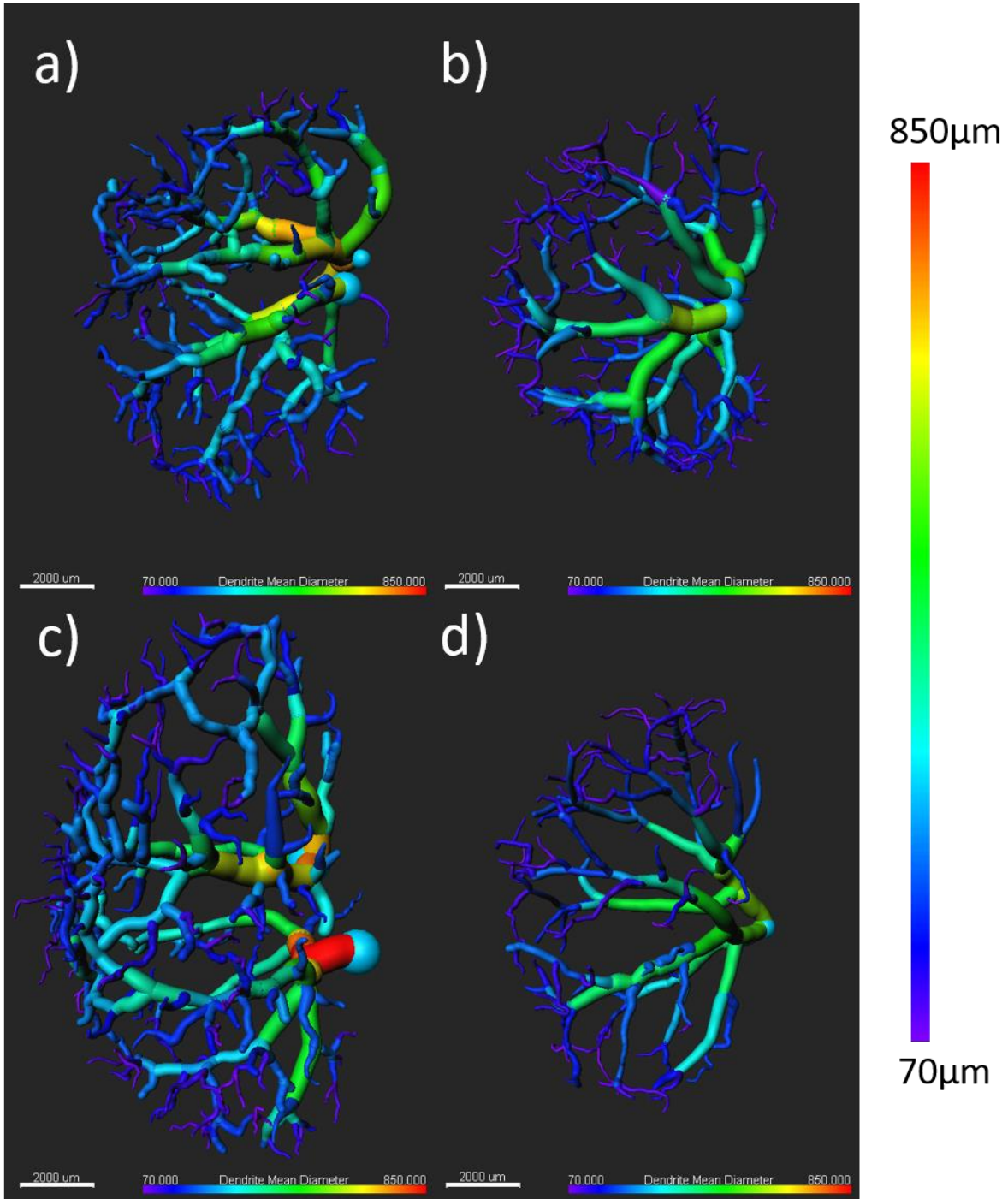


Figure 21 but color-coded based on the branch depth. Branch depth is the number of bifurcations in the shortest path, from the beginning point to a given point in the vessel network. The maximum branch depth is an indicator of the maximum number of times a vessel has been bifurcated to get to the smallest detected vessels. Maximum branch depth can be an indicator of the effect of radiation on small vessels. the decrease of maximum branch depth can be interpreted in two ways. One, small vessels are lost due to radiation or two, the small vessels have become smaller so that they were not detectable with resolution of 70  $\mu\text{m}$ . The highest maximum dendrite (vessel) branch depth that was observed in the samples was 19. Therefore, vessels are colored from the branch depth of 0, colored by violet, to the branch depth of 19, colored by red. Figure 22a and b are representative of the non-irradiated and irradiated kidneys harvested day-60 post-radiation. The smaller vessels (the vessels closer to the endpoints) in these figures are colored mainly blue and green. It suggests that first, the maximum branch depth for both groups of irradiated and non-irradiated kidneys harvested 60-days post-radiation is less than 19 and second, the branch depth has not been considerably affected by radiation 60 days after radiation. In contrast, in Figure 22c we can see that the color of smaller vessels is yellow and sometimes orange and red, but in Figure 22d they are green and blue. It means that radiation has affected the maximum of the vessel branch depth and this effect is conspicuous by day-90 post-radiation.





*Figure 20: The representative extracted 3D vasculatures* in which the terminal points of each vessels is marked with green spheres and the vessel beginning point is marked with blue sphere. a) Kidney received 0 grey irradiation and was harvested 60 days after irradiation. b) Kidney received 12.5 grey irradiation and was harvested 60 days after irradiation. c) Kidney received 0 grey irradiation and was harvested 90 days after irradiation. d) Kidney Received 12.5 irradiation and was harvested 90 days after irradiation.



*Figure 21:* The representative extracted 3D vasculatures colored-coded based on diameter. The vessel diameter ranges from 70 μm to 850 μm. The biggest vessels are colored red, and the smallest vessels are colored violet. a) Kidney received 0 grey irradiation and was harvested 60 days after irradiation. b) Kidney received 12.5 grey irradiation and was harvested 60 days after irradiation. c) Kidney received 0 grey irradiation and was harvested 90 days after irradiation. d) Kidney Received 12.5 irradiation and was harvested 90 days after irradiation.

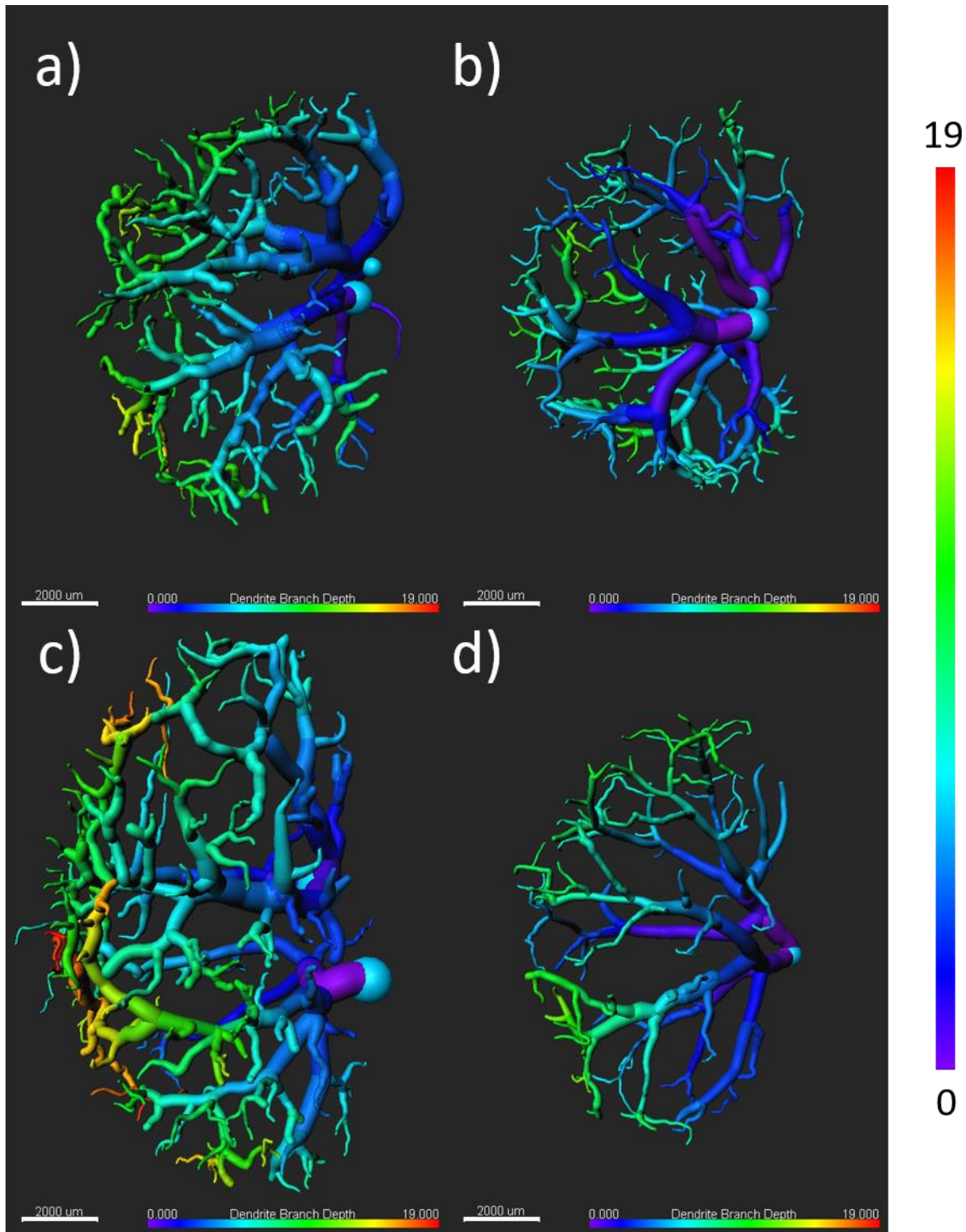


**Figure 22: The representative extracted 3D vasculatures colored-coded based on branch depth.** The branch depth ranges from 0 to 19. Vessels with branch depth of 0 are colored violet and vessels with branch depth 19 are colored red. a) Kidney received 0 grey irradiation and was harvested 60 days after irradiation. b) Kidney received 12.5 grey irradiation and was harvested 60 days after irradiation. c) Kidney received 0 grey irradiation and was harvested 90 days after irradiation. d) Kidney Received 12.5 irradiation and was harvested 90 days after irradiation.

To analyze the time-repose the fold change was used for the total vessel volume, vessel density, vessel branch depth and the number of terminal points, 60 and 90 days after radiation. The formula that was used for fold change is as follows:

$$\text{Day 90 fold change} = \frac{\text{Average of the measured parameter in day-90 post radiation irradiated kidneys}}{\text{Average of the measured parameter in in day-90 post-radiation non-irradiated kidneys}} \quad \text{Equation 5}$$

$$\text{Day 60 fold change} = \frac{\text{Average of the measured parameter in day-60 post radiation irradiated kidneys}}{\text{verage of the measured parameter in in day-60 post-radiation non-irradiated kidneys}} \quad \text{Equation 6}$$

The value of fold change for 3D vessel structural parameters was calculated to investigate the time response of irradiated kidneys. The fold change provides a quantitative index for the severity of changes caused by radiation at day-60 and day-90. The smaller is the value of fold change, the more severe are the damages that were caused by radiation. Table 2 presents the value of fold change for total vessel volume, vessel density, maximum branch death, and the number of terminal points at day-90 and day-60 post-radiation. The result in Table 2 illustrates that the value of fold change for all parameters is notably smaller at da-90 compared to day-60. It means that the effect of radiation on total vessel volume, vessel density, maximum vessel branch depth and the number of vessel terminal points are more pronounced at day-90 post-radiation compared to day-60.

Table 2: The fold changes for day-90 and day-60 post radiation.

	<b>Harvesting Day</b>	<b>Total Vessel Volume</b>	<b>Vessel Density</b>	<b>Maximum Vessel Branch Depth</b>	<b># Vessel Terminal Points</b>
<b>Fold</b>	60	0.7376	0.8861	0.9004	0.9178
<b>Change</b>	90	0.4490	0.4337	0.72	0.4818

Table 3 contains the average value  $\pm$  standard deviation of the measurement that were done on all the 3D vessel structural parameters. As Table 3 shows, for 0 grey radiation, total vessel volume,

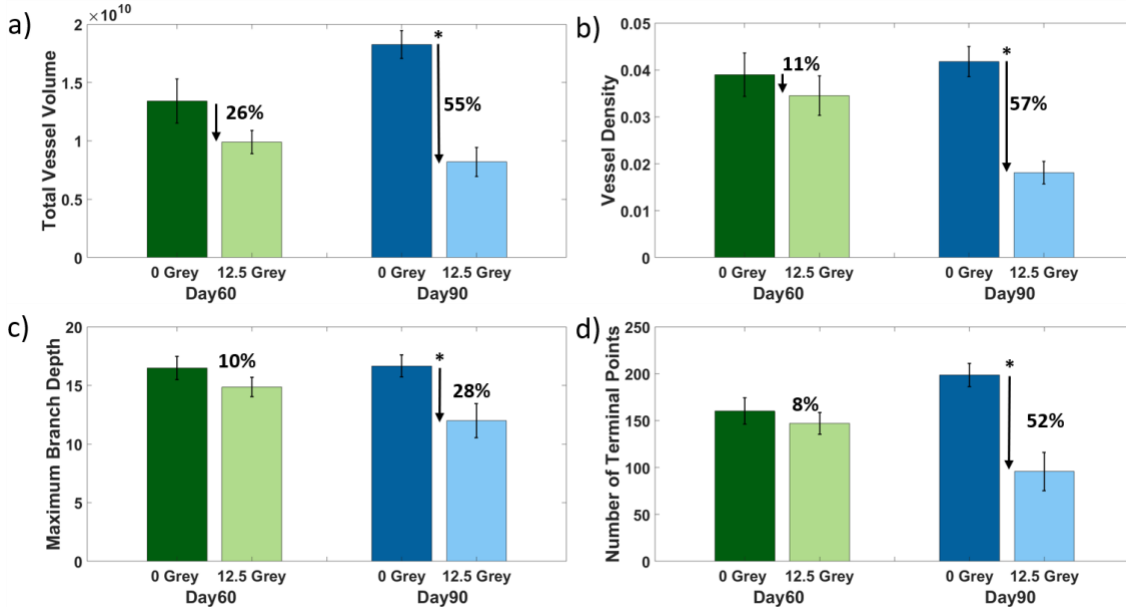
vessel density, maximum vessel branch depth, and the number of terminal points has increased at day-90 compared to day-60. These results were expected since by the time of harvesting the kidneys, the rats had not reached their complete physical growth. For 12.5 grey radiation, Table 3 shows that for 12.5 Grey irradiated kidneys, the changes in the average of total vessel volume, vessel density, maximum vessel branch depth and the number of terminal points by day 90 are more intense compared to those of day 60. This observation manifests the time-response of radiation on kidney vessels.

*Table 3:* The average of measured vessel parameters and their standard deviation.

<b>Radiation Dosage</b>	<b>Harvesting Day</b>	<b>Total Vessel Volume× 10<sup>9</sup>μm<sup>3</sup></b>	<b>Vessel Density</b>	<b>Maximum Vessel Branch Depth</b>	<b># Vessel Terminal Points</b>
<b>0 Grey</b>	60	13.421±4.6184	3.9%±1.14%	16.5±2.43	160.17±34.55
	90	18.269±2.9164	4.18%±0.79%	16.67±2.34	198.67±30.04
<b>12.5 Grey</b>	60	9.8997±2.5969	3.45%±1.11%	14.86±2.19	147±30.28
	90	8.2020±3.2778	1.81%±0.63%	12±3.87	95.71±53.68

Two-factor repeated ANOVAs was applied on all the data for dose-response at day 60 and day 90.

For a better understanding of the dose-response, the data in Table 3 are exhibited in



Figure

23.

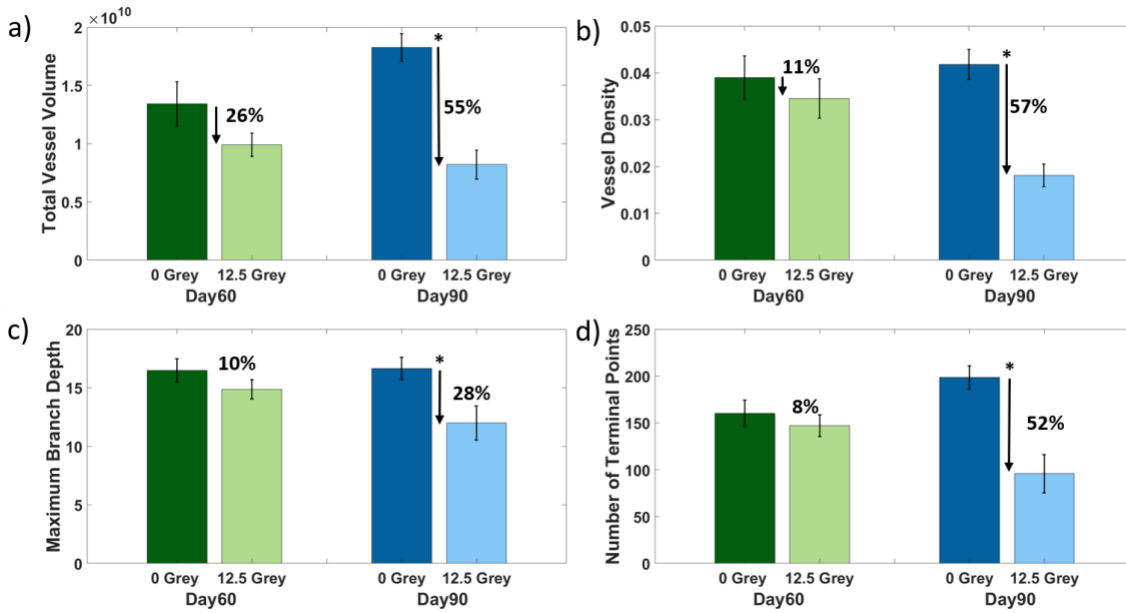


Figure 23 displays the bar graph and the statistical results for total vessel volume, vessel density, maximum branch depth and number of terminal points in all samples of our four groups.

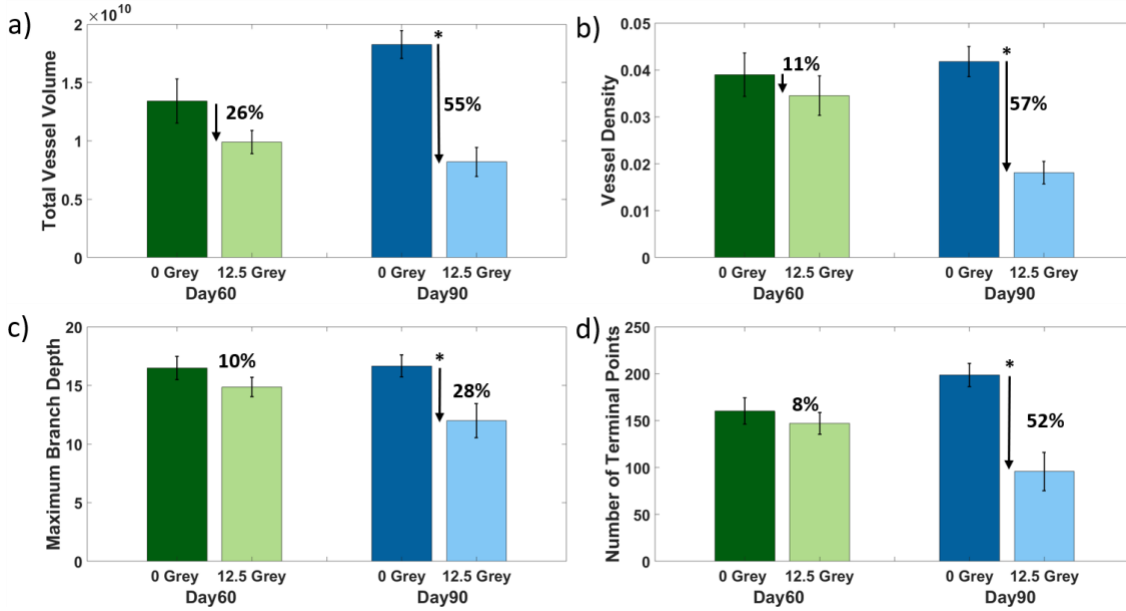


Figure 23a shows the changes in total vessel volumes. Since by using VMI method, we are only able to detect the vessels that carry blood, the total vessel volume is also an indicator of total blood volume.

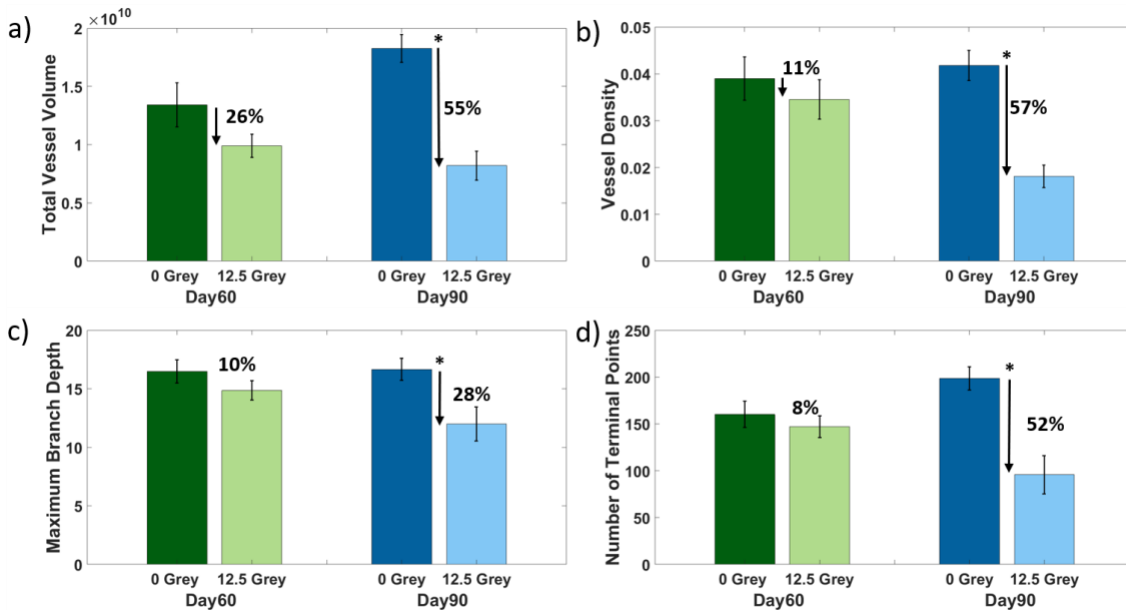


Figure 23a reveals that 12.5 Grey radiation at day 60 post-radiation reduced the total blood volume by 26% and 55% at day 90 after radiation.

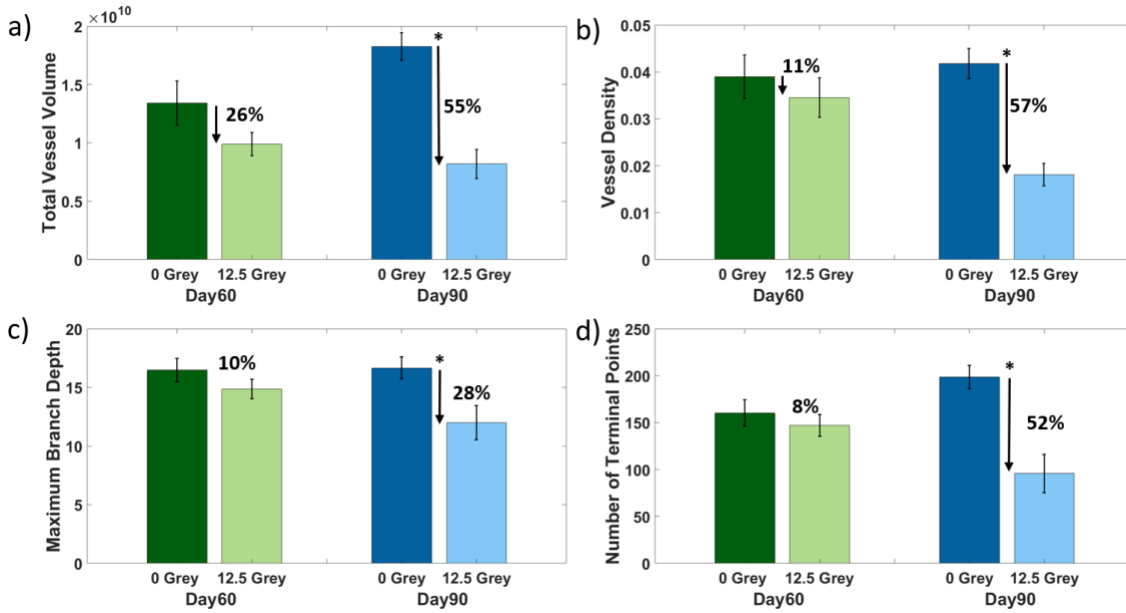


Figure 23b illustrates that vessel density has drop by 11% and 57% after 60- and 90-days post-radiation, respectively.

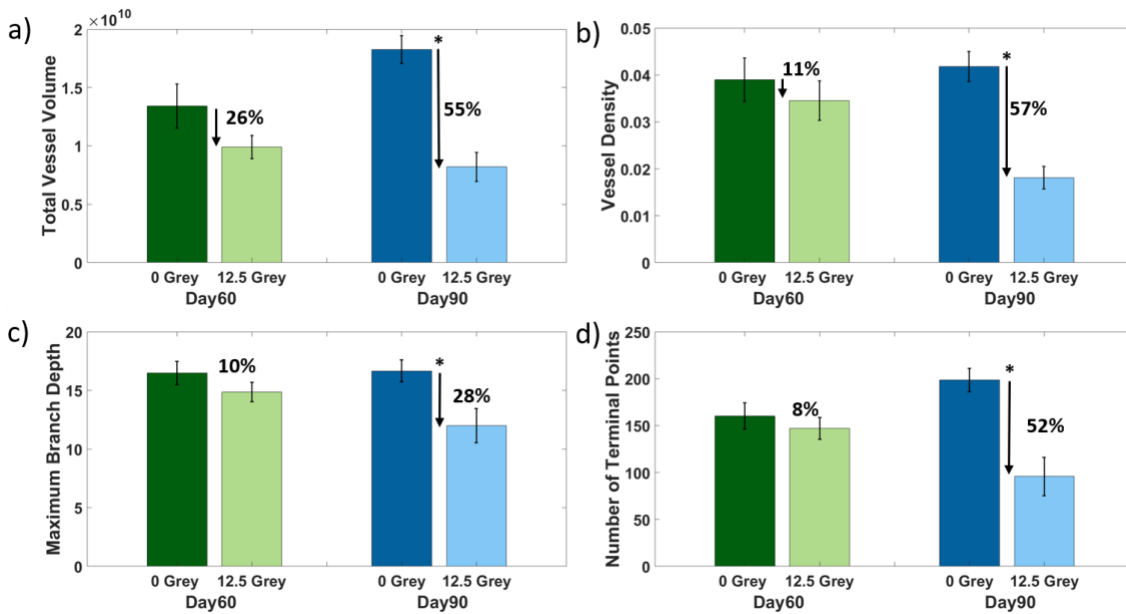


Figure 23c displays that the maximum branch depth for 12.5 Grey has decreased by 10% compared to 0 gray at day 60, however, this decrease is 28% on day 90 post-radiation. The number of terminal points is a good estimation for the number of vessels that could be detected in a sample. The bar graphs

in

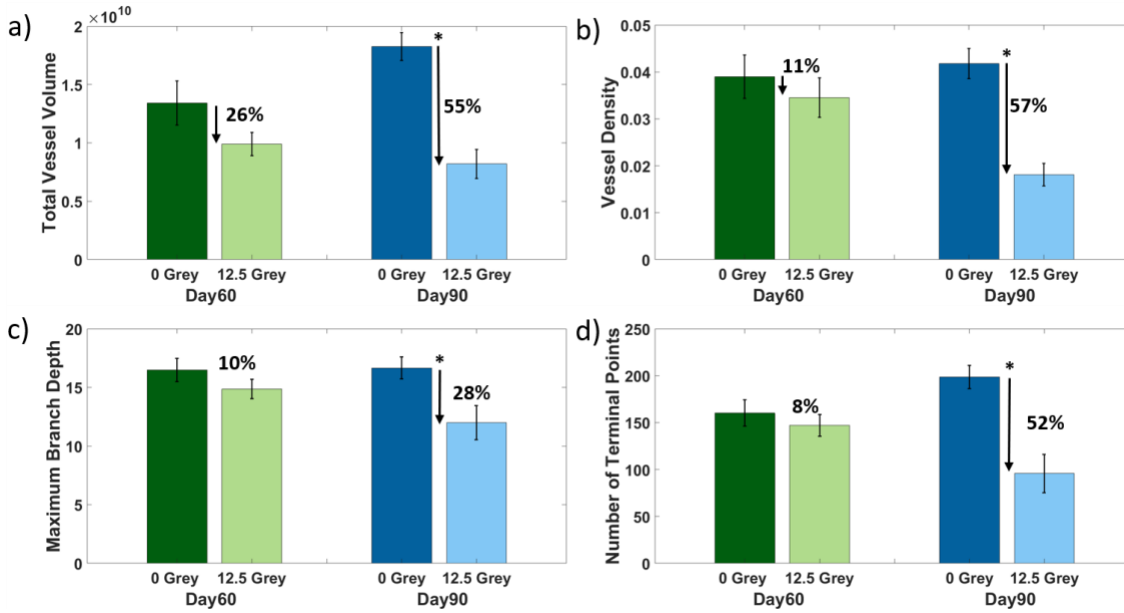
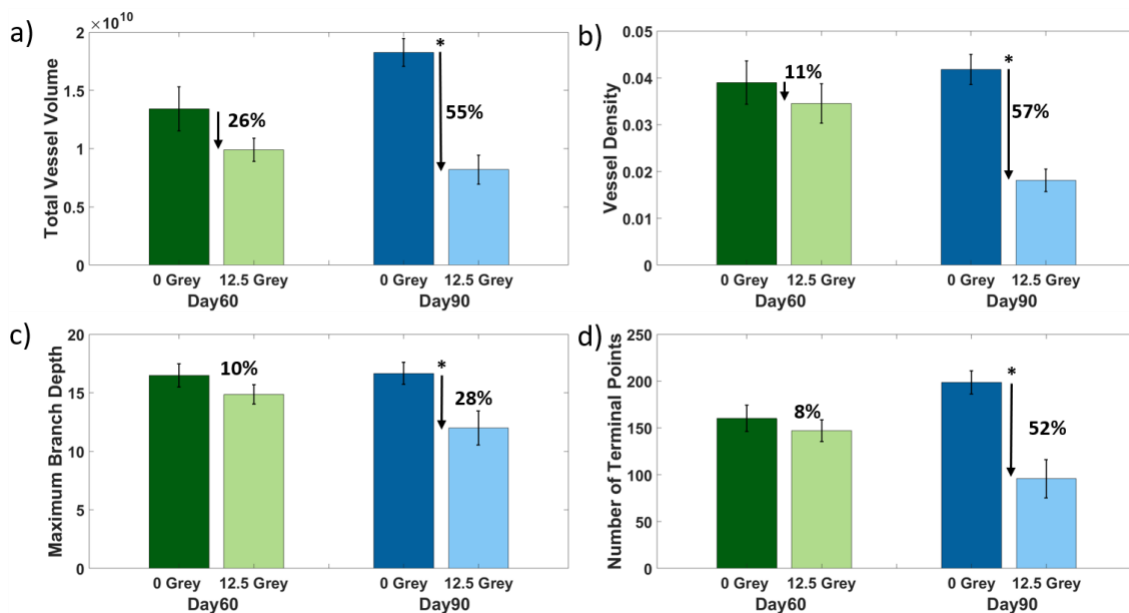


Figure 23d shows the statistics for the number of vessels in all samples, and it reveals that receiving 12.5 grey radiation diminishes the number of terminal points on day 60 only by 8%. Despite this little change on day 60, the number of terminal points is noticeably lower for 12.5 compared to those of 0 Grey on day 90. The results of repeated ANOVAs on these parameters show that total vessel volume, vessel density, maximum branch depth and the number of terminal points is

significantly lower in the irradiated group at day-90 (with a criterion of  $P < 0.05$ ). This confirms that the changes caused by 12.5 grey radiation are more evident 90 days after radiation compared to 60 days post-radiation.

The kidney is a richly perfused organ that renal blood flow (RBF) accounts for almost 25% of the cardiac output [96]. Therefore, being able to measure the blood volume in vessel would provide us with useful information about kidney perfusion. Using VMI method, vessel diameter would be a good indicator of blood perfusion in kidney. Although our result shows that the vessel mean diameter after radiation is decreased, the number of detected vessels had shrunk too (the decrease in the number of endpoints). Consequently, the average vessel diameter in each sample did not



**Figure 23: The average of measurements on all the kidneys in bar plots  $\pm$  standard deviation.** (a) Total vessel volume diameter  $\pm$  standard deviation for 12.5 Grey (irradiated group) and 0 Grey (non-irradiated group) 60 and 90 days after radiation. The total vessel volume r has dropped 26% 60 days after radiation and 55% 90 days after radiation. (b) The average of vessel density  $\pm$  standard deviation for irradiated group and control group 60 and 90 days after radiation. The total vessels volume decreased by 26% at day-60 post-radiation and 55% at day-90 post-radiation. (c) The average of Maximum branch  $\pm$  depth standard deviation for irradiated group and control group 60 and 90 days after radiation. The Maximum branch depth is reduced by 10% and 28% for 60 and 90 days after radiations, respectively. (d) The average of the number of terminal points  $\pm$  depth standard deviation for the irradiated group and control group 60 and 90 days after radiation. The number of terminal points diminished by 8% and 52% for day-60 and 90 post-radiation, respectively. \*, a significant difference of the vessel density, the maximum branch depth and between the number of terminal points between the irradiated group and non-irradiated at day-90 post-radiation with the criteria of  $P < 0.05$ .

change significantly and the effect of radiation on vessel diameter was not conveyed by measuring the average of vessel mean diameter. Hence, to illustrate the effect of radiation on the vessel mean diameter, we counted the number of vessels in different diameter ranges. Table 4 shows the number of vessels in different ranges, with a span of 100  $\mu\text{m}$ . This data shows that the number of vessels in all ranges on day-90 post-radiation has decreased. With a closer look at day-60 data, we realize that the number of vessels in smaller ranges (70-150  $\mu\text{m}$ , 250-450  $\mu\text{m}$ ), has increased and the number of vessels in larger ranges (450-850  $\mu\text{m}$ ) has decreased in the irradiated group. This might suggest that although by day-60 radiation narrows the larger vessel vasculogenesis or angiogenesis would be continued. Two-factor repeated ANOVAs was applied on all the data in table 3 for dose-response at day-60 and day-90. With the criteria of  $P < 0.005$ , the number of vessels in irradiated kidneys on day-90 was significantly lower in ranges of 150-250  $\mu\text{m}$ , 250-350  $\mu\text{m}$ , 350-450  $\mu\text{m}$  and 750-850  $\mu\text{m}$ . No significant decrease at day-60 vessel diameter was observed. Table 4 also confirms our observation that by day-90, radiation more severely damages the kidneys in comparison with day-60.

*Table 4:* The number of vessels that was detected for different ranges of 100  $\mu\text{m}$  span and stars (\*) mark the values in the FR-irradiated group that are significantly different from mom-irradiated group with the criteria of  $P < 0.05$ .

Harvesting Day	Radiation dosage	70-150 $\mu\text{m}$	150-250 $\mu\text{m}$	250-350 $\mu\text{m}$	350-450 $\mu\text{m}$	450-550 $\mu\text{m}$	550-650 $\mu\text{m}$	650-750 $\mu\text{m}$	750-850 $\mu\text{m}$
<b>60</b>	0 Grey	131.1667	111.1667	49	22.1667	9	4.3333	1.5	0.5
	12.5 Grey	136.7143	105.5714	67.1429	25.7143	7.5714	0.5714	0.1429	0.2875
<b>90</b>	0 Grey	151.1667	125.8333	85.8333	30.5	11.1667	3.6667	1.6667	2.1667
	12.5 Grey	86.4286	25.8571*	25.8571*	12.1429*	6.8571	1	0	0*

# **Chapter 4**

## **Conclusion and Future Direction**

## 4. Conclusion and future direction

The *in vivo* fluorescence imager uses redox ratio as a biomarker of the metabolic state of a tissue. I designed and implemented the second version of the *in vivo* fluorescence with main changes including removing the excitation filter wheel and replacing the Nikon light source with Xcite LED1. This alteration reduced operation cost, phototoxicity, experiment time, weight, and size of the instrument. I also developed user interfaces for both versions that reduced the experience time by 80%. The result of our study on wounds of diabetic mice showed that *in vivo* fluorescence imager successfully monitored the effect of 670 Far-red photobiomodulation on diabetic wounds. It indicates that our non-invasive, non-contact and portable *in vivo* fluorescence imager can distinguish the impaired diabetic wound and detect the efficiency of interventions for wound healing by tracking the mitochondria dysfunction and ROS concentrations during wound healing. Additionally, to make this instrument more convenient for clinical trials, I changed the assembly by separating the optical part from the hardware part. As a result, the *in vivo* fluorescence imager became more manageable for the user. Furthermore, it provided more degrees of freedom to move the optical part, so different parts of a patient body became more accessible. Consequently, it minimized the change of position that would have been needed from the patient.

The characteristics of the second version of the *in vivo* fluorescence imager made it suitable for the clinical setting. A future human pilot study can confirm that it can be highly beneficial to be used in wound care centers for monitoring the efficiency of interventions on diabetic wound healing. Moreover, there are many other fluorophores in the skin that are marker of multiple injuries and interventions. The *in vivo* fluorescence imager can easily track these markers when choosing the appropriate excitation wavelength and emission filters. For example, by imaging

other fluorophores like porphyrin and collagens, the human acnes [97] and microvascular diseases in type1 diabetes [98] can be studied.

We use the 3D cryo-imaging system to study the metabolic state of tissue by tracking NADH and FAD. Besides, by utilizing the 3D cryo-imaging system a vessel segmentation method was developed in our lab to extract the 3D vessel network of the different organ. I validated the vessel segmentation method by Murray's law and used it to quantitatively investigate the dose-response and time-response of ionizing radiation in the vessel structure of a rat's kidney. The results showed that this method successfully segmented the perfused vessels in kidneys and manifest the vessel structure anatomical damage caused by radiation.

This method is also applicable for extracting the 3D vessel network in other organs like lungs, liver, heart and cancerous tumors. Therefore, it can be used to investigate various disease-induced anatomical injuries to vessel structure. Moreover, by improving the 3D cryo imaging resolution to microscopic level, the effect of disease on capillary vessels and consequence cellular changes can be monitored too.

## References

- [1] G. Keiser, "Light-Tissue Interactions," in *Biophotonics*: Springer, 2016, pp. 147-196.
- [2] H. Lodish *et al.*, *Molecular cell biology*. Macmillan, 2008.
- [3] K. Roberts, B. Alberts, A. Johnson, P. Walter, and T. Hunt, "Molecular biology of the cell," *New York: Garland Science*, 2002.
- [4] D. Voet, J. G. Voet, and C. W. Pratt, *Fundamentals of biochemistry*. 2000.
- [5] A. Kumari, *Sweet Biochemistry: Remembering Structures, Cycles, and Pathways by Mnemonics*. Academic Press, 2017.
- [6] M. A. Wall *et al.*, "Metabolic Imaging Approaches: Optical Imaging," in *Imaging and Metabolism*: Springer, 2018, pp. 99-126.
- [7] B. Dictionary. "Electron Transport Chain." <https://biologydictionary.net/electron-transport-chain/> (accessed).
- [8] L. Learning. "Module6: Metabolic Pathways, Electron Transport Chain." <https://courses.lumenlearning.com/wm-biology1/chapter/reading-electron-transport-chain/> (accessed).
- [9] A. Mayevsky and B. Chance, "Repetitive patterns of metabolic changes during cortical spreading depression of the awake rat," *Brain research*, vol. 65, no. 3, pp. 529-533, 1974.
- [10] S. Ji, B. Chance, B. H. Stuart, and R. Nathan, "Two-dimensional analysis of the redox state of the rat cerebral cortex in vivo by NADH fluorescence photography," *Brain research*, vol. 119, no. 2, pp. 357-373, 1977.
- [11] A. Mayevsky and B. Chance, "Intracellular oxidation-reduction state measured in situ by a multichannel fiber-optic surface fluorometer," *Science*, vol. 217, no. 4559, pp. 537-540, 1982.
- [12] B. Chance, A. Mayevsky, C. Goodwin, and L. Mela, "Factors in oxygen delivery to tissue," *Microvascular research*, vol. 8, no. 3, pp. 276-282, 1974.
- [13] B. Chance, "Optical method," *Annual review of biophysics and biophysical chemistry*, vol. 20, no. 1, pp. 1-30, 1991.
- [14] M. C. Skala *et al.*, "In vivo multiphoton fluorescence lifetime imaging of protein-bound and free nicotinamide adenine dinucleotide in normal and precancerous epithelia," *Journal of biomedical optics*, vol. 12, no. 2, p. 024014, 2007.
- [15] N. Ramanujam, R. Richards-Kortum, S. Thomsen, A. Mahadevan-Jansen, M. Follen, and B. Chance, "Low temperature fluorescence imaging of freeze-trapped human cervical tissues," *Optics Express*, vol. 8, no. 6, pp. 335-343, 2001.
- [16] MEDBULLETS. "Electron Transport Chain." <https://step1.medbullets.com/biochemistry/102051/electron-transport-chain> (accessed).
- [17] H. Bayr, "Reactive oxygen species," *Critical care medicine*, vol. 33, no. 12, pp. S498-S501, 2005.
- [18] X. Wen, J. Wu, F. Wang, B. Liu, C. Huang, and Y. Wei, "Deconvoluting the role of reactive oxygen species and autophagy in human diseases," *Free Radical Biology and Medicine*, vol. 65, pp. 402-410, 2013.
- [19] H. Cui, Y. Kong, and H. Zhang, "Oxidative stress, mitochondrial dysfunction, and aging," *Journal of signal transduction*, vol. 2012, 2012.

- [20] J. Finaud, G. Lac, and E. Filaire, "Oxidative stress," *Sports medicine*, vol. 36, no. 4, pp. 327-358, 2006.
- [21] G. Storz and J. A. Imlay, "Oxidative stress," *Current opinion in microbiology*, vol. 2, no. 2, pp. 188-194, 1999.
- [22] B. Halliwell and J. M. Gutteridge, *Free radicals in biology and medicine*. Oxford University Press, USA, 2015.
- [23] M. P. Murphy, "How mitochondria produce reactive oxygen species," *Biochemical journal*, vol. 417, no. 1, pp. 1-13, 2009.
- [24] O. I. Aruoma, "Free radicals, oxidative stress, and antioxidants in human health and disease," *Journal of the American oil chemists' society*, vol. 75, no. 2, pp. 199-212, 1998.
- [25] V. J. Thannickal and B. L. Fanburg, "Reactive oxygen species in cell signaling," *American Journal of Physiology-Lung Cellular and Molecular Physiology*, vol. 279, no. 6, pp. L1005-L1028, 2000.
- [26] V. V. Tuchin, "Light-tissue interactions," ed: CRC Press: Boca Raton, 2003, pp. 3.1-3.26.
- [27] G. D. Luker and K. E. Luker, "Optical imaging: current applications and future directions," *Journal of Nuclear Medicine*, vol. 49, no. 1, pp. 1-4, 2008.
- [28] C. Balas, "Review of biomedical optical imaging—a powerful, non-invasive, non-ionizing technology for improving in vivo diagnosis," *Measurement science and technology*, vol. 20, no. 10, p. 104020, 2009.
- [29] R. N. Pittman, "Regulation of tissue oxygenation," in *Colloquium series on integrated systems physiology: from molecule to function*, 2011, vol. 3, no. 3: Morgan & Claypool Life Sciences, pp. 1-100.
- [30] M. D. Brand and D. G. Nicholls, "Assessing mitochondrial dysfunction in cells," *Biochemical Journal*, vol. 435, no. 2, pp. 297-312, 2011.
- [31] M. F. la Cour *et al.*, "Optical imaging for the assessment of hepatocyte metabolic state in ischemia and reperfusion injuries," *Biomedical Optics Express*, vol. 8, no. 10, pp. 4419-4426, 2017.
- [32] M. F. la Cour *et al.*, "Optical metabolic imaging of irradiated rat heart exposed to ischemia–reperfusion injury," *Journal of biomedical optics*, vol. 23, no. 1, p. 016011, 2018.
- [33] M. Aldakkak, D. F. Stowe, J. S. Heisner, M. Spence, and A. K. Camara, "Enhanced Na<sup>+</sup>/H<sup>+</sup> exchange during ischemia and reperfusion impairs mitochondrial bioenergetics and myocardial function," *Journal of cardiovascular pharmacology*, vol. 52, no. 3, p. 236, 2008.
- [34] H.-H. Lu *et al.*, "Molecular imaging of ischemia and reperfusion in vivo with mitochondrial autofluorescence," *Analytical chemistry*, vol. 86, no. 10, pp. 5024-5031, 2014.
- [35] M. Ranji *et al.*, "Optical cryoimaging reveals a heterogeneous distribution of mitochondrial redox state in ex vivo guinea pig hearts and its alteration during ischemia and reperfusion," *IEEE journal of translational engineering in health and medicine*, vol. 4, pp. 1-10, 2016.
- [36] M. Ranji *et al.*, "Quantifying acute myocardial injury using ratiometric fluorometry," *Ieee Transactions on Biomedical Engineering*, vol. 56, no. 5, pp. 1556-1563, 2008.
- [37] R. Sepehr *et al.*, "Optical imaging of lipopolysaccharide-induced oxidative stress in acute lung injury from hyperoxia and sepsis," *Journal of innovative optical health sciences*, vol. 6, no. 03, p. 1350017, 2013.
- [38] S. Maleki, R. Sepehr, K. Staniszewski, N. Sheibani, C. M. Sorenson, and M. Ranji, "Mitochondrial redox studies of oxidative stress in kidneys from diabetic mice," *Biomedical optics express*, vol. 3, no. 2, pp. 273-281, 2012.

- [39] S. A. Lewis *et al.*, "The effect of Tmem135 overexpression on the mouse heart," *PloS one*, vol. 13, no. 8, p. e0201986, 2018.
- [40] S. Maleki *et al.*, "Optical imaging of mitochondrial redox state in rodent model of retinitis pigmentosa," *Journal of biomedical optics*, vol. 18, no. 1, p. 016004, 2013.
- [41] A. W. Cowley Jr *et al.*, "Evidence of the importance of Nox4 in production of hypertension in Dahl salt-sensitive rats," *Hypertension*, vol. 67, no. 2, pp. 440-450, 2016.
- [42] S. Mehrvar *et al.*, "The early effects of uninephrectomy on rat kidney metabolic state using optical imaging," *Journal of Biophotonics*, vol. 13, no. 9, p. e202000089, 2020.
- [43] Z. Zhang *et al.*, "Redox ratio of mitochondria as an indicator for the response of photodynamic therapy," *Journal of biomedical optics*, vol. 9, no. 4, pp. 772-778, 2004.
- [44] S. Mehrvar *et al.*, "670 nm photobiomodulation improves the mitochondrial redox state of diabetic wounds," *Quantitative Imaging in Medicine and Surgery*, vol. 11, no. 1, p. 107, 2021.
- [45] H. Xu *et al.*, "Chop therapy induced mitochondrial redox state alteration in non-hodgkin's lymphoma xenografts," *Journal of innovative optical health sciences*, vol. 6, no. 02, p. 1350011, 2013.
- [46] J. H. Ostrander *et al.*, "Optical redox ratio differentiates breast cancer cell lines based on estrogen receptor status," *Cancer research*, vol. 70, no. 11, pp. 4759-4766, 2010.
- [47] L. Z. Li, H. N. Xu, M. Ranji, S. Nioka, and B. Chance, "Mitochondrial redox imaging for cancer diagnostic and therapeutic studies," *Journal of innovative optical health sciences*, vol. 2, no. 04, pp. 325-341, 2009.
- [48] S. Mehrvar, M. F. la Cour, M. Medhora, A. K. Camara, and M. Ranji, "Optical metabolic imaging for assessment of radiation-induced injury to rat kidney and mitigation by lisinopril," *Annals of biomedical engineering*, vol. 47, no. 7, pp. 1564-1574, 2019.
- [49] A. Iqbal, A. Jan, M. Wajid, and S. Tariq, "Management of chronic non-healing wounds by hirudotherapy," *World journal of plastic surgery*, vol. 6, no. 1, p. 9, 2017.
- [50] C. K. Sen, "Human wounds and its burden: an updated compendium of estimates," ed: Mary Ann Liebert, Inc., publishers 140 Huguenot Street, 3rd Floor New ..., 2019.
- [51] S. a. Guo and L. A. DiPietro, "Factors affecting wound healing," *Journal of dental research*, vol. 89, no. 3, pp. 219-229, 2010.
- [52] T. J. Fahey III, A. Sadaty, W. G. Jones II, A. Barber, B. Smoller, and G. T. Shires, "Diabetes impairs the late inflammatory response to wound healing," *Journal of Surgical Research*, vol. 50, no. 4, pp. 308-313, 1991.
- [53] A. Terranova, "The effects of diabetes mellitus on wound healing," *Plastic surgical nursing: official journal of the American Society of Plastic and Reconstructive Surgical Nurses*, vol. 11, no. 1, pp. 20-25, 1991.
- [54] A. Raghav, Z. A. Khan, R. K. Labala, J. Ahmad, S. Noor, and B. K. Mishra, "Financial burden of diabetic foot ulcers to world: a progressive topic to discuss always," *Therapeutic advances in endocrinology and metabolism*, vol. 9, no. 1, pp. 29-31, 2018.
- [55] S. Enoch and D. J. Leaper, "Basic science of wound healing," *Surgery (Oxford)*, vol. 26, no. 2, pp. 31-37, 2008.
- [56] E. Fernandez and B. Bernhardsen, "Wound Care Management," *Primary Care Reports*, vol. 24, no. 4, 2018.
- [57] M. Löndahl, P. Katzman, A. Nilsson, and C. Hammarlund, "Hyperbaric oxygen therapy facilitates healing of chronic foot ulcers in patients with diabetes," *Diabetes care*, vol. 33, no. 5, pp. 998-1003, 2010.

- [58] A. P. Duzgun, H. Z. Satir, O. Ozozan, B. Saylam, B. Kulah, and F. Coskun, "Effect of hyperbaric oxygen therapy on healing of diabetic foot ulcers," *The Journal of foot and ankle surgery*, vol. 47, no. 6, pp. 515-519, 2008.
- [59] L. Kessler *et al.*, "Hyperbaric oxygenation accelerates the healing rate of nonischemic chronic diabetic foot ulcers: a prospective randomized study," *Diabetes care*, vol. 26, no. 8, pp. 2378-2382, 2003.
- [60] C.-J. Wang, R.-W. Wu, and Y.-J. Yang, "Treatment of diabetic foot ulcers: a comparative study of extracorporeal shockwave therapy and hyperbaric oxygen therapy," *Diabetes research and clinical practice*, vol. 92, no. 2, pp. 187-193, 2011.
- [61] N. Greer *et al.*, "Advanced wound care therapies for nonhealing diabetic, venous, and arterial ulcers: a systematic review," *Annals of internal medicine*, vol. 159, no. 8, pp. 532-542, 2013.
- [62] S. W. Jere, H. Abrahamse, and N. N. Houreld, "The JAK/STAT signaling pathway and photobiomodulation in chronic wound healing," *Cytokine & growth factor reviews*, vol. 38, pp. 73-79, 2017.
- [63] N. N. Houreld, "Shedding light on a new treatment for diabetic wound healing: a review on phototherapy," *The Scientific World Journal*, vol. 2014, 2014.
- [64] M. Cogan and A. Arieff, "Radiation nephritis and intravascular coagulation," *Clinical nephrology*, vol. 10, no. 2, pp. 74-78, 1978.
- [65] J. A. Jurado, R. Bashir, and M. W. Burket, "Radiation-induced peripheral artery disease," *Catheterization and Cardiovascular Interventions*, vol. 72, no. 4, pp. 563-568, 2008.
- [66] J. J. Kruse, J. A. te Poele, N. S. Russell, L. J. Boersma, and F. A. Stewart, "Microarray analysis to identify molecular mechanisms of radiation-induced microvascular damage in normal tissues," *International Journal of Radiation Oncology\* Biology\* Physics*, vol. 58, no. 2, pp. 420-426, 2004.
- [67] H. Izzedine, P. Cluzel, and G. Deray, "Renal radiation-induced arterial stenosis," *Kidney international*, vol. 71, no. 11, p. 1188, 2007.
- [68] L. Bali, F. Silhol, A. Kateb, and B. Vaisse, "Renal artery stenosis after abdominal radiotherapy," in *Annales de Cardiologie et D'angiologie*, 2008, vol. 58, no. 3, pp. 183-186.
- [69] M. Verheij, L. G. Dewit, R. A. V. Olmos, and L. Arisz, "Evidence for a renovascular component in hypertensive patients with late radiation nephropathy," *International Journal of Radiation Oncology\* Biology\* Physics*, vol. 30, no. 3, pp. 677-683, 1994.
- [70] A. Edeani and E. P. Cohen, "Onco-Nephrology: Radiation Nephropathy," American Society of Nephrology, 2012.
- [71] M. Dansinger. "What is nephropathy?" WebMed. <https://www.webmd.com/diabetes/qa/what-is-nephropathy> (accessed).
- [72] M. Baradaran-Ghahfarokhi, "Radiation-induced kidney injury," *Journal of renal injury prevention*, vol. 1, no. 2, p. 49, 2012.
- [73] T. H. Kim, P. J. Somerville, and C. R. Freeman, "Unilateral radiation nephropathy—the long-term significance," *International Journal of Radiation Oncology\* Biology\* Physics*, vol. 10, no. 11, pp. 2053-2059, 1984.
- [74] H. P. Rodemann and M. Bamberg, "Cellular basis of radiation-induced fibrosis," *Radiotherapy and Oncology*, vol. 35, no. 2, pp. 83-90, 1995.
- [75] J. Yarnold and M.-C. V. Brotons, "Pathogenetic mechanisms in radiation fibrosis," *Radiotherapy and oncology*, vol. 97, no. 1, pp. 149-161, 2010.

- [76] T. N. Wight and S. Potter-Perigo, "The extracellular matrix: an active or passive player in fibrosis?," *American Journal of Physiology-Gastrointestinal and Liver Physiology*, vol. 301, no. 6, pp. G950-G955, 2011.
- [77] A. R. Chade, "Renal vascular structure and rarefaction," *Comprehensive Physiology*, vol. 3, no. 2, pp. 817-831, 2013.
- [78] E. P. Cohen, P. Pais, and J. E. Moulder, "Chronic kidney disease after hematopoietic stem cell transplantation," in *Seminars in nephrology*, 2010, vol. 30, no. 6: Elsevier, pp. 627-634.
- [79] D. A. Nordsletten, S. Blackett, M. D. Bentley, E. L. Ritman, and N. P. Smith, "Structural morphology of renal vasculature," *American Journal of Physiology-Heart and Circulatory Physiology*, vol. 291, no. 1, pp. H296-H309, 2006.
- [80] S. Mehrvar *et al.*, "3D-vascular metabolic imaging using inverted autofluorescence," 2021.
- [81] Q. Liu, G. Grant, and T. Vo-Dinh, "Investigation of synchronous fluorescence method in multicomponent analysis in tissue," *IEEE Journal of Selected Topics in Quantum Electronics*, vol. 16, no. 4, pp. 927-940, 2009.
- [82] K. Staniszewski, "OPTICAL INSTRUMENTATION AND IMAGE CYTOMETRY OF LUNG AND EYE INJURIES: STUDIES IN THE RODENT MODEL," Masters, Electrical Engineering, University of Wisconsin Milwaukee.
- [83] R. Sepehr, "Optical studies of oxidative stress in lung tissue: rodent models," 2014.
- [84] J. Li, J. Chen, and R. Kirsner, "Pathophysiology of acute wound healing," *Clinics in dermatology*, vol. 25, no. 1, pp. 9-18, 2007.
- [85] M. Cano Sanchez, S. Lancel, E. Boulanger, and R. Neviere, "Targeting oxidative stress and mitochondrial dysfunction in the treatment of impaired wound healing: a systematic review," *Antioxidants*, vol. 7, no. 8, p. 98, 2018.
- [86] J. Ao, J. P. Wood, G. Chidlow, M. C. Gillies, and R. J. Casson, "Retinal pigment epithelium in the pathogenesis of age-related macular degeneration and photobiomodulation as a potential therapy?," *Clinical & experimental ophthalmology*, vol. 46, no. 6, pp. 670-686, 2018.
- [87] M. R. Hamblin, "Mechanisms and mitochondrial redox signaling in photobiomodulation," *Photochemistry and photobiology*, vol. 94, no. 2, pp. 199-212, 2018.
- [88] S. Passarella *et al.*, "Increase of proton electrochemical potential and ATP synthesis in rat liver mitochondria irradiated in vitro by helium-neon laser," *FEBS letters*, vol. 175, no. 1, pp. 95-99, 1984.
- [89] S. Passarella, A. Ostuni, A. Atlante, and E. Quagliariello, "Increase in the ADP/ATP exchange in rat liver mitochondria irradiated in vitro by helium-neon laser," *Biochemical and biophysical research communications*, vol. 156, no. 2, pp. 978-986, 1988.
- [90] J. T. Eells *et al.*, "Therapeutic photobiomodulation for methanol-induced retinal toxicity," *Proceedings of the National Academy of Sciences*, vol. 100, no. 6, pp. 3439-3444, 2003.
- [91] S. Mehrvar *et al.*, "Fluorescence imaging of mitochondrial redox state to assess diabetic wounds," *IEEE journal of translational engineering in health and medicine*, vol. 7, pp. 1-9, 2019.
- [92] B. Chance, B. Schoener, R. Oshino, F. Itshak, and Y. Nakase, "Oxidation-reduction ratio studies of mitochondria in freeze-trapped samples. NADH and flavoprotein fluorescence signals," *Journal of Biological Chemistry*, vol. 254, no. 11, pp. 4764-4771, 1979.

- [93] P. R. Painter, P. Edén, and H.-U. Bengtsson, "Pulsatile blood flow, shear force, energy dissipation and Murray's Law," *Theoretical Biology and Medical Modelling*, vol. 3, no. 1, pp. 1-10, 2006.
- [94] B. L. Fish, T. J. MacVittie, A. Szabo, J. E. Moulder, and M. Medhora, "WAG/RijCmcr rat models for injuries to multiple organs by single high dose ionizing radiation: similarities to nonhuman primates (NHP)," *International journal of radiation biology*, vol. 96, no. 1, pp. 81-92, 2020.
- [95] M. Medhora *et al.*, "Model development and use of ACE inhibitors for preclinical mitigation of radiation-induced injury to multiple organs," *Radiation research*, vol. 182, no. 5, pp. 545-555, 2014.
- [96] M. Carlström, C. S. Wilcox, and W. J. Arendshorst, "Renal autoregulation in health and disease," *Physiological reviews*, vol. 95, no. 2, pp. 405-511, 2015.
- [97] M. Shu *et al.*, "Porphyrin metabolisms in human skin commensal propionibacterium acnes bacteria: potential application to monitor human radiation risk," *Current medicinal chemistry*, vol. 20, no. 4, pp. 562-568, 2013.
- [98] D. R. Sell *et al.*, "Skin collagen fluorophore LW-1 versus skin fluorescence as markers for the long-term progression of subclinical macrovascular disease in type 1 diabetes," *Cardiovascular diabetology*, vol. 15, no. 1, pp. 1-14, 2016.